AN ELECTRICALLY ACTIVE MICRONEEDLE ELECTROPORATION ARRAY FOR INTRACELLULAR DELIVERY OF BIOMOLECULES

A Dissertation
Presented to
The Academic Faculty

By

Seong-O Choi

In Partial Fulfillment
Of the Requirements for the Degree
Doctor of Philosophy in the
School of Electrical and Computer Engineering

Georgia Institute of Technology

December 2007

AN ELECTRICALLY ACTIVE MICRONEEDLE ELECTROPORATION ARRAY FOR INTRACELLULAR DELIVERY OF BIOMOLECULES

Approved by:

Dr. Mark G. Allen, Advisor
School of Electrical and Computer Engineering
Georgia Institute of Technology

Dr. Pamela T. Bhatti
School of Electrical and Computer Engineering
Georgia Institute of Technology

Dr. Mark R. Prausnitz
School of Chemical and Biomolecular Engineering
Georgia Institute of Technology

Dr. Oliver Brand
School of Electrical and Computer Engineering
Georgia Institute of Technology

Dr. Shyh-Chiang Shen
School of Electrical and Computer Engineering
Georgia Institute of Technology

Date Approved: November 9, 2007

To my family,

For their endless love and support

ACKNOWLEDGEMENTS

First of all, I would like to thank Prof. Allen for his patient guidance throughout the pursuit of my Ph.D. degree. It has been my honor to have him as my advisor. His encouragement and inspiration led me to complete this thesis work. I also would like to thank Prof. Prausnitz for his sincere guidance and support of my research.

In addition, I would like to thank Prof. Brand, Prof. Bhatti, and Prof. Shen for serving on my thesis committee. I appreciate their advice and support, which was invaluable to my degree completion.

I would like to acknowledge the members of the Microsensors and Microactuators (MSMA) group. Special thanks go to Dr. Jung-Hwan Park and Dr. Yong-Kyu Yoon for their valuable advice on the development of fabrication process. I would like to express my gratitude to the Bio-group members, Mr. Swaminathan Rajaraman and Ms. Maxine McClain, for valuable discussions. I also graciously acknowledge Mr. Richard H. Shafer, laboratory manager, and Mrs. Purnima Sharma, laboratory administrator, for their help with the technical and administrative works. I also thank Gary Spinner and the Microelectronics Research Center (MiRC) cleanroom staff for their technical assistant and support with the cleanroom facilities.

My colleagues in the Prausnitz drug delivery group deserve my thanks for many insightful discussions and technical support. I would especially like to thank Dr. Yeuchun Kim, Mr. Jeong Woo Lee, Dr. Harvinder S. Gill, Mr. Joshua Hutcheson, and Dr. Robyn Schlicher. This research could not have been possible without their support. I also want to thank Mrs. Donna Bondy for her generous help with administrative works.

I would like to thank all the people who have helped with my research. In particular, I greatly appreciate the unforgettable support, advice, and friendship of Dr. Yeun-Ho Joung, Dr. Jin-Woo Park, Dr. Seungkeun Choi, and Dr. Jaehyung Seo.

I am deeply grateful to my friends for their encouragement and confidence. I owe Mr. Wonsang Koh special thanks for standing by me with trust. Whenever I had a hard time, he encouraged and supported me. I also want to express my appreciation to Dongjin Yeo, Seungho Lee, Sangjin Kim, Hyungki Park, Jaehyun Shim, Seungyoon Ryu, Soojin Oh, Boram Jung, Kyung Park and Soyoung Bae for their careful consideration and friendship.

Finally, none of this would have been possible without the love and support of my family. I am eternally grateful to my parents and parents-in-law for their endless love and sacrifice, for teaching me right from wrong, for understanding and trusting me, and most importantly, for teaching me how to love people. Lastly, I am forever indebted to my best friend and lovely wife, Mee-Kyung. Her endless love, support, encouragement, patience, sacrifice, and trust over the years made this dissertation possible.

TABLE OF CONTENTS

LIST OF TABLES

LIST OF FIGURES

SUMMARY

The objective of this research is the development of an electrically active microneedle array that can deliver biomolecules such as DNA and drugs to epidermal cells by means of electroporation. Microneedles are currently used for painless transdermal drug delivery, as reported in the literature [1, 2]. Properly metallized microneedles could serve as microelectrodes essential for electroporation. Furthermore, the close needle-to-needle spacing of microneedle electrodes provides the advantage of utilizing reduced voltage, which is essential for safety as well as portable applications, while maintaining the large electric fields required for electroporation. Therefore, microneedle arrays can potentially be used as part of a minimally invasive, highly-localized electroporation system for cells in the epidermis layer of the skin.

This research consists of three parts: development of the 3-D microfabrication technology to create the microneedle array, fabrication and characterization of the microneedle array, and the electroporation studies performed with the microneedle array. A 3-D fabrication process was developed to produce a microneedle array using an inclined UV exposure technique combined with micromolding technology, potentially enabling low cost mass-manufacture. The developed technology is also capable of fabricating 3-D microstructures of various heights using a single mask.

In order to achieve electrical functionality in the fabricated microneedle array, metallization techniques such as laser ablation and metal transfer were exploited. To create electrical interconnects between the device and the outer electronics, holes created by laser drilling were filled with conductive materials to realize the backside contacts essential for microneedle functionality. The fabricated microneedle array was then tested to demonstrate its feasibility for through-skin electrical and mechanical functionality using a skin insertion test. It was found that the microneedles were able to penetrate skin without breakage. To study the electrical properties of the array, a finite element simulation was performed to examine the electric field distribution. From these simulation results, a predictive model was constructed to estimate the effective volume for electroporation. Finally, studies to determine hemoglobin release from bovine red blood cells (RBC) and the delivery of molecules such as calcein and bovine serum albumin (BSA) into human prostate cancer cells were used to verify the electrical functionality of this device.

This work established that this device can be used to lyse RBC and to deliver molecules, e.g. calcein, into cells, thus supporting our contention that this metallized microneedle array can be used to perform electroporation at reduced voltage. Further studies to show efficacy in skin should now be performed.

CHAPTER 1

INTRODUCTION

Recently, microstructures for biological and biomedical applications have become a highly promising research area of microelectromechanical systems (MEMS). Micro-scale devices for biological/biomedical applications are often referred to "BioMEMS" and can be used for a variety of applications such as biosensors [3-8], micro total analysis systems (μTAS) [9-14], neural prostheses [15-18], scaffolds for cell growth [19-21], and drug delivery systems [2, 22-25]. The miniaturization of conventional devices used for clinical or laboratory purposes not only offers a way to reduce manufacturing costs, but also minimizes reagent volumes, increases sensitivity, increases ease of implantation, and provides minimal disturbance and discomfort to patients.

Microsystems are attractive drug delivery devices because many problems of conventional drug delivery techniques, which rely on pills and injections, can be potentially overcome by these means. The limitations of conventional drug delivery techniques, such as loss of drug due to gastrointestinal drug degradation and pain related to intramuscular and intravenous injections, can be potentially overcome by microfabricated drug delivery devices. In drug delivery, it is desired to deliver precise quantities of a particular drug at the proper time and within proximity to the treatment site. For example, timed and pulsatile release of a drug at a specific site can be realized by an implantable drug delivery microsystem, and minimally invasive, painless injection of a drug can be achieved by microneedle arrays.

Using recent developments in biotechnology, new formulations of drugs based on proteins or DNA have been created. The administration of such drugs through conventional approaches such as pills and injection are often not suitable; therefore these therapies require an alternative means for systematic administration. Recently, skin has attracted considerable interest as an alternative pathway for drug delivery. The administration of drugs through the skin can eliminate degradation in the gastrointestinal tract, an occurrence associated with oral delivery; as well as reduce the pain and inconvenience of intravenous injection.

Skin is composed of two main layers, the epidermis and the dermis. The epidermis acts as a physical barrier which is responsible for the prevention of desiccation and mechanical agitation. The outermost layer of the epidermis is called the stratum corneum, which consists mainly of keratin and is the rate-limiting barrier to transdermal delivery. The dermis acts to supply blood to the epidermis, and mediates thermoregulation and immune surveillance. In the stratum granuloma, a deep layer of the epidermis, there is a hydrophobic layer made up of various lipids important for the retention of water. These lipids also have bacterial and fungal static properties and may serve a role in keeping external compounds from entering the deeper layers of the skin [26].

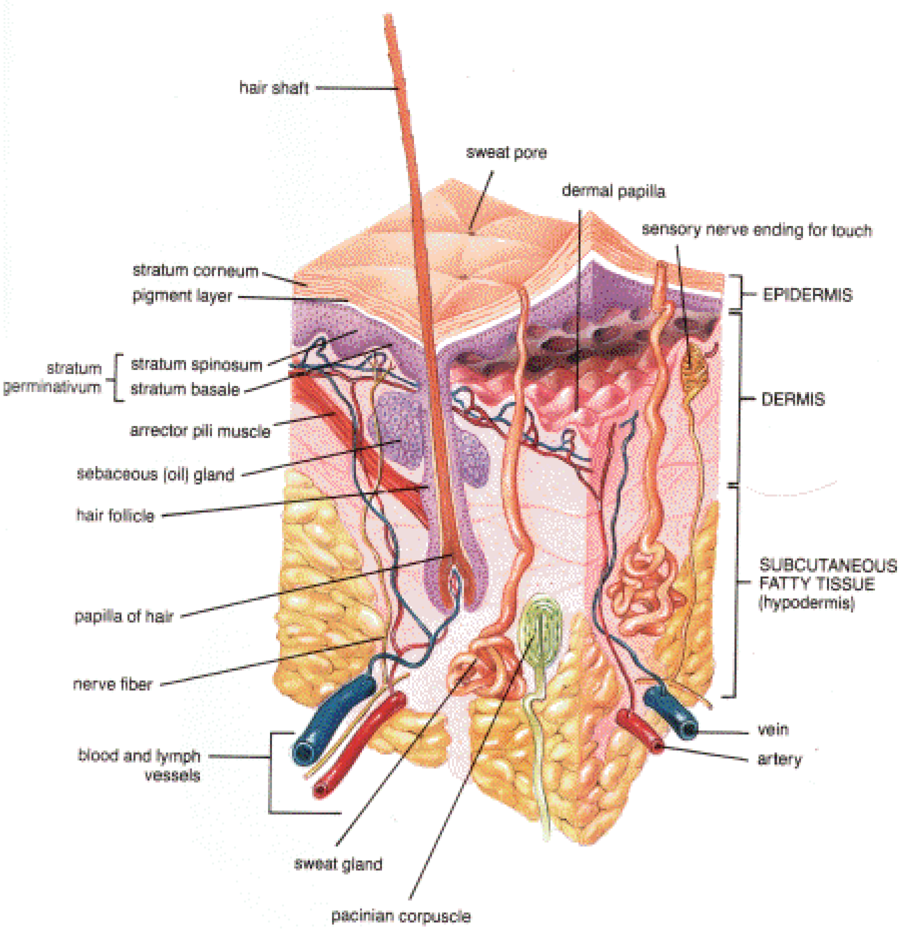

Figure 1.1 Anatomy of human skin, reproduced from [27]

Skin has attractive gene transfer properties because skin is easily accessible, and has a large pool of antigen presenting cells (APCs) that can process and present the antigen to the appropriate lymphocytes efficiently. In addition, epidermal cells slough off after a relatively short life span, thereby eliminating the bulk of the foreign DNA from the patient's body. This may help to lower the risk of negative long-term effects of transfecting cells with foreign DNA. However, skin is a difficult target tissue due to the existence of the stratum corneum, a layer of dead tissue protecting the living cells underneath.

Several methods of transferring genes across the stratum corneum to the epidermis have been proposed. These include intradermal injection of naked DNA [28], ballistic particle bombardment using a gene gun [29], jet injection [30], puncture-mediated transfer [31], tape stripping [32], topical application of viral particles [33], and liposome entrapped DNA [34]. However, these methods are still inefficient. Recently, it has been reported that skin-targeted DNA vaccine delivery using electroporation is quite promising [35, 36], and could provide an alternative means for DNA vaccine delivery to a variety of cell types. Target cells of interest include keratinocytes, Langerhans cells (LHC), and dendritic cells (DC), which are located in the two main areas of the skin, the epidermis and the dermis. After maturation, the LHC, found mainly in the epidermis, and the dermal DC, found mainly in the dermis, can migrate to local lymph nodes where presentation of antigens to T cells can occur and initiate a variety of immunological responses [37].

The objective of this research is to develop a microdevice for delivering biomolecules such as DNA into the skin by means of electroporation. The basic requirements of the device include: 1) penetrating the stratum corneum layer, and 2) providing an electrical pathway to generate an electric field. In addition, the device should provide a means for reducing pain during injection and alleviating tissue burning during applying an electric field, two issues that plague traditional therapies. One promising approach for satisfying these requirements is to implement electrical functionality on a microneedle array. A properly metallized microneedle array can provide minimally invasive, painless insertion into skin and can act as an electrode. Due to the shallow insertion depth of the microneedles, pain caused during application of an electric field due to disturbance of the nerves can also be minimized. In addition, the voltage required for electroporation can be reduced due to the small size scale of the device, avoiding the need for a high voltage source, which is not suitable for portable applications, as well as potentially enhancing overall safety.

In Chapter 2, an overview of electroporation and the fabrication technologies of microneedles are presented. Fabrication technologies for 3-D metal-patterned microstructures have been developed to achieve the goal of this research, and the details are discussed in Chapter 3. By using the technologies presented in Chapter 3, two types of microneedle arrays were fabricated and characterized by insertion tests and electric field simulations. These results are presented in Chapter 4. To verify electrical functionality of the fabricated devices, electroporation experiments were performed with red blood cells and human prostate cancer cells *in vitro*, and the experimental results are presented in Chapter 5. The conclusion of this research and suggestions for future directions are given in Chapter 6.

CHAPTER 2

BACKGROUND

2.1 Electroporation Overview

2.1.1 Background

Electroporation (also called electropermeabilization) refers to the phenomenon of increasing the permeability of cell membranes by exposing cells to a short and strong electric field. This phenomena was first reported by Stampfli [38] in 1958, but received little attention for over a decade. In 1967, Sale and Hamilton [39] showed that strong electric fields could cause cell death, and Neumann and Rosenheck [40] demonstrated a change in cell membrane permeability by electrical pulses in 1972. Since their report, many researchers have investigated the effect of electric fields on cells to understand the fundamental mechanism of the permeability phenomena. The exact mechanism is still not fully understood. The most popular theory is that the electric field causes the formation of aqueous pores in the plasma membrane [41-43]. According to this theory, the electric field causes hydrophilic pores to be formed by reorientation of the plasma membrane lipid bilayer in such a manner that the hydrophilic head groups face the pore, while the hydrophobic tails are hidden inside the membrane. Calculations based on this theory predict that the size of an electroporation-created pore would be on the order of nanometers. However, experiments have shown that molecules bigger than the predicted size of the pore can cross the cell membrane during electroporation. This indicates that another mechanism may be involved in this phenomenon.

Although theoretical models of electroporation cannot explain the exact mechanism, there is a general agreement between researchers that the exposure of cells to an intense electric field for brief periods of time causes a “dielectric breakdown” of biological membranes, allowing molecules to be transferred into the cells. Researchers have taken advantage of this unique property of electroporation to introduce many different molecules such as dyes [44-46], radiotracers [47, 48], drugs [49-51], oligonucleotides [52], RNA [53, 54], and DNA [55-58] into cells. Electroporation is currently used for medical applications such as electrochemotherapy (ECT), transdermal drug delivery, and gene therapy [59-62].

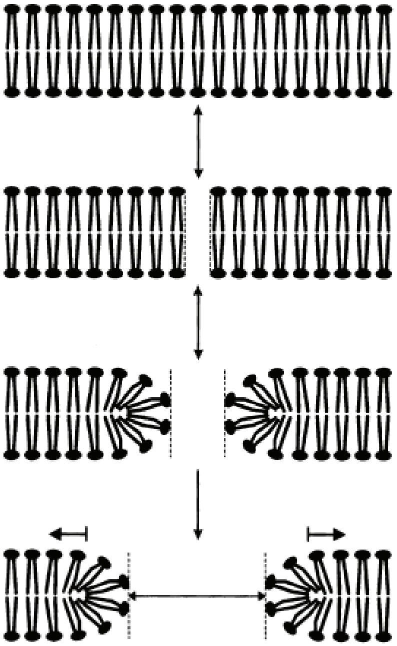

Figure 2.1 Illustration of the formation of an aqueous pore by an external electric field; adopted from ref. [43]

2.1.2 Estimation of Transmembrane Potential

Electroporation is a threshold phenomenon, and can only occur when a transmembrane potential reaches a certain value, typically 0.2-1V [63, 64]. When a cell is exposed to an electric field, a transmembrane voltage is induced on the cell membrane. If the induced voltage exceeds a threshold value, which is dependent mainly on the size of cell, aqueous pores are formed. As the electric field strength increases, the size and the number of pores also increase. The aqueous pores are resealed over minutes after a short and moderately strong application of the electric field (reversible electroporation). However, if exposure to the electric field occurs for too long, or if the magnitude of the electric field is too high, the cell membrane cannot return to its normal state, leading to cell death (irreversible electroporation). For the purposes of intracellular delivery, it is desirable to optimize experimental parameters such that both high intracellular transfer rate and high cell viability can be achieved. For electrochemotherapy, both reversible and irreversible electroporation could be acceptable, but parameters should be optimized to reduce side effects such as pain, muscle contraction, and necrosis of healthy tissue near the treated area.

Many factors must be considered when designing an effective electroporation system. These include electric field strength, pulse length, pulse shape, number of pulses, interval between pulses, size of target cells, and thermal conditions during and after the pulse. The most important parameters in determining the transmembrane voltage are the field strength and the pulse length [65]. To estimate the transmembrane voltage induced on the cell membrane by an external electric field, a simple analytical model was proposed by Schwan [66]. This model assumed that the cell is spherical, and the membrane is nonconductive. The relationship between an external electric field and the induced transmembrane voltage is given as:

$$\Delta\Phi = \frac{3}{2} ER\cos\varphi \tag{2.1}$$

where $\Delta\Phi$ is the induced transmembrane voltage, E is the external electric field, R is the cell radius, and φ is the polar angle measured from the center of the cell with respect to the direction of the field. This is often referred to as Schwan's equation.

From the equation given above, it is possible to roughly estimate the minimum electric field strength required to achieve electroporation of the cell. However, the electric conductivity of cell membrane is not zero. In order to account for this conductivity, the above equation can be modified as follows [67]:

$$\Delta\Phi = \frac{3}{2}\frac{\sigma_e\left[3dR^2\sigma_i + (3d^2R - d^3)(\sigma_m - \sigma_i)\right]}{\left[R^3(\sigma_m + 2\sigma_e)(\sigma_m + \frac{1}{2}\sigma_i) - (R-d)^3(\sigma_e - \sigma_m)(\sigma_i - \sigma_m)\right]} ER\cos\varphi \tag{2.2}$$

where σ_i, σ_m , and σ_e are electric conductivities of the cytoplasm, cell membrane, and external medium, respectively, and d is the membrane thickness. The above model assumes constant thickness and conductivity of the cell membrane. When the conductivity of cell membrane, σ_m is set to zero, then Equation 2.2 simplifies to Schwan's equation.

Equations 2.1 and 2.2 assume that a cell is spherical. However, some types of cells such as erythrocytes are not spherical, but are oblate spheroid. So it is desirable to derive a generalized form of Schwan's equation to expand its application to spheroidal cells. In 2000, Kotnic and Miklavčič [68] derived the equation for transmembrane voltage induced by electric fields on spheroidal cells, and the final result reads as follows:

$$\Delta\Phi = E\frac{R_2^2 - R_1^2}{\frac{R_2^2}{\sqrt{R_2^2 - R_1^2}}\, arc\cot\frac{R_1}{\sqrt{R_2^2 - R_1^2}} - R_1} \times \frac{R_2\cos\varphi}{\sqrt{R_1^2\sin^2\varphi + R_2^2\cos^2\varphi}} \quad \text{for } R_1 < R_2 \qquad (2.3)$$

$$\Delta\Phi = \frac{3}{2}ER_1\cos\varphi = \frac{3}{2}ER_2\cos\varphi \quad \text{for } R_1 = R_2 \qquad (2.4)$$

$$\Delta\Phi = E\frac{R_1^2 - R_2^2}{R_1 - \frac{R_2^2}{\sqrt{R_1^2 - R_2^2}}\log\frac{R_1 + \sqrt{R_1^2 - R_2^2}}{R_2}} \times \frac{R_2\cos\varphi}{\sqrt{R_1^2\sin^2\varphi + R_2^2\cos^2\varphi}} \quad \text{for } R_1 > R_2 \qquad (2.5)$$

where E is the external electric field, R_1 is the radius along the axis of rotational symmetry, R_2 is the radius perpendicular to the axis of rotational symmetry, and φ is the polar angle measured from the center of the cell with respect to the direction of the field. All equations described thus far are based on single cell models and cannot be applied to cell suspensions due to the fact that the electric field outside a cell is not homogeneous. However, these models are useful for determining the range of electric field strength required for electroporation.

2.1.3 Electrodes for Electroporation

The requirements for successful delivery of molecules through skin via electroporation are: 1) administration of molecules to the appropriate sites; and 2) application of an appropriate electric field to the sites within a time window. Typically the molecule to be delivered is injected with a needle and syringe, followed by the application of an electric field with electrodes.

There are three electrode types, which are shown in Figure 2.2. The most widely used electrodes are plate electrodes, separated by either a fixed or a variable distance. In the latter case, the electrode plates are typically mounted on a caliper. These types of electrodes can generate a uniform electric field required for efficacious electroporation. However, the skin must be folded and held between the electrode calipers during electroporation. This results in pain during electroporation that is caused by excitation of nerves by the external electric field. Also, superficial skin burning has been observed as a consequence of the breakdown of the stratum corneum.

Needle electrodes can exist as a needle pair or a needle array. Needle electrodes are useful for the treatment of deep-seated tumors, and can also be used for skin immunization. Typically, the needle lengths are on the order of a millimeter, causing the patient to feel some pain during insertion. Also, the conical geometry results in an inhomogeneous electric field; recently, however, it has been reported that this limitation can be overcome by a proper arrangement of needles coupled with an appropriate voltage application strategy [69].

Surface electrodes are useful for skin electroporation. Due to the noninvasive nature of this method, it offers patient-friendly treatment. Also, the potential drop between the electrodes is mainly confined to the stratum corneum. Underlying nerves and muscles are not subjected to a strong electrical stimulus. However, the initial administration of molecules into the skin requires a hypodermic needle, resulting in pain.

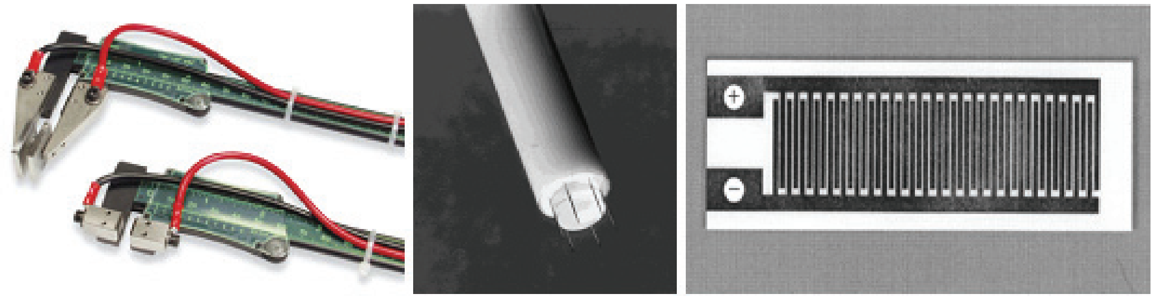

(a) (b) (c)

Figure 2.2 Different types of electrode for electroporation: (a) plate, (b) needle, and (c) surface

Two main problems associated with electroporation using conventional electrodes are occurrence of pain and the high voltage requirement. These problems can potentially be overcome by adopting microneedles as electrodes. Due to their shallow penetration depth, microneedles can minimize pain during injection. Also, the high electric field required for traditional electroporation can be reduced because of the small gap between microneedles. To illustrate how electroporation can be incorporated into microneedle structures, microneedle fabrication techniques will be discussed in the following section.

2.2 Microneedle Overview

2.2.1 Background

The idea to use micron-sized needles for transdermal drug delivery was proposed in 1976 [70], and the first micro-piercing structure for delivering molecules across the skin was reported in 1995 [71]. The microstructure of these needles was a pyramidal shape formed using well-established silicon wet etching technology. It was shown that the tip of the microprobe penetrated through a nematode cuticle without causing injury to the nematode, and resulting in a foreign gene being successfully delivered into the nematode. MEMS technology was developed in the interim, and enabled both new shapes and sizes to be fabricated with much greater manufacturability. In 1998, the use of solid microneedles for transdermal drug delivery was first demonstrated (Figure 2.3) [72]. To create a microneedle structure, Cr was deposited on a silicon wafer, and then patterned. Next, the silicon wafer was etched by a deep reactive ion etching process based on fluorine/oxygen chemistry. Tests showed that the microneedles were able to penetrate skin without breaking and increased the permeability of human epidermis to calcein *in vitro* by 3 to 4 orders of magnitude depending on insertion time.

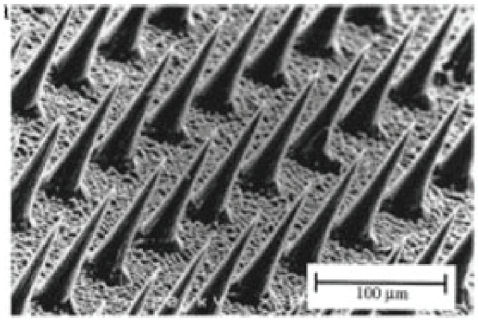

Figure 2.3 SEM pictures of microneedles fabricated by Henry et al. [72]

From a structural point of view, microneedle structure can be categorized into two groups, solid or hollow microneedles. Both types will be discussed in the following sections.

2.2.2 Solid Microneedles

Solid microneedles have been used to pierce skin prior to the application of topical drugs so that the permeability of the drugs into the skin is dramatically increased. To effectively pierce the skin, the microneedle structure should be strong. Typically silicon and metal have been used as structure materials. As discussed before, the first two microneedle structures were fabricated from silicon utilizing either wet or dry etching technologies. These technologies are common in the microelectronics industry.

Another example of silicon-based microneedles are the microenhancer arrays (MEAs) fabricated by Mikaszta et al.[73], as shown in Figure 2.4. These microenhancer arrays were fabricated using a KOH etch technique, providing mesa-point geometry. The needle heights ranged from 50 to 200 µm, with spacing between microenhancers of twice the height. It was demonstrated that these structures were capable of breaching the outermost skin layer, the stratum corneum, and enhancing reporter gene activity up to 2800 fold *in vivo.*

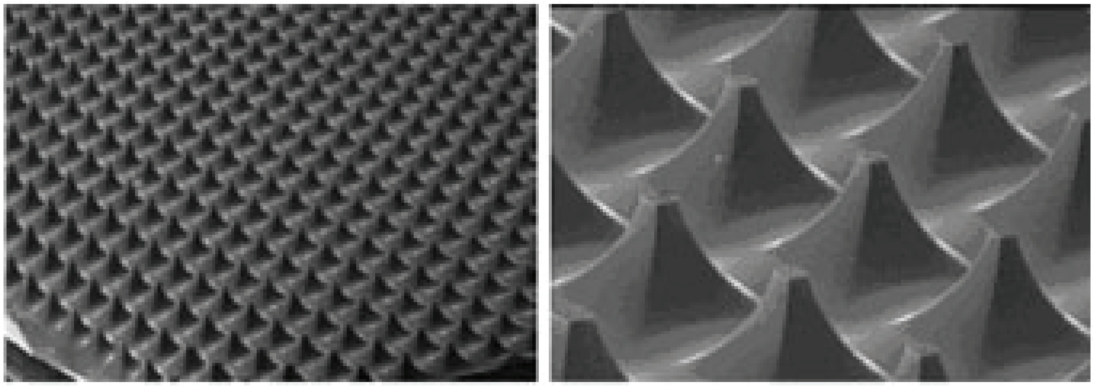

Figure 2.4 SEM pictures of microenhancer arrays, Mikszta et al. [73]

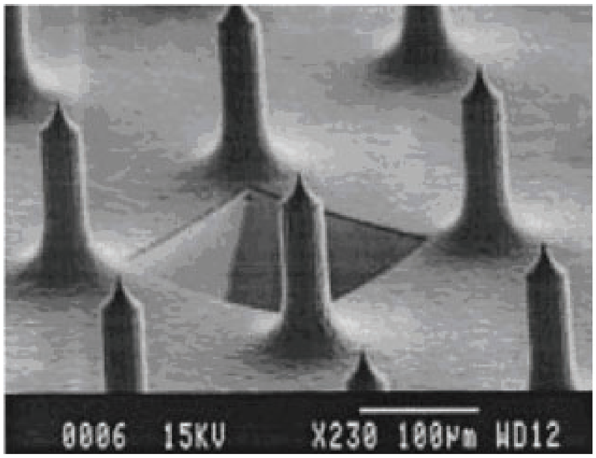

Figure 2.5 SEM picture of microneedle array for biopotential measurement, Griss et al. [74]

In addition to the application of the microneedle structure for transdermal drug delivery, microneedles have also been used for biopotential measurement [74] as shown in Figure 2.5. These needles were also fabricated by utilizing silicon etching technology (dry and wet). It was demonstrated that this microneedle structure could pierce human skin and record low amplitude biopotentials resulting from brain activity.

Previous silicon microneedle structures were based on conventional photolithography followed by silicon etching. Recently, Shikida et al. reported pen-shaped microneedle structures fabricated by a combination of anisotropic wet etching and a dicing technology [75]. The fabrication shaped post structure using a dicing saw, and then etched the structure anisotropically. The fabrication process and fabricated structures are shown in Figure 2.6.

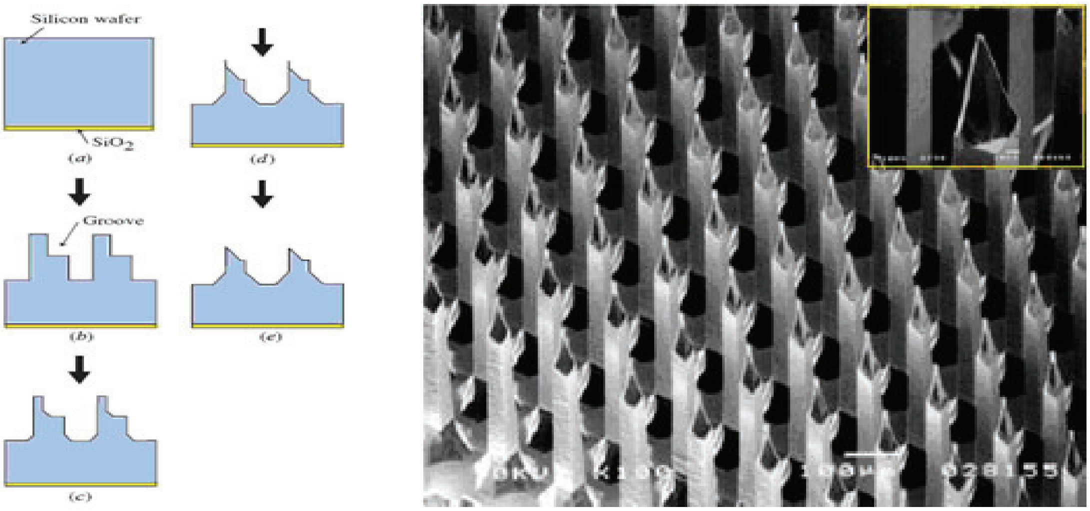

(a) (b)

Figure 2.6 Pen-shaped microneedle structures reported by Shikida et al. [75]; (a) Fabrication process, and (b) fabricated structures

Due to its mechanical strength, ease of fabrication, and relatively inexpensive cost, metal is an attractive candidate for microneedle fabrication. The Macroflux® microprojection array is a metal array currently used in medical applications, and is fabricated by etching a titanium or stainless steel sheet with the desired pattern, then bending the arrays perpendicular to the horizontal plane [76, 77], as shown in Figure 2.7. These microprojection arrays have been used to deliver desmopressin, a synthetic peptide hormone for treatment of enuresis in young children, and ovalbumin, an albumin obtained from the white of eggs, through the skin of hairless guinea pigs.

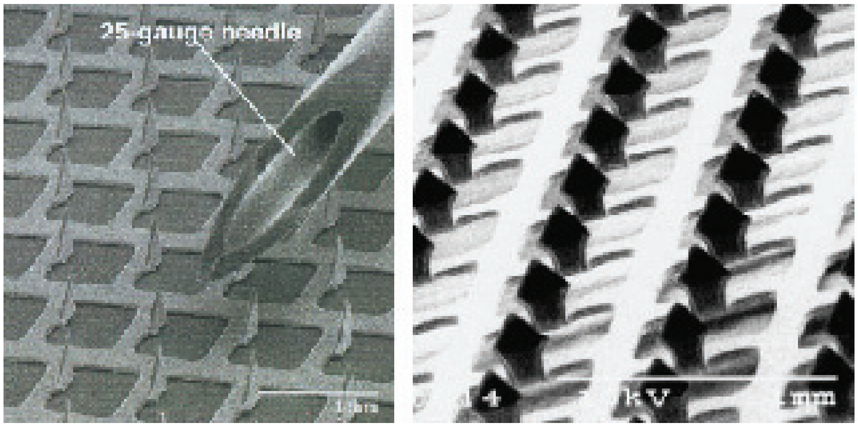

(a) (b)

Figure 2.7 SEM picture of microprojection arrays; (a) Matriano et al. [76], and (b) Cormier et al. [77]

Instead of etching metal sheets to fabricate metal microneedles, Martanto et al. [78] utilized a laser ablation technique to form metallic microneedles such as those shown in Figure 2.8. After cutting the microneedles from a 75 µm stainless steel sheet using an infrared laser, each microneedle was manually bent vertically. Electropolishing was used to sharpen the microneedle tips. This microneedle array was used to increase transdermal delivery of insulin to diabetic hairless rats.

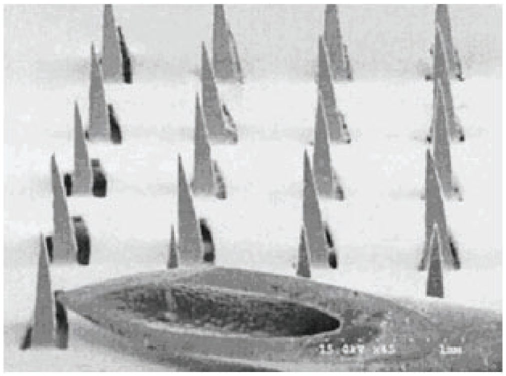

Figure 2.8 SEM picture of solid metal microneedles, Martanto et al. [78]

Most microneedles have been fabricated from silicon or metal, but recently, polymer microneedles have received considerable attention. Compared to both silicon and metal microneedles, polymer microneedles offer several advantages including ease of manufacture using micromolding technology, fewer safety concerns and the capability of using biodegradable polymers to encapsulate molecules that will be delivered into the skin. Various polymers and microneedle geometries have been studied by Park et al. [79]. The microneedle structures were made of polylactic acid (PLA), polyglycolic acid (PGA), and their co-polymer, PLGA. Several different microneedle geometries such as beveled-tip, chisel-tip, and tapered-cone structures were demonstrated.

For fabricating a beveled-tip microstructure (Figure 2.9), SU-8 epoxy photoresist was patterned in a cylindrical shape followed by the application of a sacrificial polymer layer between SU-8 cylinders. Then, a metal layer was deposited to form a mask. The sample was etched using reactive ion etching to form a beveled-tip. After forming the tip, the sacrificial layer was removed. Once the SU-8 master structure was formed, polydimethylsiloxane (PDMS) was applied to form a mold. A polymer microneedle structure was formed by melting a polymer in the PDMS mold.

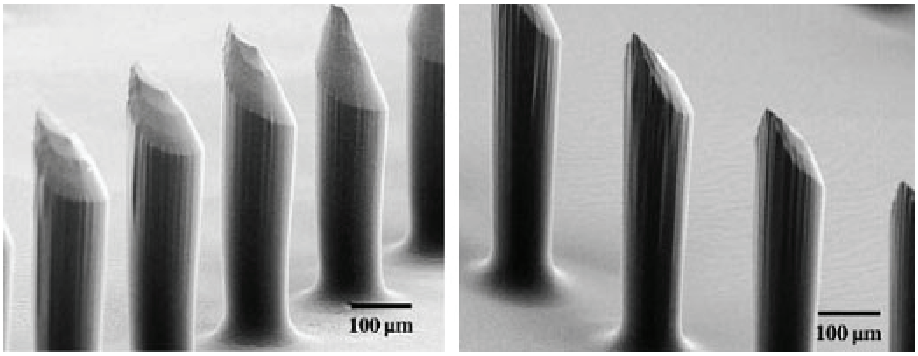

Figure 2.9 SEM pictures of beveled-tip microneedles, Park et al. [79]

Chisel-tip microneedles (Figure 2.10a) were fabricated by using both silicon wet etching and high-aspect-ratio SU-8. The mold for a chisel-tip shape was formed by etching a silicon wafer, and then applying SU-8 on top of the pre-etched silicon wafer. PDMS was used to cover the structure, and then SU-8 was removed by reactive ion etching to form the final mold.

To fabricate tapered-cone microneedles (Figure 2.10b), SU-8 was coated on a glass substrate bearing microlenses that were formed by glass wet etching. UV light was then exposed from the back side, forming tapered-cone microneedle structures.

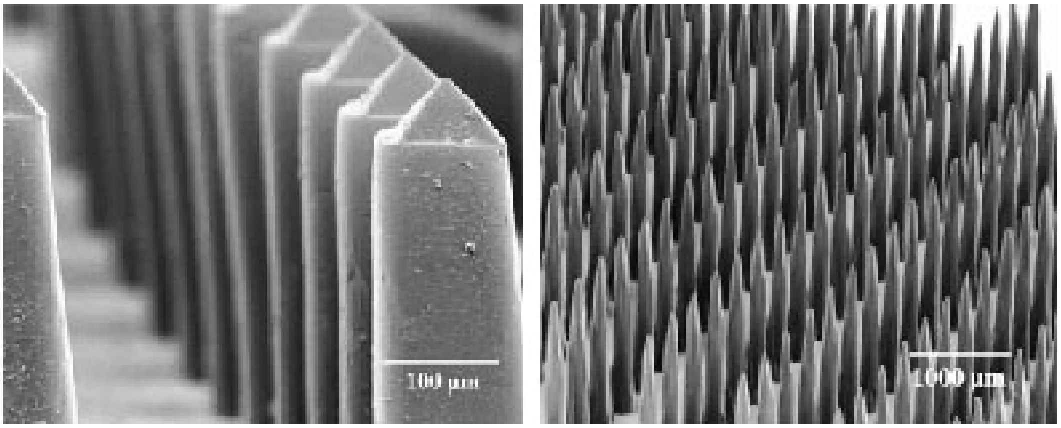

(a) (b)

Figure 2.10 SEM pictures of polymeric microneedles reported by Park et al. [79]; (a) chisel-tip, and (b) tapered-cone microneedles

2.2.3 Hollow Microneedles

Solid microneedles can penetrate the skin, resulting in dramatically increased skin permeability. However, the transport mechanism of molecules is then limited to diffusion across the breaks in the stratum corneum. To deliver molecules at a faster rate, hollow microneedles that enable convective transfer have been fabricated.

Previously, hollow microneedles were fabricated as in-plane structures by both surface and bulk micromachining techniques [80, 81] (Figure 2.11).

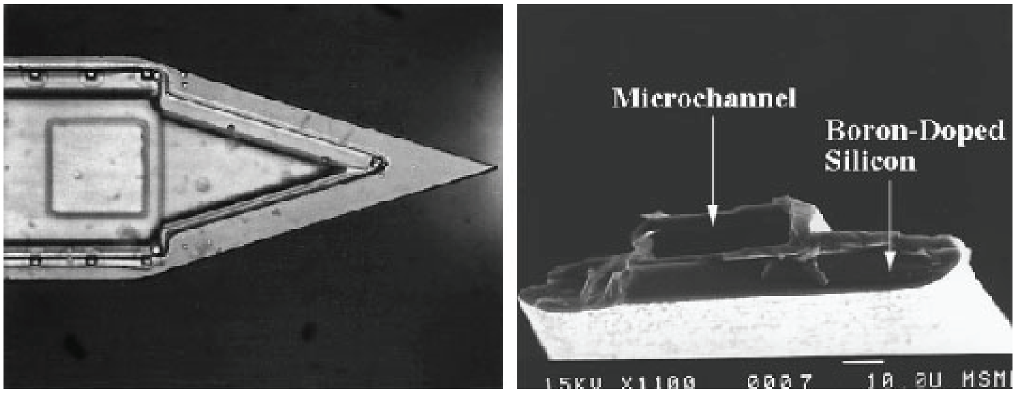

(a) (b)

Figure 2.11 Silicon hollow microneedle fabricated by Lin and Pisano [81]; (a) Top view, and (b) cross section

In-plane hollow metal microneedles have also been fabricated by Chandrasekaran et al. [82] (Figure 2.12). This metallic hollow microneedle was formed by photolithography of thick photoresist followed by electroplating palladium or nickel and platinum. It was demonstrated that this type of microneedle could withstand an applied pressure up to 700 kPa, and achieve a flow rate of 4000μL/h at 106 kPa using water.

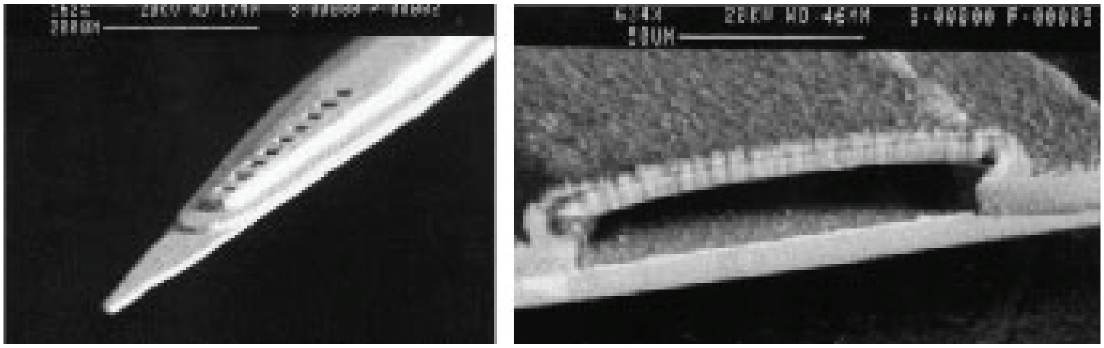

(a) (b)

Figure 2.12 SEM pictures of fabricated metallic hollow microneedle; (a) Top view, and (b) cross section

The main advantage of in-plane hollow microneedle structures have over out-of-plane hollow microneedle structures is that they utilize well-established technologies in microelectronics, allowing complex designs of the microneedle arrays. However, it is not easy to fabricate an array with high microneedle density due to inherent limitations of 2-D fabrication. It is possible to increase the density of microneedles by assembling and combining multiple microneedle arrays, but this method is inefficient and impractical. By virtue of the effort of many researchers, novel technologies for fabricating 3-D microstructures have been developed. These technologies have made it possible to create complex, high-density out-of-plane microneedle structures. Gardeniers et al. [83] fabricated out-of-plane silicon hollow microneedles for transdermal liquid transport by a sequence of deep-reactive ion etching, anisotropic wet etching and conformal thin film deposition. The length of the microneedle varied between 150 and 350 μm, and the widest needle base was 250 μm. The detailed fabrication process and the resulting fabricated structures are shown in Figure 2.13.

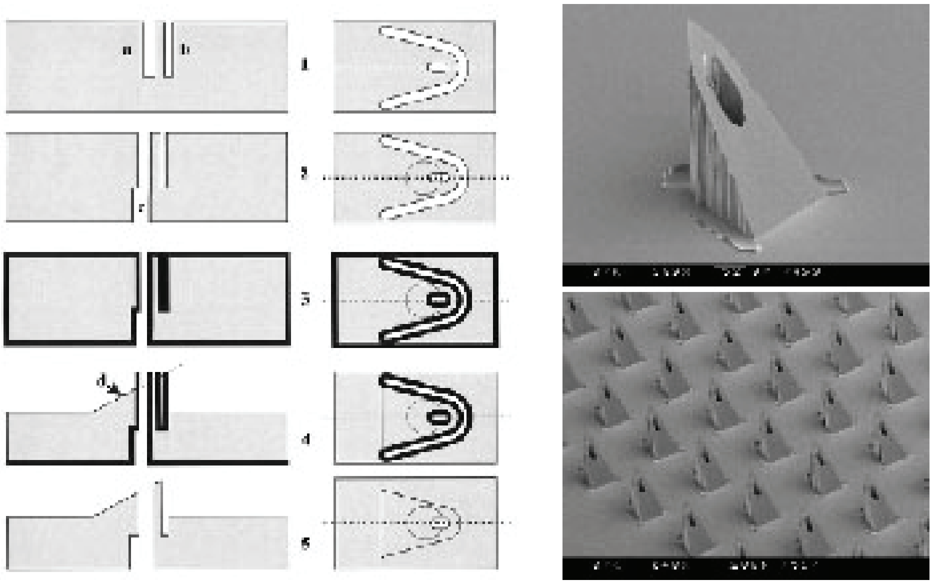

(a) (b)

Figure 2.13 Out-of-plane microneedles; (a) fabrication process, and (b) fabricated structure

The fabrication of side-opened, out-of-plane microneedle structures was demonstrated by Griss and Stemme [84] (Figure 2.14a and b). Side-opened structures were fabricated to minimize clogging by tissue during microneedle insertion. Therefore, this geometry gives low resistance to liquid flows and a large exposure area between the fluid and the tissue. Even though the structure looks complex, it requires only 2 masks. Recently, the same group reported another type of hollow, side-opened, out-of-plane microneedle array fabricated by tapered deep reactive ion etching [85], shown in Figure 2.14c.

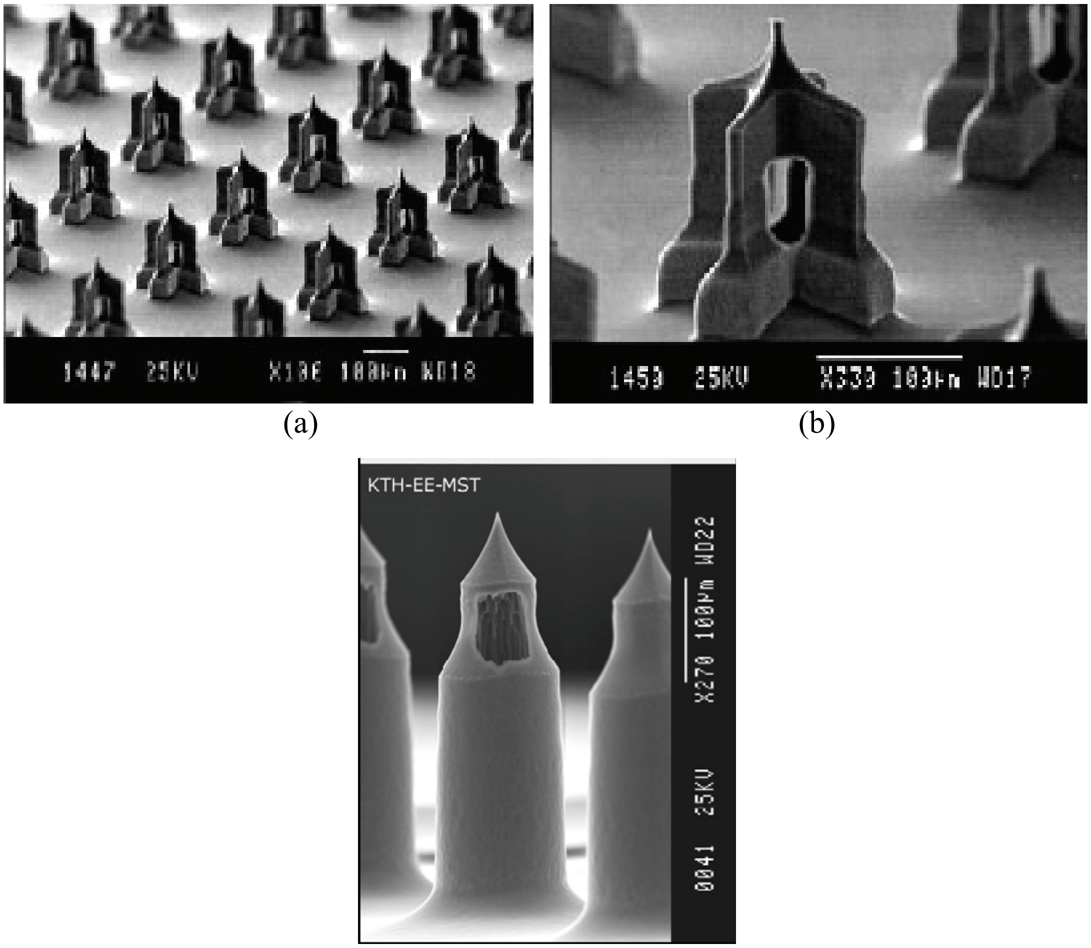

(a) (b)

(c)

Figure 2.14 SEM pictures of side-opened microneedles

Mukerjee et al. [86] developed a hollow microneedle array for biological fluid extraction. The system contains microfluidic channels, which are used for analyzing biological fluid in situ. These arrays were fabricated using deep reactive ion etching, diamond blade circular sawing, and isotropic etching. The fabricated device is shown in Figure 2.15a. A similar microneedle structure, which is shown in Figure 2.15b, was reported by Stoeber and Liepmann [87] using similar fabrication steps. The only difference between the fabrication processes of the two microneedle arrays was the method used to define the microneedle. The first group used a diamond saw to define the column structure, followed by isotropic etching of the column to form the microneedle structure. In contrast, the second group etched silicon isotropically with a mask to define the needle structure.

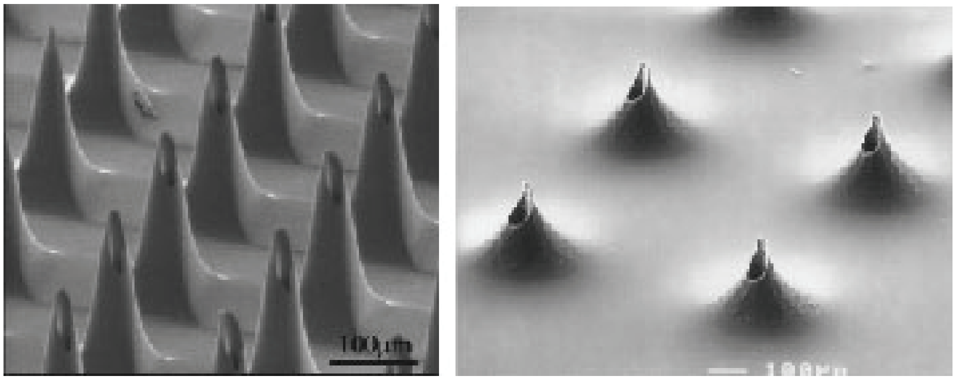

(a) (b)

Figure 2.15 SEM picture of hollow microneedle array fabricated by silicon etching,; (a) Mukerjee et al. [86], and (b) Stoeber et al. [87]

Most hollow microneedle arrays have been fabricated from silicon using well-established dry and wet etching techniques. However, other materials, such as metals and polymers, are also attractive candidate materials for microneedles. Compared to the silicon micromachining process, metals and polymers can be processed at a lower cost with higher fidelity. Davis et al [88] used hollow metal microneedles, which were fabricated by electrodeposition of Ni in polyethylene terephthalate, for insulin delivery to diabetic rats. To prepare a micromold for electrodeposition of Ni, a polymer sheet was ablated by an excimer laser. After electrodeposition, the polymer sheet was selectively etched, forming hollow metal microneedles, which are shown in Figure 2.16.

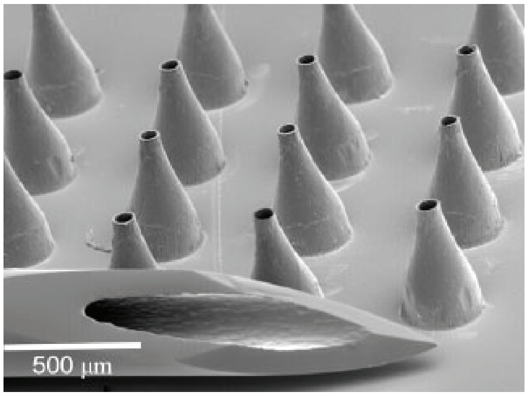

Figure 2.16 SEM picture of hollow metal microneedle array

Another technology for the fabrication of hollow metal microneedles was proposed by Kim et al.[89]. They utilized a backside exposure technique to form tapered structure out of thick photoresist, SU-8. Once the tapered SU-8 structure was fabricated, a seed layer was deposited on the structure, and then electroplating was performed. The top opening was formed by a polishing process, and then the metallic structure was separated from the SU-8 structure, giving the tapered hollow metal microneedles shown in Figure 2.17.

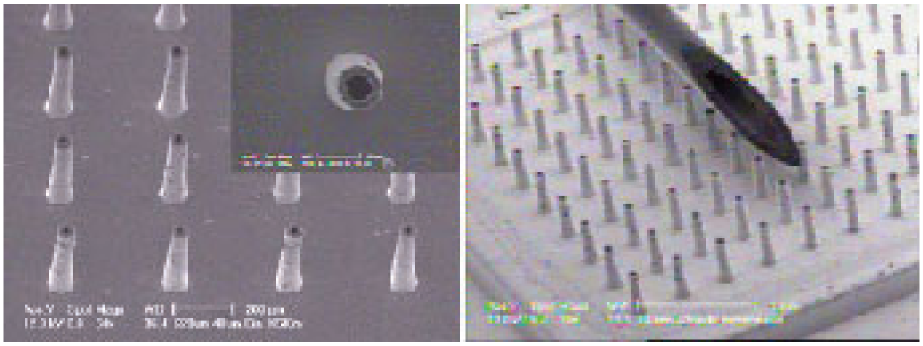

Figure 2.17 SEM picture of tapered hollow metal microneedle array

Compared to both silicon and metal, polymers have a relatively low mechanical stiffness. Therefore, polymer microneedle fabrication has received considerably less attention than the previously discussed materials. Recently, however, it was demonstrated that hollow microneedles made of polymethylmethacrylate (PMMA) could penetrate skin without breaking [90]. The microneedle structure was fabricated by exposing deep x-ray in an inclined fashion similar to the inclined UV exposure technique that has been demonstrated by many authors [91-94]. The longest microneedle fabricated was 1000µm, with a needle base of 400µm, and a hole diameter of 100µm. A fabricated polymer hollow microneedle is shown in Figure 2.18.

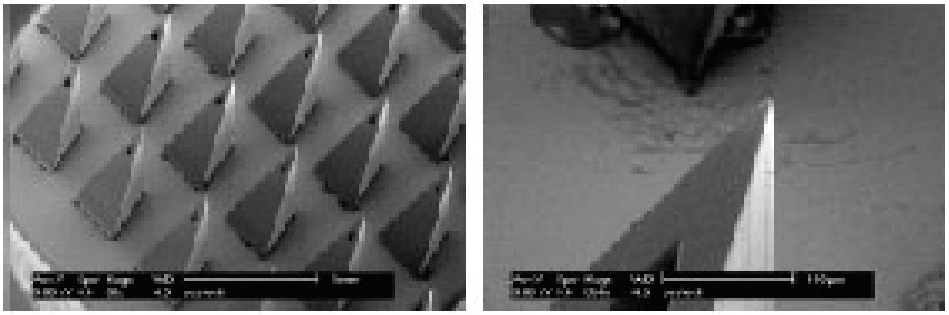

Figure 2.18 SEM pictures of PMMA microneedle, Moon et al. [90]

Many fabrication technologies developed for fabricating microneedle structures with different materials have been reviewed. Some representative studies are summarized in Table 2.1.

Table 2.1 Summary of microneedle fabrication technologies

	Material	Technology		
		Dry etching	Wet etching	Others
Henry et al. [72]	Silicon	RIE	–	–
Mikszta et al. [73]	Silicon	–	KOH	–
Griss et al. [74]	Silicon	DRIE	KOH	–
Shikida et al. [75]	Silicon	–	KOH	Dicing
Mukerjee et al. [86]	Silicon	DRIE	KOH	Dicing
Martanto et al. [78]	Metal	–	–	Laser ablation
Davis et al. [88]	Metal	–	–	Laser ablation / Electroplating
Park et al. [79]	Polymer (PLA, PGA, PLGA)	RIE	–	Micromolding
Moon et al. [90]	Polymer (PMMA)	–	–	Deep X-ray

Most current microneedle fabrication technologies require etching steps to sharpen the tip of the microneedles. These etching steps are not suitable for low-cost mass manufacturing, since dry etching techniques demand high-cost equipment and long processing time due to the low etch rate. Wet etching techniques have difficulty controlling the etch rate over a large area. Moon et al. [90] demonstrated the fabrication of a PMMA microneedle array without any etching steps. However, this requires a high-cost process. Other techniques such as laser machining are serial processes, which may not be time-efficient. Therefore, it is desirable to develop a microneedle fabrication technology which enables mass production at low cost. To achieve this goal, several fabrication technologies have been developed, and will be discussed in the following chapter.

2.3 Electroporation with Microneedles

Microneedles have been used for transdermal drug delivery, and reports indicate that they could be inserted into skin without pain [72]. With proper metallization, microneedles could serve as microelectrodes to be used for electroporation. In addition, the close spacing of the microneedle electrodes provides an advantage of reduced voltage while simultaneously maintaining the large electric fields required for electroporation. With these advantages, microneedles can potentially be utilized as a minimally invasive, highly-localized electroporation system for cells in the epidermis of the skin. The concept of an electroporation microneedle array was proposed by Cyto Pulse Sciences, Inc. [95] in 2003, and Figure 2.19 illustrates the concept of delivery of biomolecules into cells with an electroporation microneedle array.

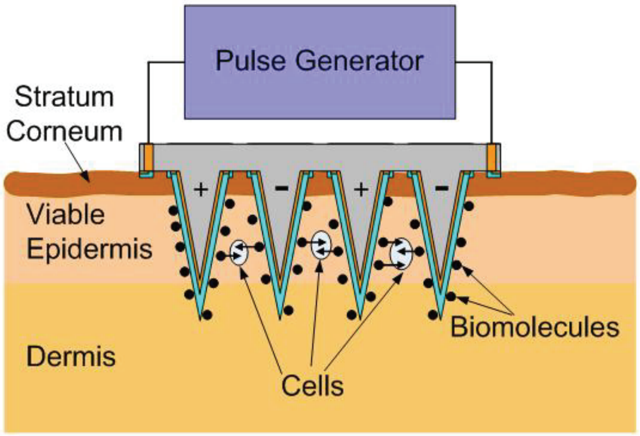

Figure 2.19 Conceptual use of a microneedle electrode array to electroporate cells in epidermis

Microneedles could serve two functions for delivering molecules into skin. By coating microneedle structures with molecules, microneedles could first serve as a vehicle to deliver molecules to the epidermis. While microneedles remain inserted in skin, they could subsequently serve as microelectrodes to locally electroporate epidermal cells and thereby transport the molecules into cells. Recently, several research groups have demonstrated the potentiality of this approach [96-98]. Building on previous studies, we have developed novel fabrication technologies to overcome some of the problems that have limited the application of electroporation by microneedles.

CHAPTER 3

DEVELOPMENT OF 3-D MICROFABRICATION TECHNOLOGY

3.1 Inclined/Rotational Photolithography for 3-D Fabrication

3.1.1 Introduction

Photolithography based on ultraviolet (UV) exposure has been used in both the semiconductor industry as well as research to transfer patterns from a mask to a wafer. Recently, more exotic lithographic methods such as electron beam lithography, extreme ultraviolet lithography, x-ray lithography, and ion beam lithography have been investigated to overcome the limitation of conventional UV lithography. These methods target the generation of fine features in two dimensions, sufficient for fabrication of semiconductors. In the MEMS world, however, it becomes important to fabricate 3-D structures for a variety of applications including but not limited to microneedles; thus, researchers have devoted much time to the development of 3-D microfabrication technologies.

The simplest technique for 3-D microfabrication is the multilayer process, which generates 3-D structures by stacking 2-D structures that have been fabricated by conventional 2-D lithography. One example of a multilayer process is the fabrication of microchannels [99]. Other methods for 3-D fabrication include multi-beam interference lithography [100], gray-scale lithography [101], moving mask lithography [102], and inclined lithography [103]. The purpose of this chapter is to describe the fabrication of 3-D microstructures by using inclined/rotational UV lithography.

3.1.2 Fabrication of 3-D Microstructures by Inclined/Rotational UV lithography

The fabrication of three dimensional microstructures using inclined X-ray exposure was first proposed by Schulz et al [104] in 1993. Beuret et al [91] used this idea to fabricate 3-D metallic structures which were created by electroplating Ni into a mold prepared by inclined UV lithography. This technology has since gone unnoticed for a decade by other researchers; however, recently several groups have used this technology for fabrication of complex 3-D structures [92-94, 105]. The basic concept of inclined UV lithography is the exposure of UV light through a mask at an angle, instead of conventional vertical exposure, to transfer a pattern into photoresist. A variety of 3-D structures can be formed by changing parameters such as : inclination angle, mask shape, exposure numbers, exposure angle, and exposure energy; For example, if a mask with square openings is used, a pattern of square rods will be transferred to a negative photoresist by conventional lithography. With the same mask, a vertical screen filter can be formed by two exposures at different angles, as shown in Figure 3.1.

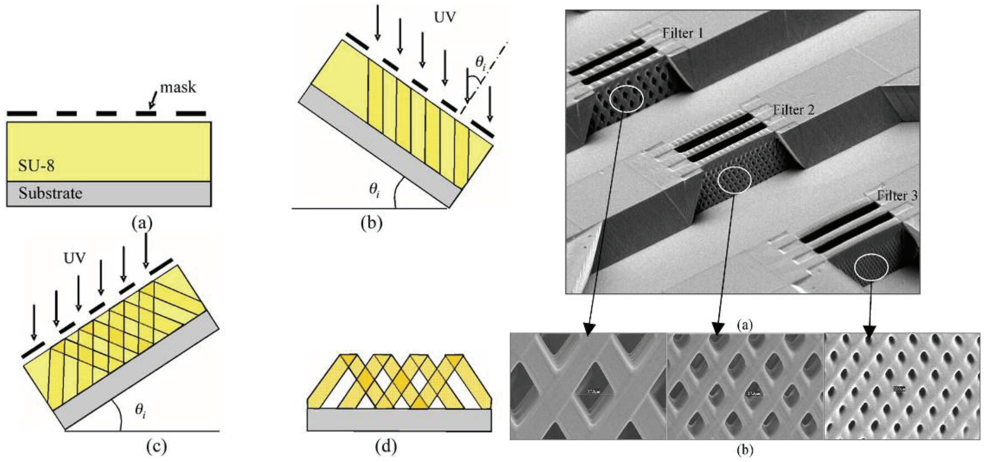

Figure 3.1 Fabrication of a vertical screen filter structure by the inclined UV lithography. Left schematic shows the fabrication process, and the SEM pictures show the fabricated structure [105]

Samples exposed to the UV light at an angle can also be continuously rotated, allowing creation of complex structures. Our group developed a mask/sample holder to perform inclined/rotational UV lithography [105] , as shown in Figure 3.2. The movable stage of this device can be tilted from 0° to ±90° and samples can be continuously rotated while in a tilted position.

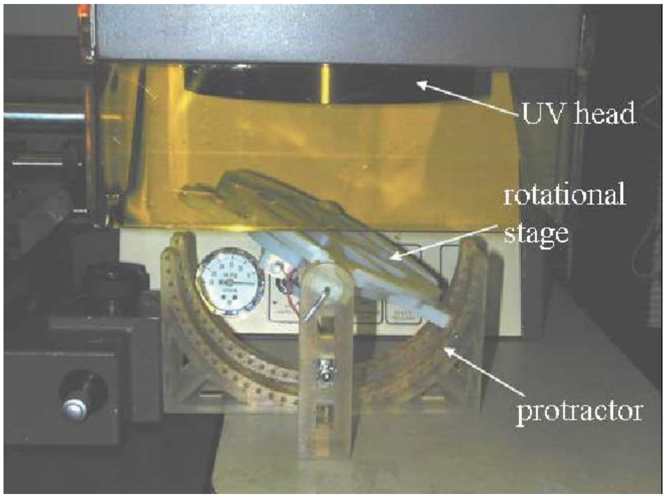

Figure 3.2 Mask/sample holder with tilting and rotational functionality [105]

Using this apparatus, structures with an oblique side wall were fabricated, as shown in Figure 3.3. To fabricate these structures, negative photo-epoxy (SU-8) with a thickness of approximately 500μm was spun on a glass substrate. Prior to the deposition of SU-8, the glass substrate was cleaned by Piranha etch (a 3:1 mixture of concentrated sulfuric acid (H_2SO_4) with hydrogen peroxide (H_2O_2)) for 15 min at 100°C, then washed with deionized (DI) water for 30 sec and dried with a nitrogen gun. The substrate was fully dried in an oven at 120°C for 30 min since water will result in poor adhesion between the substrate and the SU-8 and must be completely removed. After deposition, the SU-8 layer was baked on a hot plate at 100°C for 18 hrs and exposed to UV (365nm wavelength) in an inclined-rotational manner with an energy density of 9000mJ/cm^2. After exposure, the sample was baked on a hot plate at 100°C for 30 min, and then developed in propylene glycol methyl ether acetate (PGMEA). Finally, the sample was washed with isopropyl alcohol (IPA) and dried using a nitrogen gun. If the surface of the sample becomes white during IPA washing, it indicates that the sample is not fully developed. Therefore, the samples were developed in PGMEA until they do not become white during IPA washing.

A truncated cone-like structure was fabricated with a flat-square top using a mask with square openings. Due to the effect of rotation during exposure, the bottom of the structure was a circular shape. When a mask with ring openings was used, nozzle-like structures were formed, and the nozzle opening can be adjusted by the size of a pattern on a mask. With a mask for pad-feeding line, a 3-D structure with tapered side walls was formed.

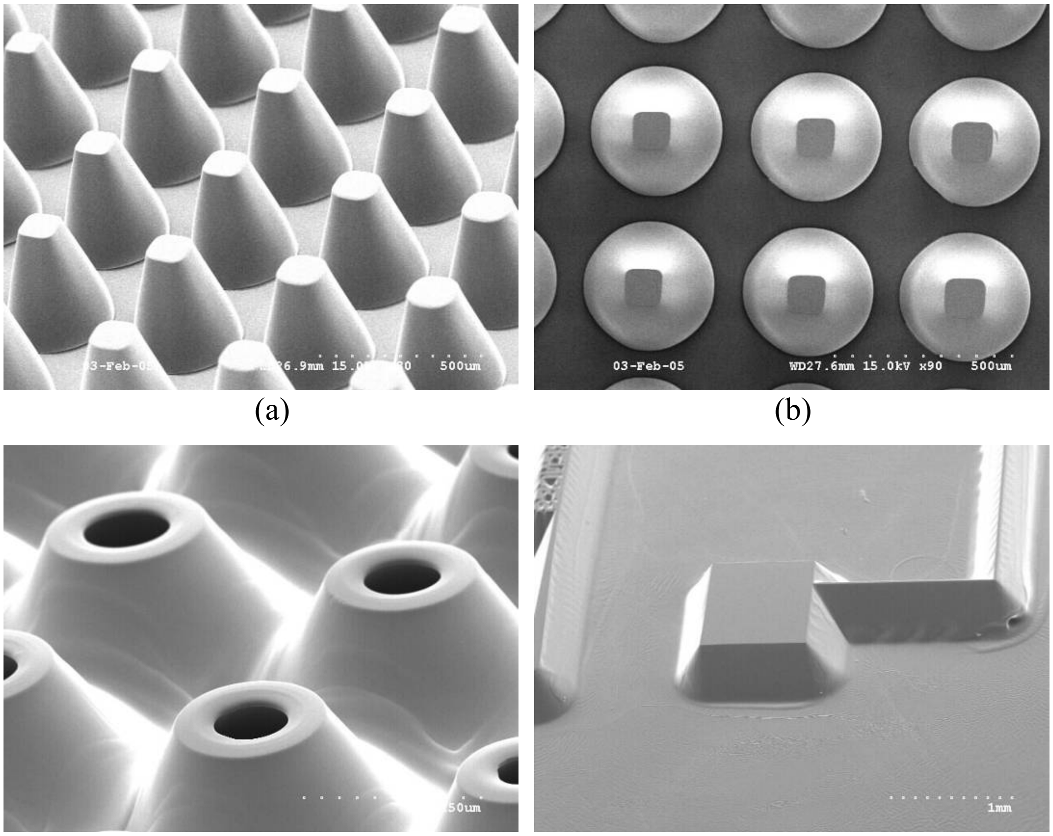

(a) (b) (c) (d)

Figure 3.3 Fabricated structures with the inclined/rotational lithography using different masks; (a) and (b) square openings, (c) ring openings, and (d) pad and feeding line

3.1.3 Fabrication of 3-D Microstructures by Inclined/Rotational UV Lithography Combined with Micromolding

In the previous section, a direct 3-D fabrication method by inclined/rotational lithography was discussed. Although this technique is capable of creating complex 3-D microstructures, it has limitations on the shape of the structures; 1) the top surface of the fabricated structures is typically flat, and 2) the heights of the structures protruding from the same substrate are the same. This technical limitation can be overcome by combining inclined/rotational UV lithography with micromolding.

This fabrication process begins by forming the negative shape of a final structure, known as the “mold,” instead of the direct formation of a final structure as discussed in 3.1.2. The basic concept in this process is that both the mask dimensions and the incident angle of UV light application control the depth of the mold. Therefore, structures with various heights can be formed simultaneously with a single mask. In addition, this technique is especially useful for fabricating structures with sharp tips such as microneedles for transdermal drug delivery, as well as 3-D microelectrode arrays for detecting signals from the brain.

A rigid SU-8 mold is fabricated using inclined UV lithography to form negative concave shapes of various depths as shown in Figure 3.4a and b. This rigid mold is used to produce a mold master (Figure 3.4c) from Polydimethylsiloxane (PDMS) or other suitable material (such as Ni in the case of electroplating). The mold master is then used to create a flexible replica (Figure 3.4d) of the original rigid mold; this flexible mold can be made from PDMS. Polymer microstructures with various heights are then fabricated using the flexible mold (Figure 3.4e and f).

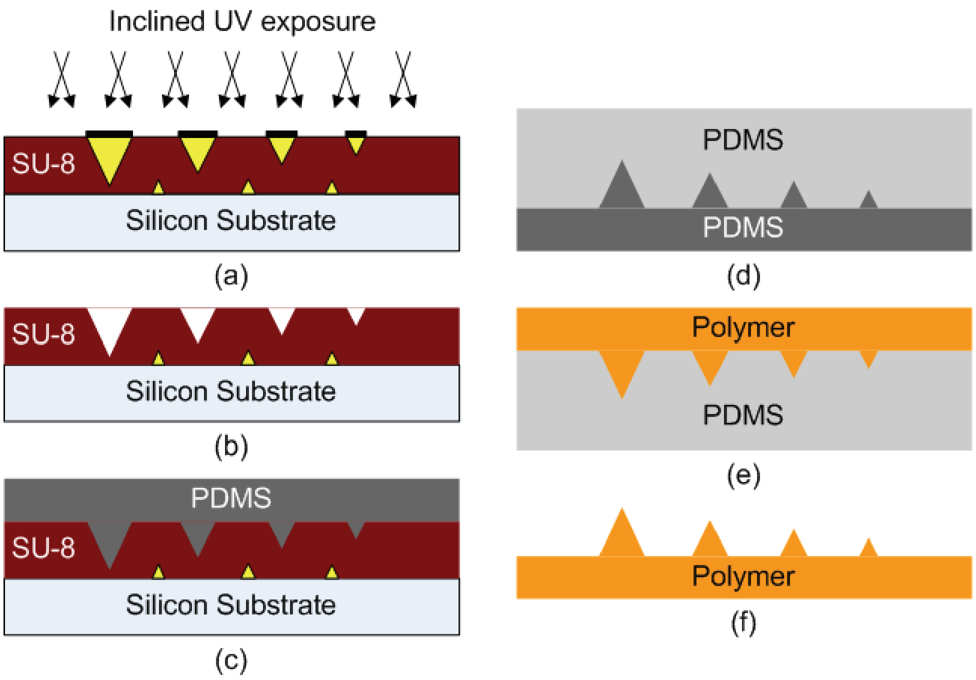

Figure 3.4 Fabrication steps for 3-D microstructures with variable heights; (a),(b) creation of SU-8 mold, (c) creation of mold master, (d) creation of flexible mold, (e) making final structure from polymer of choice, and (f) de-molded final structure

Once the rigid SU-8 mold is fabricated, a mold master can be copied from the mold by filling the mold with appropriate materials. Because the mold is rigid, a flexible material is suitable for casting due to the ease of separation, as compared to rigid materials. In this study, PDMS was chosen as a casting material due to its flexibility and low surface energy, which means it does not require a releasing agent for separation from the mold. PDMS is widely used in the MEMS field for microfluidics and optical applications. Its chemical formula is $(C_2H_6OSi)_n$, and its chemical structure is shown in Figure 3.5.

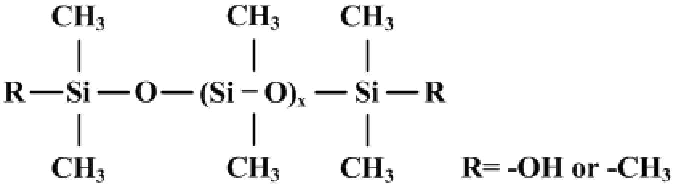

$$\mathrm{R-\underset{CH_3}{\overset{CH_3}{Si}}-O-(\underset{CH_3}{\overset{CH_3}{Si}}-O)_x-\underset{CH_3}{\overset{CH_3}{Si}}-R} \qquad \mathrm{R= -OH\ or\ -CH_3}$$

Figure 3.5 Chemical structure of polydimethylsiloxane (PDMS)

Commercially available PDMS (Sylgard 184, Dow Corning Corp., USA) has two components, base and curing agent, and the mixing ratio is 10:1 based on weight (base:curing agent). The two components of PDMS were mixed well and the mixture was degassed in a vacuum chamber before casting in an SU-8 mold. The degassed PDMS was then cast into the mold and was degassed again in a vacuum chamber after casting. If the mold does not contain high-aspect-ratio concave shapes, the second degassing process is not necessary because bubbles entrapped inside the shallow mold will disappear naturally during the curing process. The cross-linking process occurs at room temperature, but can be accelerated at higher temperatures. Usually, it takes 48 hours to form fully-cured PDMS at room temperature; however, only 1 hour is required for curing at 100°C. In this study, PDMS was cured at 50°C in a conventional oven for 8 hours.

After curing the cast PDMS, it was separated from the SU-8 mold and attached to a polystyrene container, which defines the size of a flexible mold. Before casting PDMS into the container to form a flexible PDMS mold, the PDMS master was treated with CHF_3/O_2 gas mixture (45sccm/5sccm, 200mTorr, 200W) using reactive ion etching (700 Series Wafer/Batch Plasma Processing System, Plasma-Therm Inc., St. Petersburg, FL) for 15 sec to avoid strong adhesion between PDMS surfaces. The other method used to create a PDMS mold from a PDMS master is to coat a PDMS mold with Au, because the adhesion between Au and PDMS is poor. One drawback of this method is that heat is generated during the Au deposition process, causing thermal expansion of PDMS. This thermal expansion results in the formation of wrinkles around the structure, which are copied to the PDMS mold after demolding from the PDMS master. Once the PDMS mold is fabricated, the final structure can be formed by casting the desired polymer into the mold. Several methods for polymer casting will be discussed later.

Using the fabrication process discussed above, 3-D microstructures were fabricated with a single mask. To prepare a thick (>300μm) SU-8 layer, SU-8 2025 was poured on a pre-cleaned silicon wafer instead of spin-coating. It is usually possible to define a 300μm thick SU-8 layer by spin-coating, and multiple coating can be applied to deposit even thicker layer; however, the advantage of the "pouring" method is that it does not require multiple baking steps, thus, the processing time can be reduced. The final thickness of the SU-8 layer can be estimated using the density of SU-8 and the solid content in SU-8. For example, the density of SU-8 is 1.219 g/cm^3 and SU-8 2025 contains 68.55% of solid. Using this information, it is possible to calculate the amount of SU-8 needed for a specific thickness by Equation 3.1.

$$A = \frac{\rho \times t \times 10^{-2}}{C_s} \ \text{[g/cm}^2\text{]} \tag{3.1}$$

where ρ is the density of SU-8, t is the target thickness in microns, and C_s is the solids content in percent, respectively.

To make a 500μm thick SU-8 layer, approximately 0.089 g/cm^2 of SU-8 2025 was poured on and spread over the silicon substrate. The sample was then baked on a hot plate at 100°C for 18 hours. Baking causes the SU-8 layer to form a flat surface without an edge bead, due to self-planarization. The sample was cooled slowly to avoid delamination and/or crack formation from a mismatch of the coefficient of thermal expansion between the SU-8 and the substrate and then exposed in an inclined/rotational manner under a UV lamp. The total energy density delivered to the sample was 9000mJ/cm^2. Post-exposure baking (PEB) was then performed on a hot plate at 100°C for 30 min and the sample was cooled down slowly from 100°C to room temperature by turning off the hot plate.

Development of the sample immediately after PEB frequently causes cracking of the structure and/or delamination from the substrate; therefore, the sample was further cooled down at room temperature for at least 1 hour before development. To develop the sample, it was immersed in PGMEA and agitated to accelerate development. When developing a high-aspect-ratio concave structure, it was helpful to place the sample upside down using a sample holder and agitating the solvent bath with a magnetic bar stirring underneath it. After development, the sample was dried and examined using both an optical microscope and a scanning electron microscope (SEM). Fabricated SU-8 molds are shown in Figure 3.6.

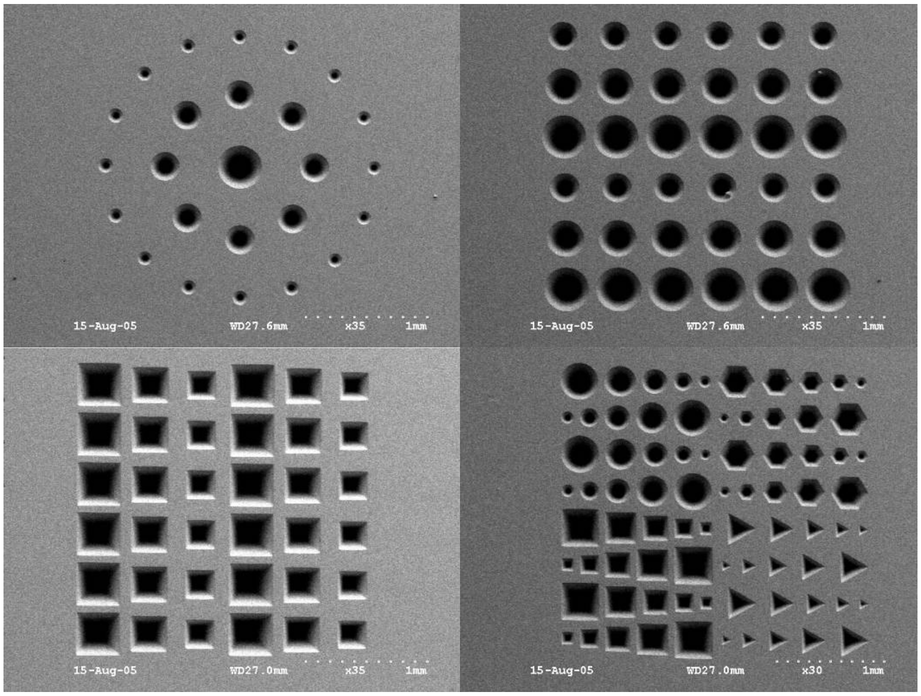

Figure 3.6 Fabricated SU-8 molds by inclined/rotational UV lithography

In principle, any moldable material can be used to make the master from a mold. However, it is desirable to use a flexible material for rigid molds that bear high-aspect-ratio concave structure, e.g. microneedles. High resolution which enables the replication of targeted small features is also necessary. Although PDMS is a suitable material that meets these criteria, it is easily torn by an external shear force, which can happen when the master is separated from the mold, especially when it is not fully cured. However, this drawback is reasonable because PDMS master structures are easy to create quickly.

Another approach for fabrication of a master structure from a rigid mold is to electroplate metal into the mold. Nickel (Ni) is suitable material for this purpose because it has appropriate mechanical and chemical properties. In this work, a commercially available Ni plating bath (Watts Nickel, Technic Inc., Cranston, RI) was used with a current density of 10 mA/cm^2, which gave an approximate 15 μm/hour deposition rate. Before electroplating Ni, the mold was coated with a Ti/Cu seed layer (300Å/5000Å). The electroplated Ni was separated from the mold by etching a Cu layer in copper etchant (saturated $CuSO_4$ in NH_4OH). Fabricated master structures created by either PDMS casting or Ni electroplating are shown in Figure 3.7.

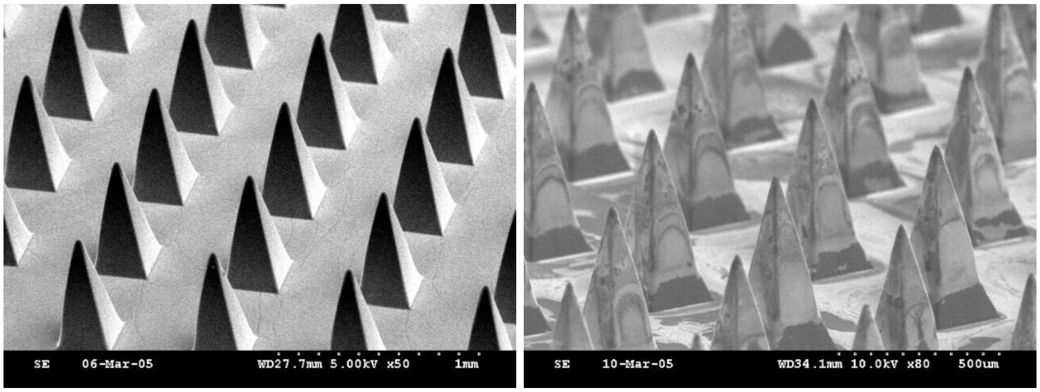

(a) (b)

Figure 3.7 Fabricated master structures from different materials; (a) PDMS and (b) Ni

After fabrication, the master of either PDMS or Ni was placed into a polystyrene (PS) container, and PDMS was poured into the container. Because the glass transition temperature (T_g) of PS is 95°C, PDMS needs to be cured at temperatures below the T_g. In this study, PDMS was cured at 50°C for 8 hours in a conventional oven. If a metal container was used, PDMS could be cured at higher temperatures. The PDMS master was treated with CHF_3/O_2 gas mixture before casting PDMS onto the master to prevent strong adhesion. When using a Ni master, this step was not required, because strong adhesion does not occur.

Once the flexible PDMS mold was fabricated, it was possible to cast various moldable materials into the mold. In this study, polymethymethacrylate (PMMA), SU-8, polyurethane (PU) and polylactic acid (PLA) were used for the fabrication of 3-D microstructures as shown in Figure 3.8.

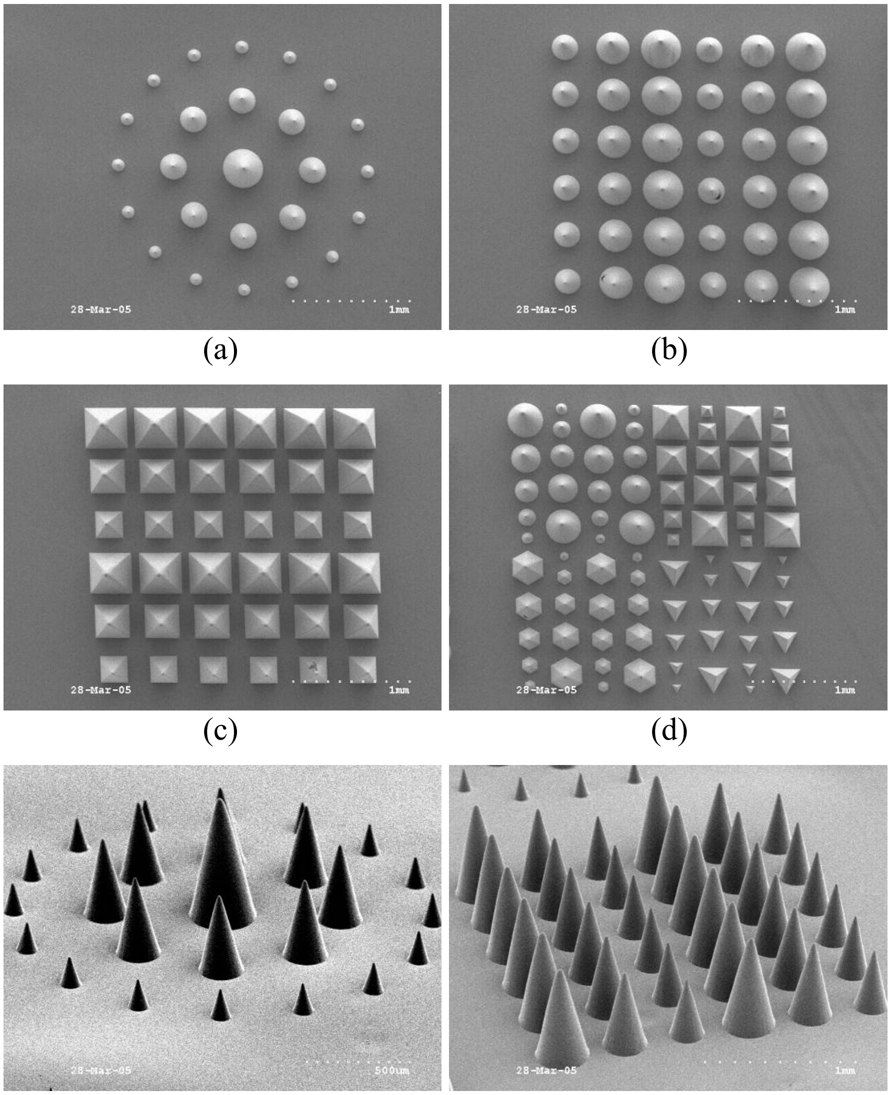

(a) (b)

(c) (d)

(e) (f)

Figure 3.8 Fabricated 3-D microstructures of varying heights; (a)-(d) Top view, and (e)-(h) Oblique view

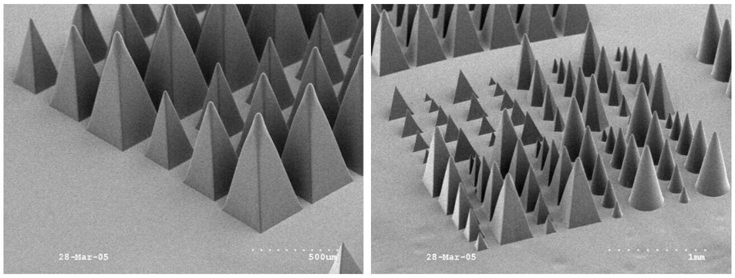

(g) (h)

Figure 3.8 continued

The fabricated microstructures shown in Figure 3.8 confirmed that it was possible to fabricate 3-D microstructures of varying heights by combining inclined/rotational UV lithography with micromolding technology. The mask sets used in this experiment were basic shapes, including circles, squares, triangles, and hexagons. These shapes produced microneedle-like microstructures with sharp tips. Using this technology, it is possible to fabricate various microstructures with sharp tips without using the wet/dry etching technique. In addition, complex 3-D microstructures can be easily fabricated using proper mask designs, as shown in Figure 3.9. This fabrication process is simple and cost-effective compared to other 3-D fabrication processes.

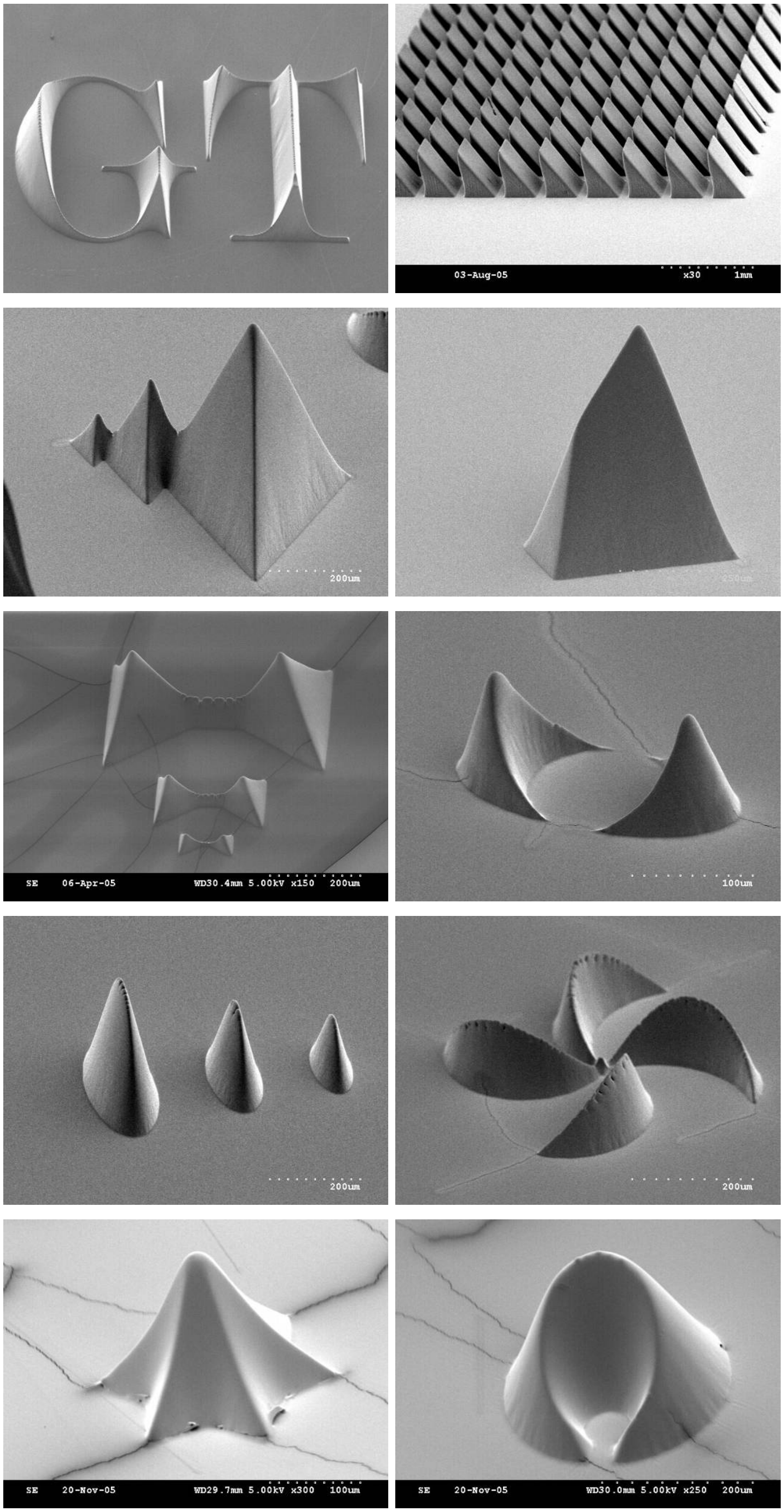

Figure 3.9 Fabricated complex 3-D microstructures

In conventional lithography, the thickness of photoresist determines the final thickness of the structure. This is typically also true for the fabrication of “positive” structures by means of inclined lithography. However, in the case of the fabrication of “negative” structures by inclined lithography, the depth of a mold is determined by parameters such as mask dimension and inclination angle. Therefore, the targeting depth of a mold should be calculated based on such parameters, and the thickness of the SU-8 layer should be thicker than the calculated depth of the mold. The depth of a mold can be calculated by Snell’s law and trigonometry as follows: The incident UV light with angle θ_1 will be refracted at the interface between air and the mask (glass), resulting in changing the incidence angle θ_1 to θ_2, and the light will be refracted one more time at the interface between the mask and SU-8 (Figure 3.10). The final angle of the incident UV will be θ_3, and the relationship between angles is given by Snell’s law in Equation 3.2.

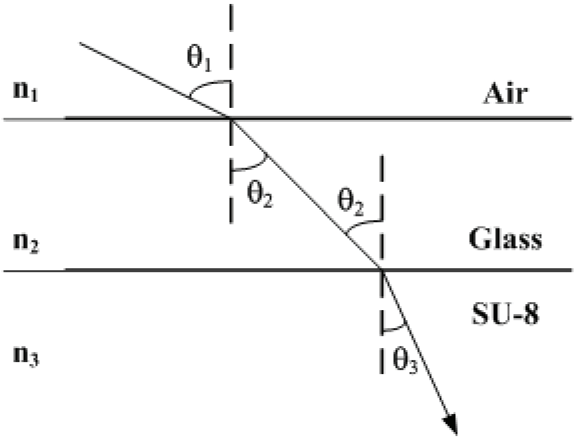

Figure 3.10 Schematic description of refraction of light at the interfaces with different refractive indices

$$n_1 \sin\theta_1 = n_2 \sin\theta_2 = n_3 \sin\theta_3 \text{ , } \theta_3 = \sin^{-1}\left(\frac{n_1}{n_3}\sin\theta_1\right) \tag{3.2}$$

where n_1,n_2, and n_3 are the refractive indices of air, glass, and SU-8, respectively.

Once the refractive angle θ_3 is calculated, the depth of the mold is given by Equation 3.3 as follows:

$$Depth = \frac{d}{\tan\theta_3} \tag{3.3}$$

where d is distance between the centroid of the mask footprint and the boundary of the mask footprint.

For example, if a mask bears circular dark fields with different diameters: 50μm, 100μm, and 200μm, and the incident angle θ_1 is 30°, which corresponds to θ_3 of 17.3° (the refractive index of SU-8 used for the calculation was 1.68 [105]) then the depth of each circular pattern can be calculated as 80μm, 160μm, and 320μm, respectively.

From equation 3.2, it is possible to determine the theoretical limit of the structure angle, which is designated as θ_3 in Figure 3.10. When the incident angle θ_1 equals 90°, the resultant structural angle is approximately 36.5°, which is the theoretical limit. This limitation is dependent on the optical property of the mold material (i.e. the refractive index of the material). The refractive index of SU-8 ranges 1.6 to 1.7, depending on the wavelength of the incident UV light [106], and this limits the structure angle to 38.7° to 36°.

Using methods described in the literature [107], it was possible to fabricate ultra-thick SU-8 structures up to 2 mm. However, substrate bowing due to stress induced by the SU-8 layer was observed as the thickness of the SU-8 layer increased. This effect can be resolved by using a thick substrate that can resist the stress from the SU-8 layer. In addition, the optimization of the process parameters such as baking temperature and duration, as well as exposure energy can minimize substrate bowing by reducing thermal stress.

It has been reported that ultra high-aspect ratio (higher than 15) structures can be realized with SU-8 [107, 108]. Open field structures such as pillars can be easily developed in solvent, but there is limitation in developing structures with narrow openings. This is due to the difficulty of refreshing the developer in small and deep holes. Theoretically, the tip of the mold should be infinitely sharp. However, it was found that approximately 5 μm of tip diameter was achievable with the standard development procedure (dipping and agitating). The sharpness of the mold could be improved if other development technologies are applied. Ultrasonic development technique would be one of the promising techniques for developing high-aspect ratio structures [108].

The procedure of micromolding consists of two steps: 1) filling a material into a micromold, and 2) separating the material from the micromold after solidification. The filling process depends on both the viscosity of the cast material during the process and the depth of the mold. In experiments, a highly viscous material (molten PLA) was successfully cast into a mold with an aspect ratio of 7.5 [109]. Separation of the cast material from the mold without breakage is a critical step for successful fabrication. During the separation step, the molded structure experiences shear stress which increases as the aspect ratio increases. For successful separation, the molded structure must be mechanically strong enough to resist the stress. In other words, the limit of the achievable aspect ratio of the molded structure depends on its mechanical strength and geometry.

In conclusion, the developed technology is beneficial for fabrication of complex 3-D microstructures from a single mask. It would therefore be possible to construct much more complex 3-D structures by adding additional lithography steps.

3.1.4 Prediction of the Shapes of Molds and Molded Microstructures

The geometry of a final structure can be easily determined if the shape of the mask footprint is simple, e.g. triangle, square or circle; the final structures of these shapes are tetrahedron, quadrangular pyramid, and cone, respectively. Prediction of the shape of the final structure becomes more difficult as the complexity of the mask footprint increases; however, ray-tracing approaches can be utilized to gain insight as to the final shape.

Prediction of the final shape can be achieved using a computer-aided design (CAD) tool such as AutoCAD (Autodesk, Inc., San Rafael, CA, USA). The concept of inclined/rotational UV exposure can be described as the UV light passes at an incident angle through a clear field of a mask. The light then sweeps the boundary of a mask footprint while keeping the incident angle constant. SU-8 is a negative-tone photoresist; therefore, the region swept by the UV light is solidified by photon-induced cross-linking. This effect can be mimicked using CAD software by extruding a structure with a hole corresponding to a mask footprint with a tapered angle as shown in Figure 3.11.

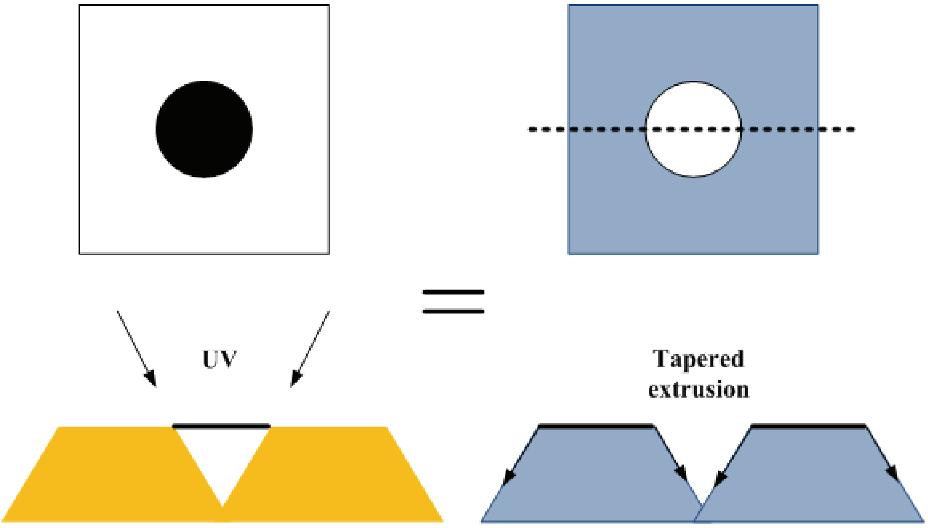

(a) (b)

Figure 3.11 Concept of tapered extrusion method to predict a shape of a mold; (a) inclined/rotational UV lithography, and (b) tapered extrusion of a 2-D geometry having a hole inside

To verify this concept, a mask with microstructures of various heights was designed with AutoCAD. Figure 3.12 shows the mask footprints and the predicted shape of the mold after the tapered extrusion procedure.

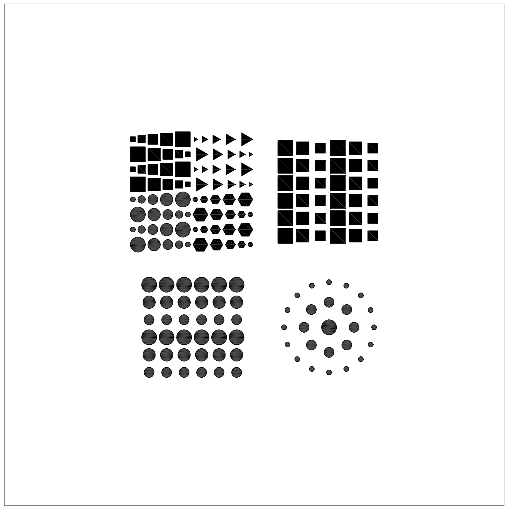

(a)

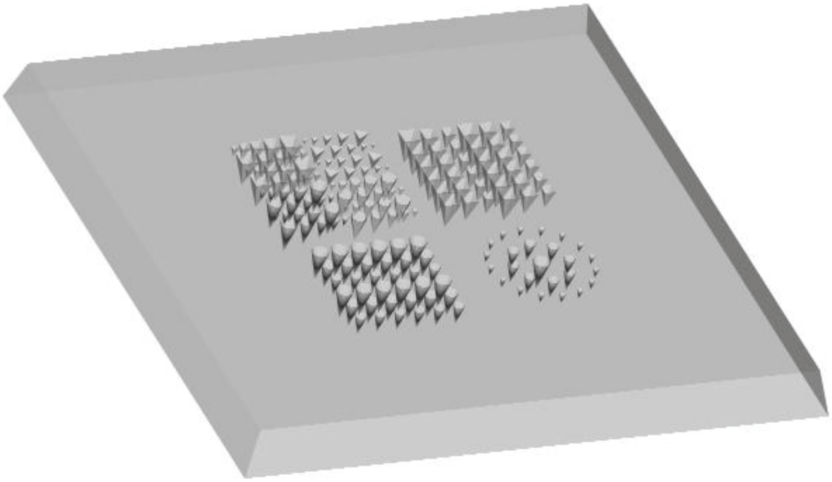

(b)

Figure 3.12 Verification of tapered extrusion approach for prediction of mold formation; (a) the mask footprints, and (b) the predicted shape of the mold

By extending this approach, it is possible to predict the shape of a molded structure directly from the mask footprint by extruding the mask footprint itself at an angle. The conceptual view of the tapered extrusion of an arbitrary 2-D shape is shown in Figure 3.13.

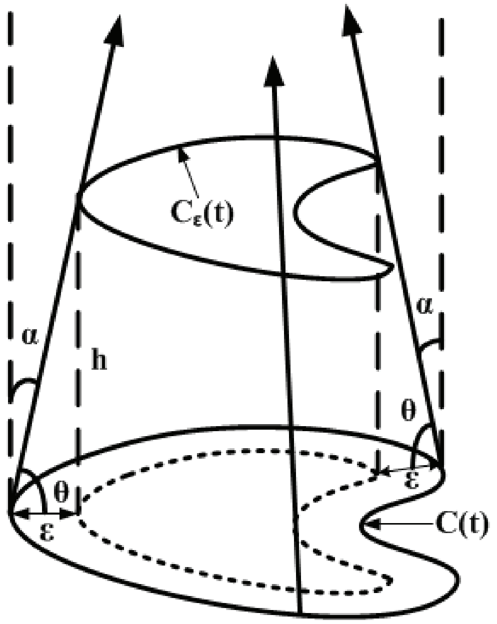

Figure 3.13 Conceptual view of tapered extrusion of arbitrary 2-D geometry

Assume that an arbitrary parametric curve $C(t) = (x(t), y(t))$ defines the boundary of a mask footprint in a 2-D space. If we extrude this curve with a tapered angle α, the curve which defines the boundary of the extruded object at a certain height *h* can be expressed by $C_\varepsilon(t)$. Since the tapered angle α is constant along the object, there is a relationship between $C(t)$ and the projection of $C_\varepsilon(t)$ on the 2-D plane as follows:

$$C_{\varepsilon}(t) = C(t) - \varepsilon \cdot N(t) \tag{3.4}$$

where $N(t)$ is the unit normal vector of $C(t)$:

$$N(t) = \left(\frac{y'(t)}{\sqrt{x'(t)^2 + y'(t)^2}}, \frac{-x'(t)}{\sqrt{x'(t)^2 + y'(t)^2}} \right), \text{ and } \varepsilon > 0.$$

At height *h*, the distance between two curves, ε, can be expressed by

$$\varepsilon = \frac{h}{\tan\theta} = h \cdot \tan\alpha \tag{3.5}$$

For example, a circle with radius R is expressed in a parametric form as

$$C(\theta) = (R\cos\theta, R\sin\theta) \tag{3.6}$$

and its normal vector $N(t)$ is expressed as

$$N(\theta) = \left(\frac{y'(\theta)}{\sqrt{x'(\theta)^2 + y'(\theta)^2}}, \frac{-x'(\theta)}{\sqrt{x'(\theta)^2 + y'(\theta)^2}} \right) = \left(\frac{R\cos\theta}{R}, \frac{R\sin\theta}{R} \right) = (\cos\theta, \sin\theta) \tag{3.7}$$

Consequently,

$$C_{\varepsilon}(\theta) = C(\theta) - \varepsilon \cdot N(\theta) = ((R-\varepsilon)\cos\theta, (R-\varepsilon)\sin\theta) \tag{3.8}$$

Equation 3.8 indicates that the boundary of the extruded circle decreases with the height due to the increase of ε along the height while keeping its original shape, and finally converges into a point when $\varepsilon = R$.

From the above equations it can be deduced that the shape of the cross-section of an extruded object at a certain height can be predicted by the inner offset of a mask footprint, and the final 3-D structure can be predicted by interpolating the boundaries at each height. Because the tapered extrusion process is not simply done by scaling the original footprint along the height but done by "offsetting" the original footprint, the shape of an original mask footprint is not preserved along the height if the original mask footprint is not symmetric with respect to its centroid. For example, the cross-section of a trapezoid becomes a triangle at a certain height as shown in Figure 3.14.

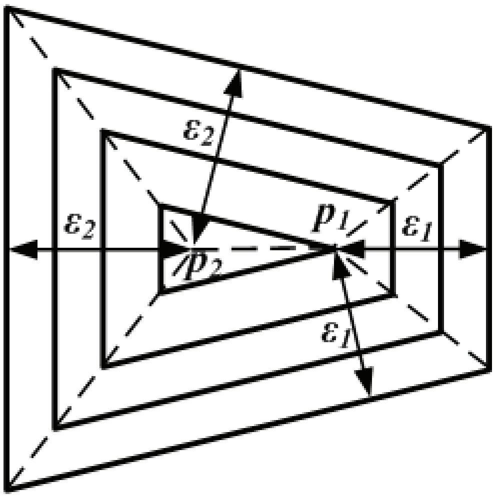

Figure 3.14 Diagram of inner offset of a trapezoid

When the trapezoid shrinks to a triangle at the point p_1, the offset distance is ε_1. Given a tapered angle α, the height at the points p_1 and p_2 can be calculated with equation 3.5. As shown in the diagram, the structure will be a form of a tapered structure which has two vertices at different heights. This result indicates that a tapered-tip microneedle structure can be fabricated by inclined/rotational UV lithography of a trapezoidal mask footprint, as shown in Figure 3.15.

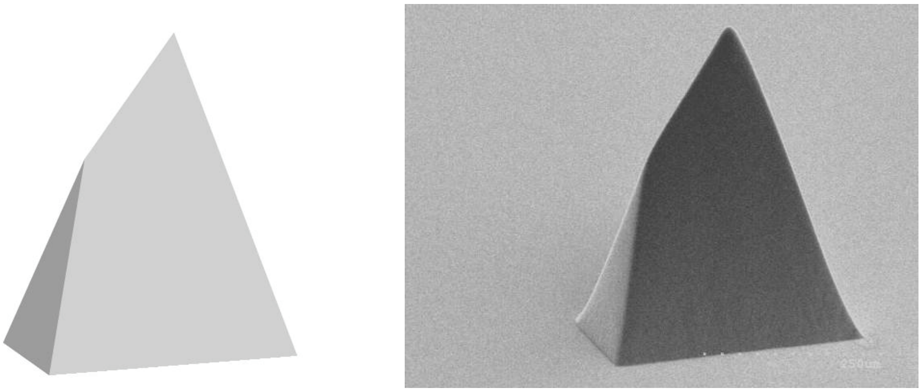

(a) (b)

Figure 3.15 Tapered-tip microneedle structure; (a) predicted structure by tapered extrusion, and (b) fabricated structure

It was proven that the tapered extrusion method could predict both the shape of the mold as well as a molded structure. Since the tested models were relatively simple shapes, a more complex mask footprint was created to test the prediction, as shown in Figure 3.16.

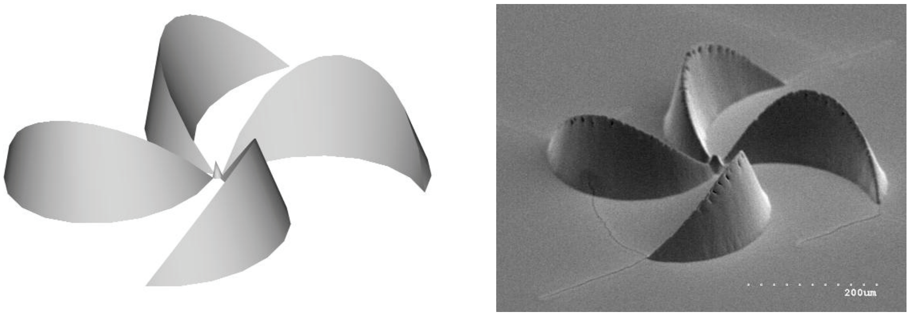

(a) (b)

Figure 3.16 Vane-like microstructure; (a) predicted model, and (b) fabricated structure

The mask footprint was composed of four crescents with a circle at the center. The predicted feature (3.16a) was a vane-like structure, and the fabrication results confirmed the capability of this approach (3.16b). However, the predicted model is not entirely similar to the fabricated model for several reasons: 1) the tapered extrusion process is performed by creating inner offsets of given geometry. For simple geometries such as a circle, triangle, etc., the exact inner offsets can be computed. However, there exists a fundamental difficulty of exact offset computation [110] for complex geometries. In these cases, the offset is estimated by several approximation methods [111, 112], resulting in errors which cause the prediction to differ from the actual structure. 2) Because the final structure is formed from a mold, shrinkage of the molded material cannot be avoided. The final dimension of the fabricated structure is strongly dependent on the shrinkage rate of the molded material. In addition, the sharpness of the mold is limited by factors such as the resolution of SU-8 and other molding materials, as well as by reflection of the UV light from the bottom of the substrate. During experiments, it was found that the limitation of the sharpness created by a mold was approximately 5 μm when measured in diameter. 3) Finally, if SU-8 deposited during mold fabrication is not perfectly flat, there exists a tiny gap between the mask and the deposition, which will affect the shape of the final structure.

3.2 Metallization of 3-D Microstructures

3.2.1 Introduction

To implement electrical functionality to microstructures, a metallization step is required. Using conventional methods, metal is patterned on the surface of a substrate by several techniques, including: wet etching, lift-off, and shadow mask. These techniques were originally developed for the metallization of 2-D structures; therefore, it has been difficult to apply these techniques for 3-D applications. These difficulties include the problem of conformal coating of photoresist on 3-D structures when using wet etching and lift-off, and the inherent gap between a shadow mask and the sample; both cases can result in poor resolution. Recently, researchers have reported methods for the metallization of 3-D structures, including spray coating of photoresist [113, 114], multi-step UV exposure [115], and electrodeposition of photoresist [114]. These methods show feasible results, and would be appropriate for metallization of 3-D structures. However, the 3-D metallization techniques discussed thus far require the sample to contact the mask, so it is not easy to apply these techniques when a sample bears high-aspect-ratio structures or for pointed structures such as microneedles. Therefore, it is essential to investigate a technology which enables metal patterning on high-aspect-ratio structures for the purposes of this work. To this end, laser ablation and metal transfer techniques were exploited and will be discussed in following sections.

3.2.2 Laser Ablation

Laser micromachining has been used for many applications such as micro-vias for chip interconnection, ink-jet printer nozzles, flat-panel displays, and biomedical devices [116]. Recently, laser micromachining has been widely used in the MEMS field for fabricating 3-D structures [117, 118], bio-microfluidics applications [119, 120], and thin polymer welding [121]. Compared to photolithography, laser micromachining provides advantages such as rapid prototyping, flexibility of materials, and simple processing. There are many types of laser systems available including: excimer, CO_2, IR, and Nd:YAG. Among them, the excimer laser has been widely used because it provides high resolution, low thermal damage, and can be used on a wide range of materials, many of which are polymers. In addition, excimer laser ablation can be used to pattern metal lines on high-aspect-ratio structures reported by our group [122, 123]. In these papers, parylene was used as a mold for electroplating, and the excimer laser was used to ablate the parylene layer. The concept of the fabrication process is shown in Figure 3.17.

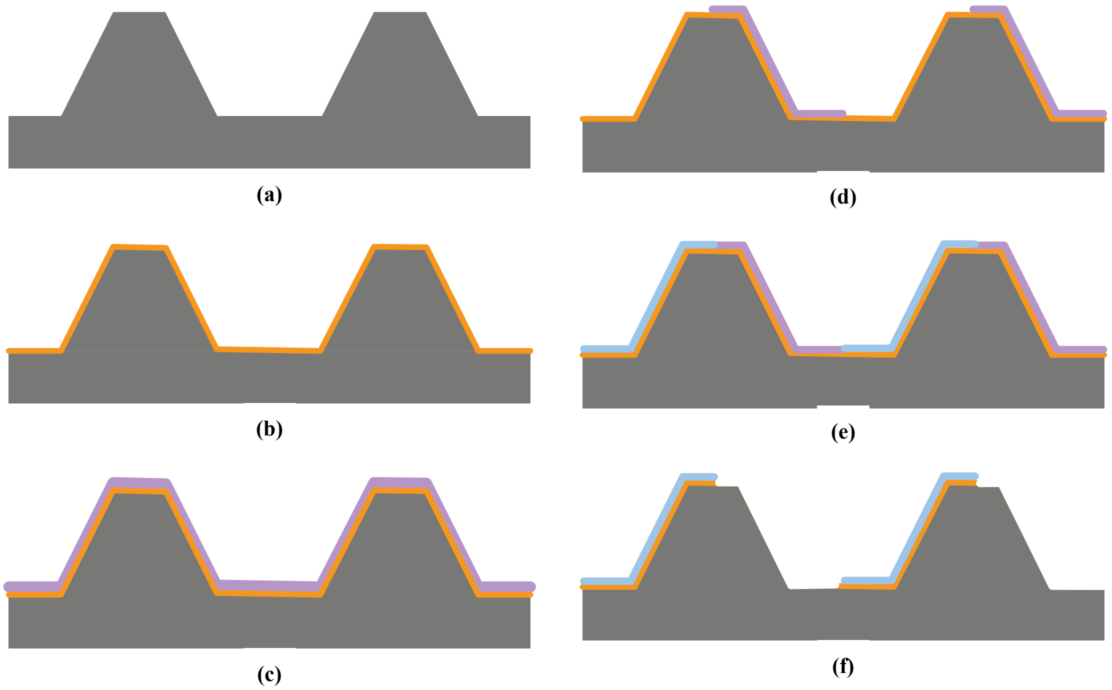

Figure 3.17 Schematic of the fabrication process for metallization on a 3-D structure

To fabricate metal lines on a 3-D structure (Figure 3.17a), a Ti/Cu seed layer was deposited over the sample (Figure 3.17b) followed by parylene deposition (Figure 3.17c), which serves to provide conformal sample coating. After parylene deposition, a mold for electroplating was formed by selective ablating of the parylene layer by the excimer laser (Figure 3.17d). Once the mold was formed, Ni was electroplated into the mold (Figure 3.17e), followed by removal of the parylene layer and the seed layer simultaneously (Figure 3.17f). This technique is suitable for forming metal lines on a 3-D structure.

It was also possible to make patterns on a seed layer directly by the excimer laser. Generally, the excimer laser has been used to process polymers because this laser is able to break polymer bonds by supplying photon energy, resulting in the chemical dissociation of the polymer into monomers which are volatile. The excimer laser is typically not powerful enough to ablate thick metals, but it was found that it was possible to ablate a thin layer of metal (~ 3000Å). The direct patterning method is especially suitable for applications that require electrical isolations, in which only a small portion of the metal layer needs to be removed. The fabrication process is shown in Figure 3.18.

The first step is the deposition of a seed layer (Ti/Cu) on a 3-D microstructure (Figure 3.18a). The excimer laser then scribes the desired pattern directly on the seed layer (Figure 3.18b). After laser scribing, the metal layer could be thickened by electroplating if required (Figure 3.18c). The fabrication results are shown in Figure 3.19.

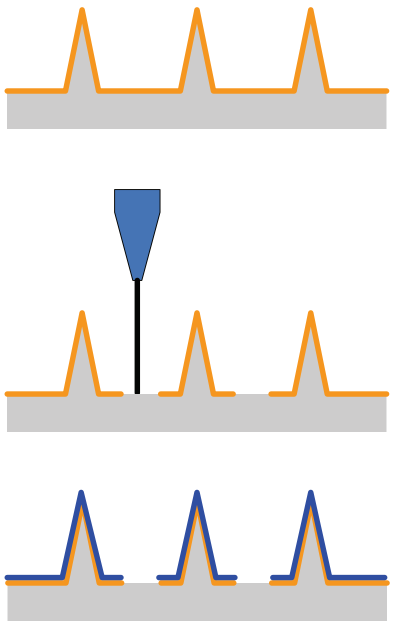

Figure 3.18 Fabrication process of direct patterning of metal layer by excimer laser

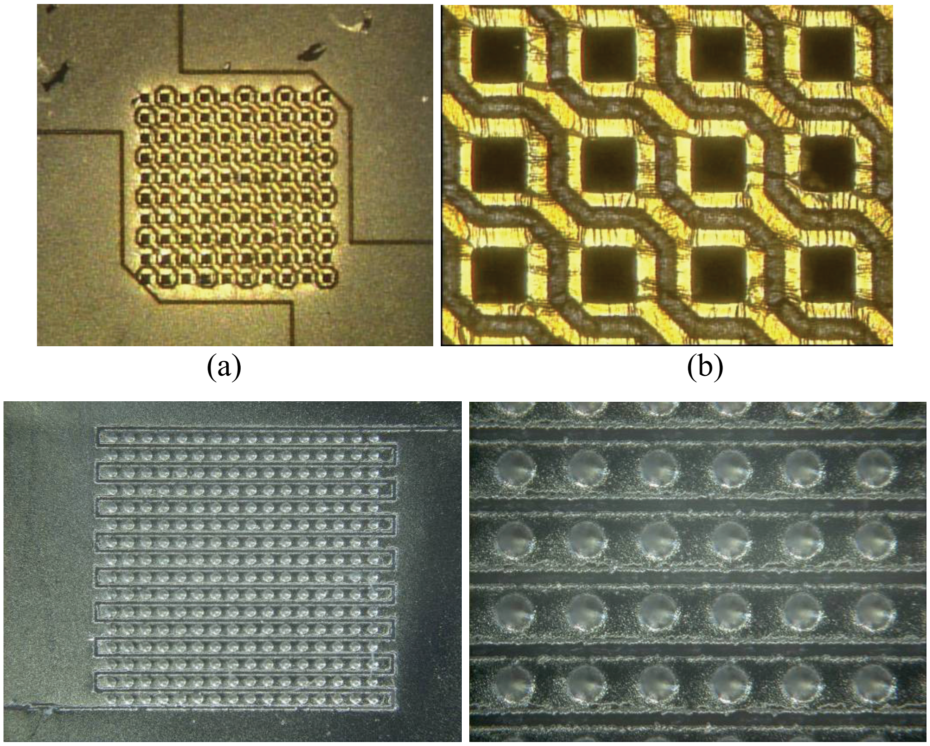
(a) (b)
(c) (d)

Figure 3.19 Optical micrographs of metal patterns fabricated by excimer laser ablation; (a) pattern on Au layer, (b) close-up view, (c) Ni electroplated after laser scribing, (d) close-up view

Figure 3.19a and b show the pattern scribed on Au surface. The substrate bears 10x10 pyramidal shaped microneedles, which are shown as black squares, and electrical isolation between the microneedles was realized by the excimer laser system (Resonetics Inc., Nashua, NH). To ablate a 2000Å thick Au layer, a metal shadow mask with a 700µm diameter hole was used, and the laser beam was de-magnified optically by 10 times, resulting in a 70µm beam diameter. The energy level of the system was 250mJ, and 20% of the energy was transmitted for ablation. The ablation was performed at a scribing speed of 100µm/sec.

Figure 3.19c and d show a 16x16 cone shaped metallized and isolated microneedle array formed using a 2000Å Cu seed layer. To develop this device, a metal shadow mask with a 500μm diameter hole was used at 10X de-magnification. The ablation process was performed at 200mJ with 25% power attenuation, and the scribing speed was 100μm/sec. After laser scribing, the sample was cleaned with a nitrogen gun, and a 20μm thick Ni layer was electroplated on top of the seed layer.

The laser ablation technique is limited in that it is not suitable for low-cost mass production because it is a serial process. Also, there is a problem with misalignment between CAD design for laser scribing and the fabricated device due to shrinkage of the material during micromolding. The misalignment issue becomes critical as the size of the mold increases, which is essential for mass production. In order to overcome these limitations, a self-aligned metallization process based on a double-layer metal transfer micromolding technique was developed.

3.2.3 Double-layer Metal Transfer Micromolding

Photolithography has been widely used in both industry and academia to fabricate metallic structures. Recently, an approach known as nanotransfer printing (nTP) was introduced to fabricate nano-scale metal structures for applications in plastic electronics [124]. The basic process of nTP is the deposition of a Au/Ti layer on a PDMS stamp, followed by oxidizing both the stamp and the substrate to form –OH groups on the surfaces. By brining the surfaces into contact with each other, TiO_x on the stamp chemically bonds to the substrate, resulting in the complete transfer of the Au/Ti pattern from the stamp to the substrate. This process utilizes covalent bonding, and thus is limited to systems in which covalent interactions occur. More recent research has reported that it is possible to perform nTP by noncovalent surface forces [125], which could expand the range of materials for nTP process. The schematic illustration of steps for noncovalent transfer printing is shown in Figure 3.20.

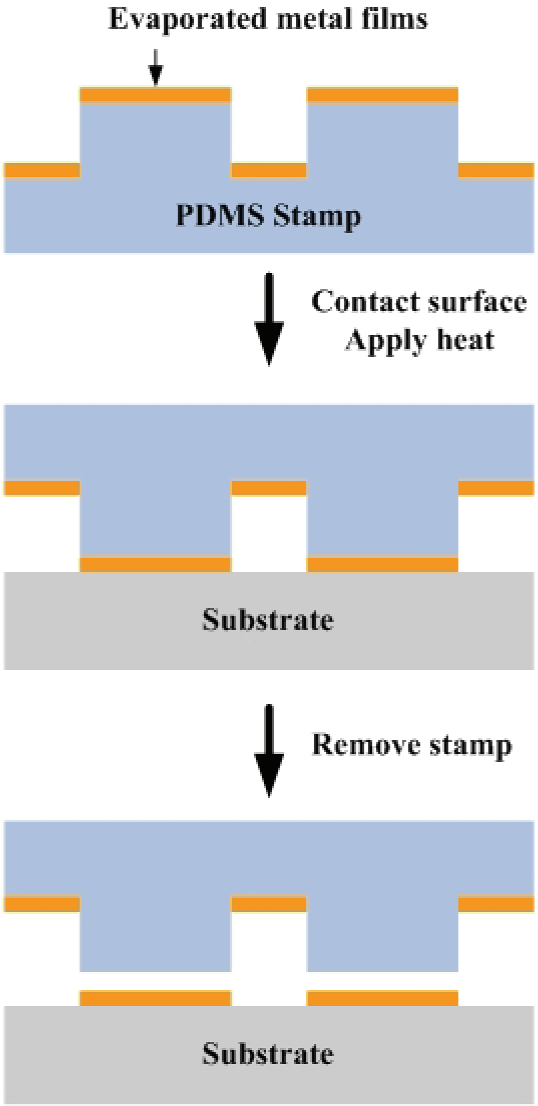

Figure 3.20 Schematic illustration of steps for noncovalent transfer printing [125]

The mechanism of noncovalent transfer printing is based on the different strengths of adhesion between PDMS-metal and substrate-metal interfaces. The relationship between the differences in the work of adhesion of those interfaces can be expressed as

$$W_{sub-metal} - W_{PDMS-metal} = (\gamma_{sub} - \gamma_{PDMS}) - (\gamma_{sub-metal} - \gamma_{PDMS-metal}) \qquad (3.9)$$

where γ_{sub} and γ_{PDMS} denote the surface energies of the substrate and the PDMS, and $\gamma_{sub-metal}$ and $\gamma_{PDMS-metal}$ denote the interfacial energies between substrate and metal and between PDMS and metal, respectively.

Since the surface energy of metal is usually much higher than the surface energies of the substrate or PDMS, the second term of the equation is small. Therefore, the difference in work of adhesion between surfaces can be regarded as the difference between the surface energies of the substrate and PDMS. In most cases, the surface energy of the substrate is higher than that of PDMS (19.8 mJ/m^2), such that metal can be transferred from PDMS to the substrate.

In this work, the principles of nTP were used to fabricate electrically active 3-D microstructures. A key innovation is the development of a self-aligned double-layer micromold approach, in which the nTP metallization isolation features are integral to the mold itself. Figure 3.21 illustrates the fabrication process of 3-D metal transfer micromolding.

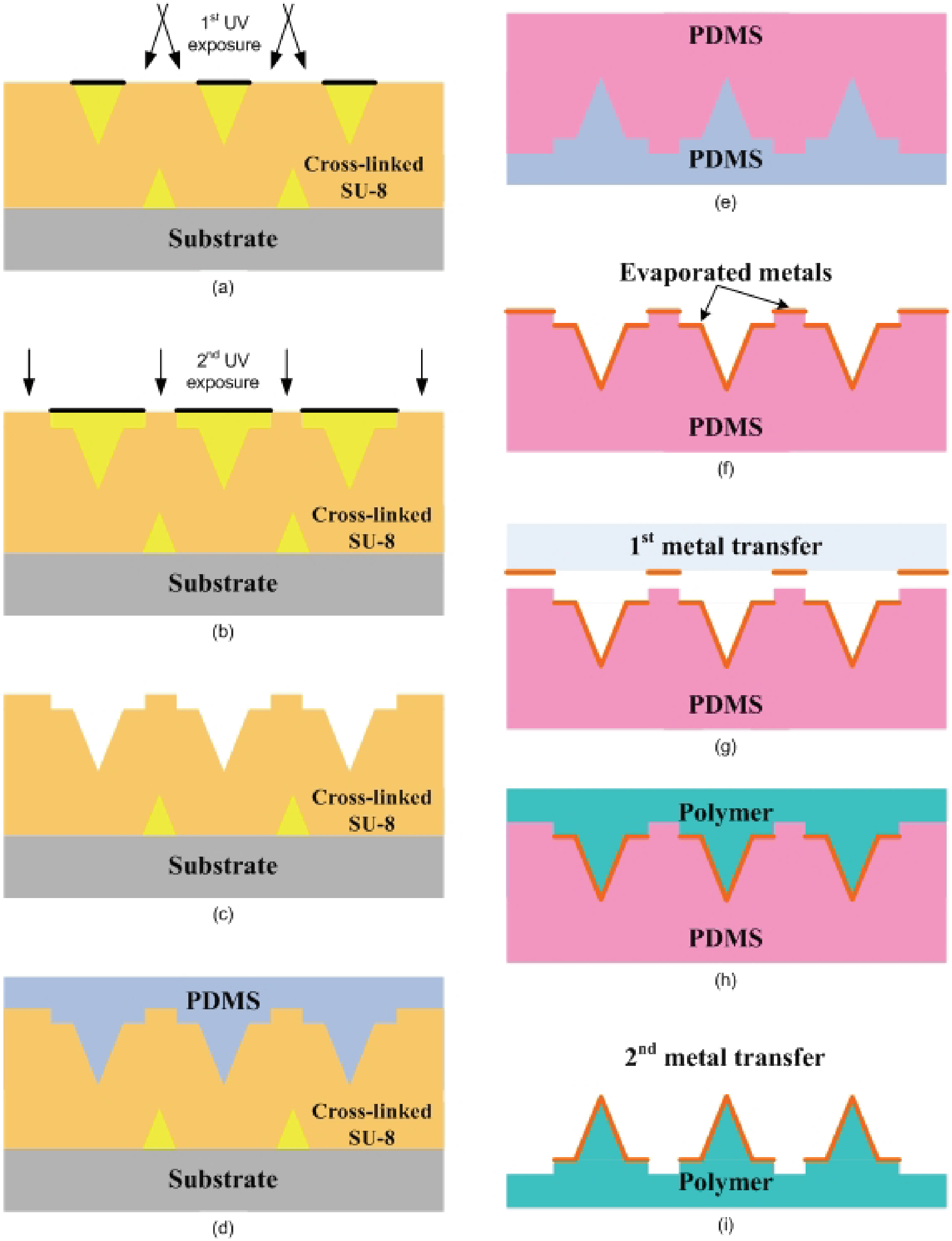

Figure 3.21 Schematic illustration of the fabrication process of 3-D metal transfer micromolding

To fabricate a double-layer SU-8 mold, the first layer of SU-8 was spun on a substrate, baked, and exposed at an angle to form a negative shape of the 3-D structure (Figure 3.21a). The first SU-8 layer was not developed prior to the second SU-8 layer being spun on top of it. The structure was then soft-baked in a conventional oven. The second UV lithography was performed with a mask, which defines the negative shape of desired metal patterns, and was done in a conventional way (Figure 3.21b). After post-exposure baking, the sample was developed in propylene glycol monomethyl ether acetate (PGMEA) (MicroChem Corp., Newton, MA), forming a double-layer SU-8 mold (Figure 3.21c). PDMS was then cast into the SU-8 mold (Figure 3.21d) to copy a negative of the mold (i.e., flexible master). After the fabrication of the flexible PDMS master, a PDMS mold was formed by casting PDMS onto the PDMS master (Figure 3.21e). Before casting PDMS onto the PDMS master, the surface of the PDMS master was treated with CHF_3/O_2 plasma to prevent it from adhering to the cast PDMS. Metal (Au or Au/Ti) was then evaporated into the PDMS mold by electron-beam evaporation, by this method the evaporated metal layer does not cover the side wall of the PDMS mold (Figure 3.21f). When a plate with high surface energy was brought into contact with the PDMS mold, the first metal transfer occurred so that the metal on the extruded part of the mold was selectively transferred to the plate (Figure 3.21g). After patterning the metal layer, a desired polymer was cast into the mold, cured, and separated. During the separation process, the second metal transfer occurred, resulting in the formation of 3-D metal-patterned microstructures (Figure 3.21h and i). The advantage of this process is that it does not require any photolithography or etching steps and enables the patterning of a metal layer on high-aspect-ratio 3-D structures with high fidelity. When compared to conventional technology for fabricating 3-D metallic structures, the 3-D metal transfer micromolding technique is a time and cost-effective process which is attractive to mass production.

Based on the technology mentioned above, a double-layer SU-8 mold for a 3-D microelectrode array (MEA) was fabricated, as shown in Figure 3.22. A silicon wafer was diced into 2cm by 2cm chips and cleaned in Piranha etch solution for 15 min. After cleaning, the substrate was rinsed with DI water for 1 min and dried with a nitrogen gun. The sample was then dehydrated at 120°C in an oven for 30 min. A 700μm thick SU-8 layer was coated on the substrate, and the sample was baked at 100°C on a hot plate for 24 hours. The sample was placed on the inclined/rotational stage with the mask, and exposed to UV light at an energy per unit area of 9000 mJ/cm^2. Post-exposure baking was done at 95°C on a hot plate for 30 min, and the sample was slowly cooled down to room temperature. Without developing the first SU-8 layer, the 2nd SU-8 layer was spun on the 1st SU-8 layer with a thickness of 80μm. The spin-coating condition for the 80μm thick SU-8 layer (SU-8 2025) was composed of two steps: 500 rpm for 5 sec with acceleration of 100 rpm/sec, and 1000 rpm for 30 sec with acceleration of 300 rpm/sec. The sample was then baked at 95°C in an oven for 30 min. The second mask was aligned with the sample, and an energy density of 800mJ/cm^2 was exposed through the mask to pattern the 2nd SU-8 layer. After the second UV exposure, the sample was post-exposure baked at 95°C in an oven for 15 min. Once the post-exposure baking was done, the sample was cooled down at room temperature for 2 hours prior to development. The sample was developed in PGMEA with agitation for 4 hours. After development, the sample was rinsed with trichloroethylene (TCE) and isopropyl alcohol (IPA), followed by nitrogen blowing.

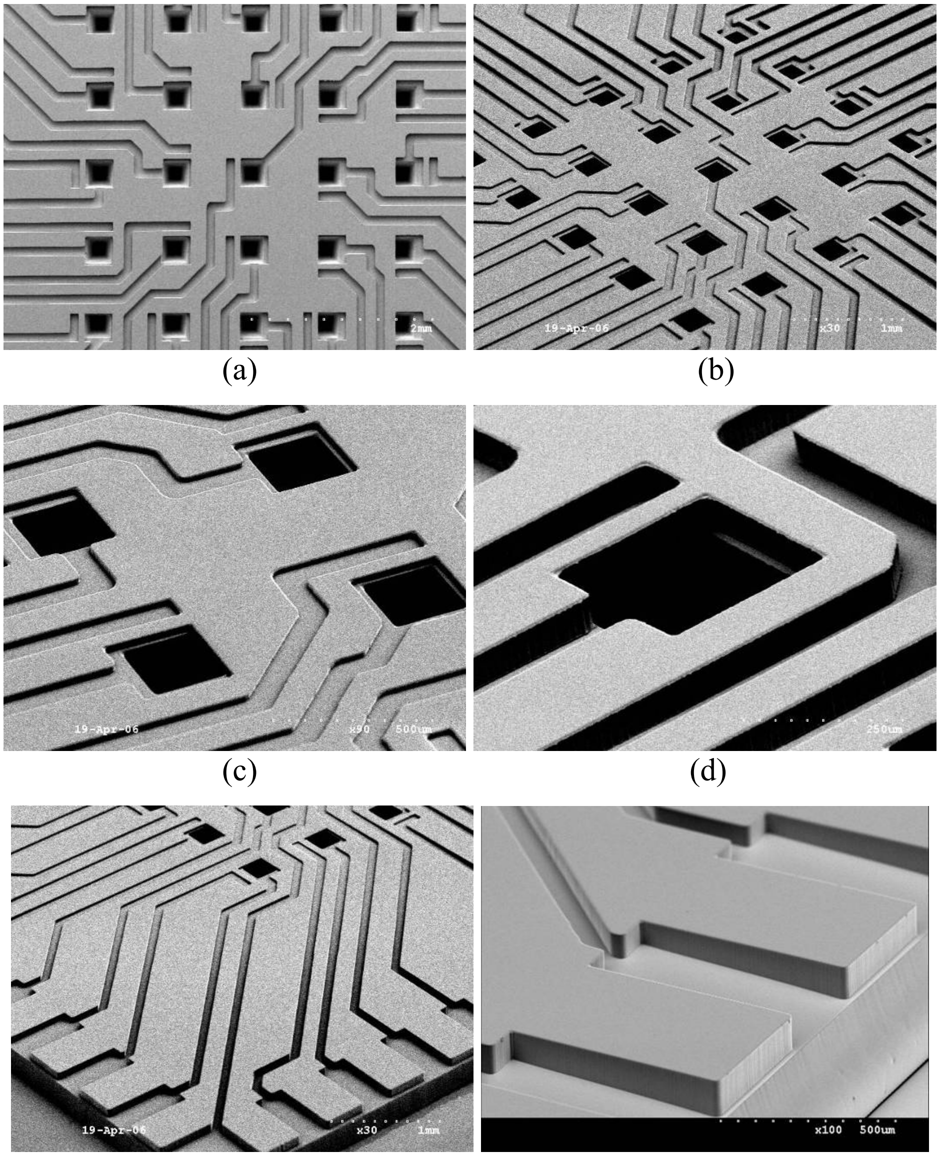

(a) (b)

(c) (d)

(e) (f)

Figure 3.22 Fabricated double-layer SU-8 mold for 3-D microelectrode array; (a) Top view of the mold, (b) oblique view of the mold, (c) region where 3-D microelectrodes will be formed, (d) close-up view of (c), (e) region where electrical contacts will be formed, (f) close-up view of (e)

The PDMS master was then copied from the SU-8 mold. PDMS prepolymer and curing agent were mixed in a 10:1 weight ratio, and the mixture was cast into the mold after degassing. Since the mold contained high-aspect-ratio tapered trenches, vacuum was applied to avoid air entrapment in the trenches. The PDMS master was separated from the mold after curing for 8 hours at 50°C in an oven. From the PDMS master, a PDMS mold was copied and metallized by E-beam evaporation. For metallization, 2000Å thick Au layer was deposited at a rate of 1.5Å/sec. To avoid crack formation during handling of the PDMS mold, the PDMS mold was firmly attached to a glass slide by polyimide tape before metallization. Once the metallization step was done, the 1st metal transfer step was performed. In principle, any material which has higher surface energy than PDMS can be placed on top of the PDMS mold for transferring metal pattern to the material, and the transferring process can be accelerated by applying heat. In thin work, adhesive tape was used for metal transfer processing. The results of the 1st metal transfer are shown in Figure 3.23.

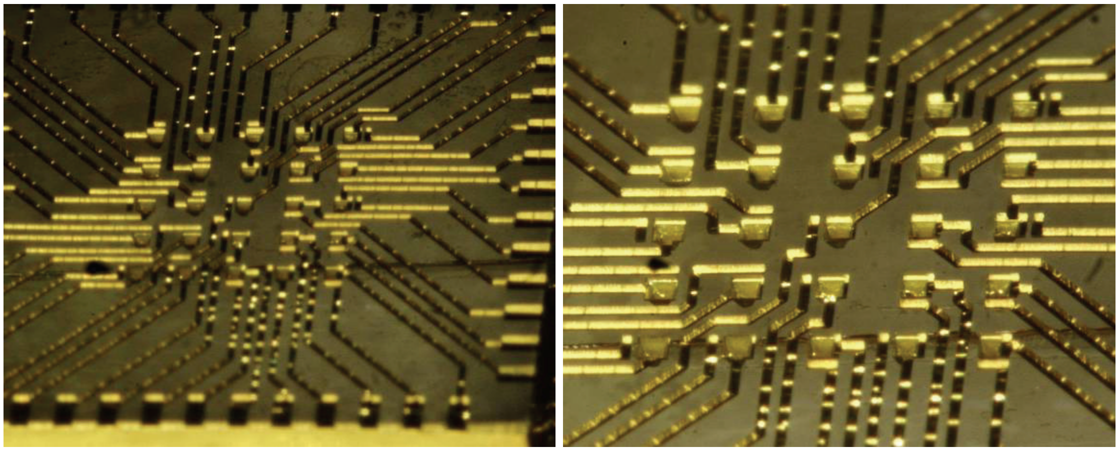

Figure 3.23 Optical micrographs of the PDMS mold after 1st metal transfer process

Due to the low surface energy of PDMS, it was possible to transfer metal from the PDMS mold to a variety of materials including SU-8, Polyurethane, and PMMA. To copy polymeric structures from the PDMS mold containing deep trenches, air bubbles must be removed. Vacuum can be used when the system has no solvent. For solvent systems such as SU-8 and solvent-cast PMMA, the solvent was evaporated slowly at mild temperatures (65°C for SU-8 and 30°C for PMMA) so that the entrapped bubbles could rise to the surface of the cast material and be released prior to surface hardening. After the bubbles were removed, the solvent was evaporated at an elevated temperature to accelerate the process (95°C for SU-8 and 50°C for PMMA). In two component systems such as Polyurethane and PDMS, the degassing process was successfully done under vacuum. The fabrication results are shown in Figure 3.24.

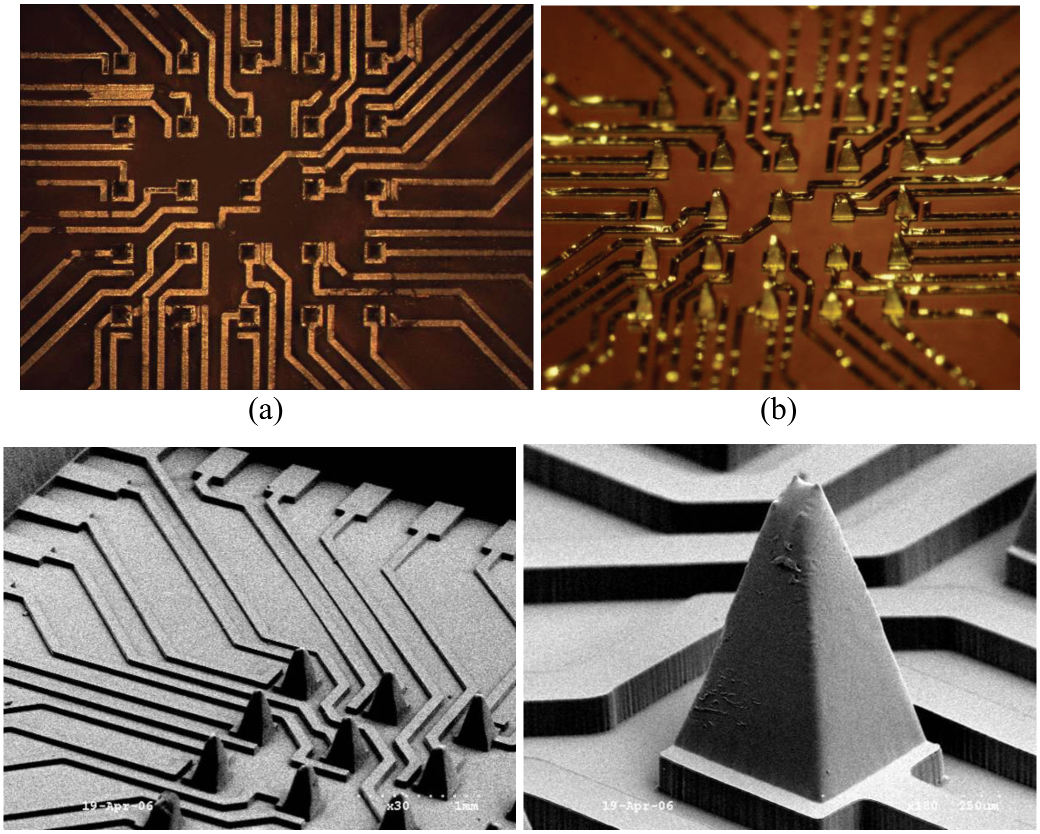

(a) (b)

(c) (d)

Figure 3.24 The fabricated 3-D electrically functional microstructure by metal transfer micromolding; (a) and (b) optical micrographs of the structure, (c) and (d) SEM pictures of the structure

3.3 Electrical Connection through Micro-via

3.3.1 Introduction

Wire bonding, which is a common method for packaging fabricated chips in the semiconductor industry, has been widely used to connect fabricated microdevices to outer electronics. For some applications, however, it is required to form large numbers of interconnects which can not be implemented by wire bonding due to the limited surface area for bonding pads. Also, it is sometimes desirable to form an electrical interconnect through the substrate for specific purposes. A potential solution is the formation of micro-vias through the substrate to implement electrical interconnects through the vias, a method widely used in the printed circuit board (PCB) industry. In this work, the formation of electrical interconnects through micro-vias by filling mirco-vias with conductive materials was investigated.

3.3.2 Electroplating through Micro-via

The first approach for implementing electrical connections through the substrate of a device was performed by filling vias with electrodeposited metal. As a test vehicle, a 500µm thick PMMA sheet was used for the substrate, and the detailed fabrication process is illustrated in Figure 3.25.

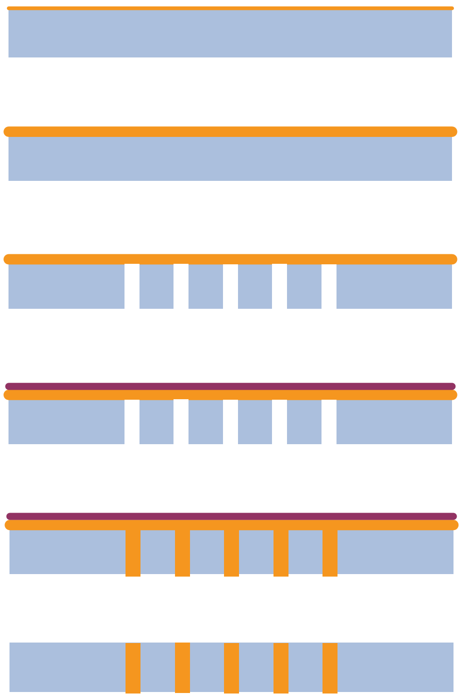

Figure 3.25 Schematic illustration of micro-via filling process by electroplating

One side of the PMMA sheet was coated with a Ti/Cu seed layer (300Å/3000Å), followed by electroplating a 10μm thick Cu layer on the seed layer (Figure 3.25a and b). Micro-vias were drilled by a CO_2 laser which thermally ablates polymeric materials. In principle, the CO_2 laser system does not provide sufficient energy to ablate the metal layer; therefore the deposited seed layer will play a role as an "etch stop" layer. However, it was observed that the thin seed layer was easily torn during the laser ablation; thus a thick electrodeposited Cu layer was formed prior to the process. Micro-vias of approximately 150μm in diameter were drilled with a CO_2 laser (Figure 3.25c), and the electroplated Cu layer was covered with polyimide tape before electroplating through the vias (Figure 3.25d). Cu was then electroplated through the vias with $10mA/cm^2$ current density (Figure 3.25e). Before electroplating Cu, the sample was soaked in water and vacuum was applied to degas the air bubbles entrapped in the vias. Since the exposed area of the seed layer for electroplating was small, it was hard to control current density. To resolve this issue, Cu tape was attached to the sample to increase the surface area for electroplating. After electrodeposition of Cu, the seed layer was selectively removed and the vertical interconnects were formed (Figure 3.25f). The fabrication results are shown in Figure 3.26.

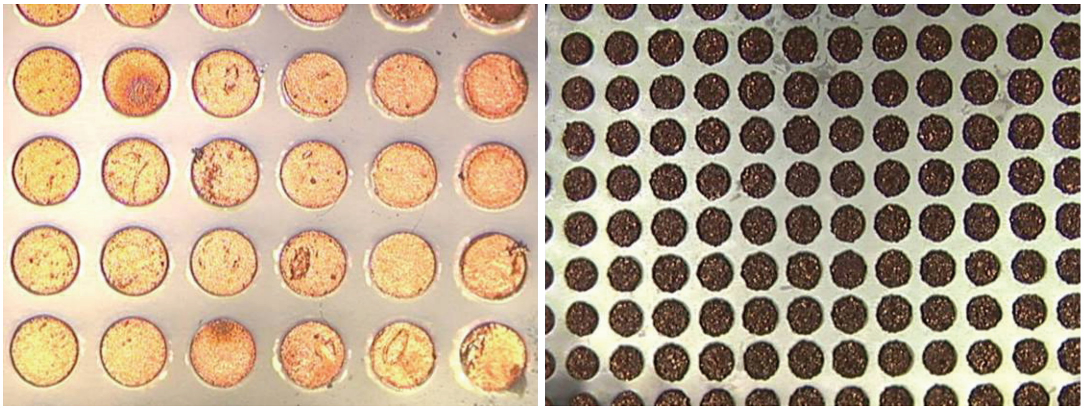
(a) (b)

Figure 3.26 Vertical interconnects fabricated by electroplating Cu in micro-vias; (a) picture taken from the top side where the seed layer was deposited and (b) picture taken from the bottom

3.3.3 Conductive Polymer Filling

The second approach to create vertical interconnects was to fill micro-vias with a conductive polymer. This approach is attractive in applications such as electroporation where extremely low resistance contacts are not required. In this work, commercially available conductive ink (Think & Tinker Ltd., Palmer Lake, CO, USA) normally used for coating the side walls of through-holes in PCB was utilized. The ink contained a mixture of silver and carbon in a polymer resin, and the viscosity was 125 cps. Conductive ink was spread over the surface of the substrate bearing pre-drilled micro-vias, and vacuum application caused the ink to fill the vias. The detailed fabrication process is depicted in Figure 3.27.

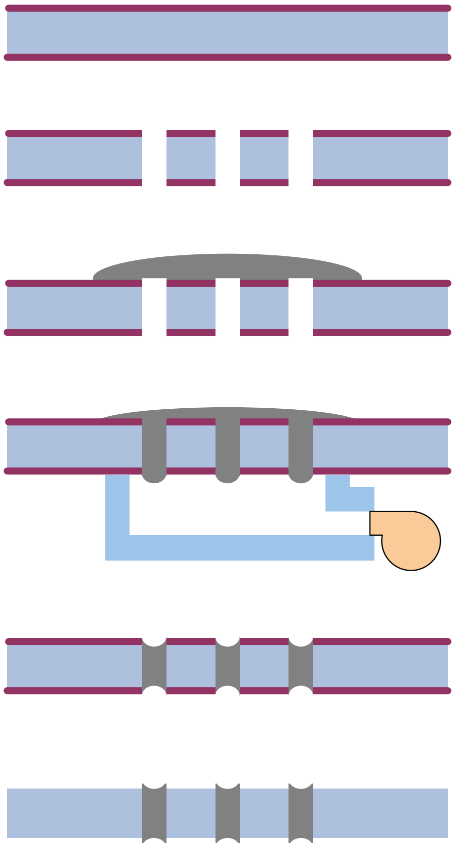

Figure 3.27 Schematic illustration of micro-via filling process

In this process, a 100µm thick polyimide sheet covered with 25µm thick Kapton tape was used as the substrate (Figure 3.27a). Micro-vias with a diameter of 20µm were drilled using the excimer laser system (Resonetics Inc., Nashua, NH, USA), and the surface of the sample was cleaned with isopropyl alcohol followed by nitrogen blowing (Figure 3.27b). Conductive ink was applied to the top of the sample (Figure 3.27c), and vacuum was applied from the backside of the sample to fill the micro-vias (Figure 3.27d), followed by a curing process in an oven at 100°C for 30 min. Excess material was removed by rubbing the sample with acetone (Figure 3.27e), and the Kapton tape was detached from the sample (Figure 3.27f).

It was observed that a dimple was formed during the removal of excess material; this is not desirable for a smooth electrical connection to external electronics. This problem was solved by attaching Kapton tape to both sides of the sample prior to the filling process, allowing protruded structures to remain on the surface of the sample after the removal of excess material and Kapton tape. The fabrication results are shown in Figure 3.28.

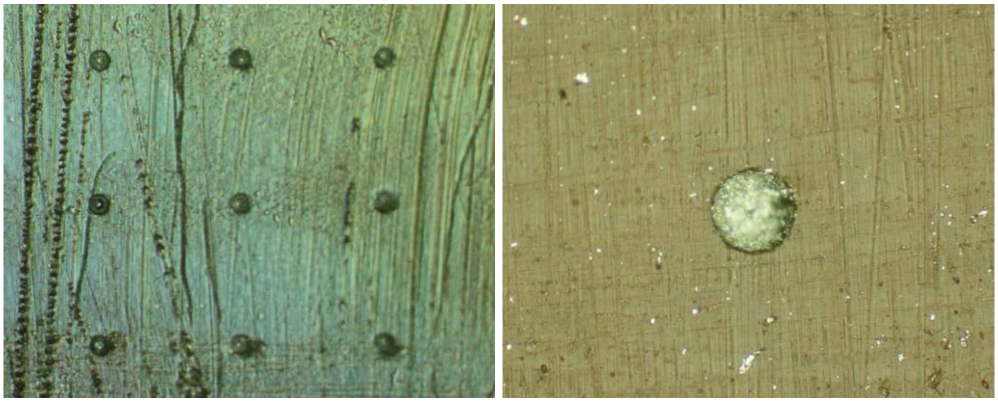

(a) (b)

Figure 3.28 Optical micrographs of micro-vias filled with conductive polymer; (a) 3 by 3 arrays of micro-vias with the diameter of 20μm, and (b) close-up view

CHAPTER 4

FABRICATION AND CHARACTERIZATION OF MICRONEEDLE ARRAY FOR ELECTROPORATION

4.1 Introduction

Based on fabrication techniques described in Chapter 3, two types of microneedle arrays for electroporation were fabricated: parallel-type and checkerboard-type microneedle arrays. These microneedle arrays differ in terms of the fabrication techniques used and the configuration of electric polarity. The parallel-type microneedle array was fabricated using a micromolding and laser ablation technique. The master structure of the parallel-type microneedle array was formed by RIE etching. Electrical isolation was realized by patterning a metal layer using an excimer laser. Alternate rows of the parallel-type microneedle array have the same electric polarity. To fabricate the checkerboard-type microneedle array, inclined/rotational UV lithography and metal transfer micromolding techniques were used. A rigid SU-8 mold for the microneedle array was formed using inclined/rotational UV lithography, and electrical functionality was implemented by a metal transfer micromolding technique. Alternate diagonals of the checkerboard-type microneedle array have the same electric polarity.

4.2 Parallel-type Microneedle Array

4.2.1 Fabrication

The fabrication process for our microneedle array consists of two main steps: 1) fabrication of a master structure, 2) fabrication of polymeric structure by micromolding.

The master structure was fabricated by reactive ion etching of an SU-8 tower array as reported by our group recently [126]. A 100 µm thick layer of SU-8 2025 (Microchem Corp., Newton, MA) was spun on a glass substrate bearing a clear field array of circular patterns, and baked for 30 min at 95°C on a hotplate. The SU-8 substrate was then formed by top exposure (800 mJ/cm^2), followed by post exposure baking (15 min at 95°C on a hotplate). Without developing the first SU-8 layer, the second layer of SU-8 (500 µm thick) was spun on the first layer, and baked for 20 hours at 95°C on a hotplate. The tapered SU-8 tower array was defined by exposing UV (5000 mJ/cm^2) from the backside of the glass substrate through a pre-patterned chromium layer. The sample was post-exposure baked (2 hours at 95°C on a hotplate), and developed in propylene glycol methyl ether acetate (PGMEA, Microchem Corp., Newton, MA). The tapered SU-8 structure was sharpened by reactive ion etching (700 Series Wafer/Batch Plasma Processing System, Plasma-Therm Inc., St. Petersburg, FL). A mixture of O_2 and CHF_3 gases (O2:100sccm, CHF3:10sccm) was used for etching SU-8 with 2µm/min etch rate under 1000 mTorr and 100W. Figures 4.1 and 4.2 show the fabrication process and the fabricated SU-8 master structure, respectively. The final structure contained a 16x16 array of microneedles with 7µm tip diameter, 70µm base diameter and 350µm height. Center-to-center distance between microneedles was 250µm.

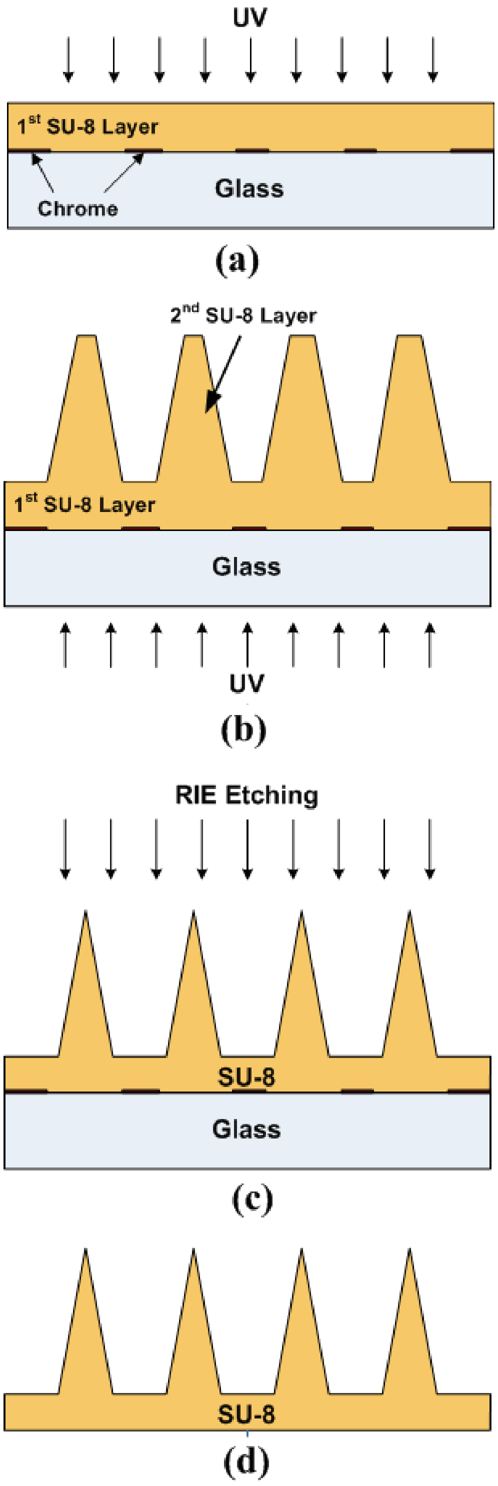

Figure 4.1 Fabrication process of the SU-8 master structure

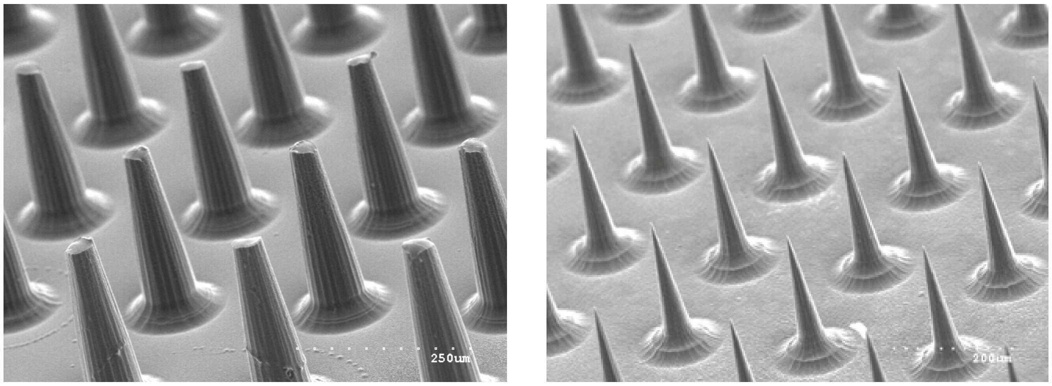

(a) (b)

Figure 4.2 SEM pictures of the fabricated SU-8 master structure; (a) structure in the middle of RIE etching, and (b) final structure

Once the SU-8 master was fabricated, a flexible polydimethysiloxane (PDMS) mold was copied from the master. The master was placed in a polystyrene (PS) container, and PDMS (Sylgard 184, Dow Corning Corp., MI) was poured into the container and cured at 50°C in a conventional oven for 10 hours. The PDMS mold was then separated from the master. Since a micromolding technique was adopted for fabricating the final device, many different materials [79] could be used as the microneedle substrate. Candidate materials lie at the intersection of moldability into high aspect ratio structures and biocompatibility. In this work, Polymethyl methacrylate (PMMA) was chosen because it satisfied both of these criteria. An additional advantage of the molding approach is its inherent mass-production capabilities, which are important for ultimate disposable applications. It is possible to reproduce the structure easily and quickly compared to a conventional photolithography process using SU-8.

In the micromolding of high aspect ratio structures, it is often difficult to utilize conventional thermoplastic melt-molding to form the structure from highly viscous polymer due to the potential for bubble entrapment in the deep and narrow mold. For our microneedle array, PMMA powder (M_W=75,000, Scientific Polymer Products Inc., Ontario, NY) was dissolved in ethyl lactate (Acros Organics, Morris Plains, NJ), which is a relatively low toxicity solvent compared to many other PMMA solvents, with 20% in weight. The solution was then cast into the PDMS mold and left at room temperature for 30min to allow the solution to spread over the entire mold. After that the sample was placed on a hotplate to evaporate solvent. Several different temperatures below the boiling point of the solvent were attempted, and it was observed that low temperature process under 50°C avoided bubble formation during evaporation. After evaporating the solvent on a hotplate at 50°C, the sample was annealed at 100°C in an oven for 1hour. Once the annealing process was completed, the sample was cooled down at room temperature, and the PMMA microneedle array was separated from the mold.

To realize electrical functionality, deposition of a metal seed layer (Ti/Cu, 300Å/3000Å) on the microneedle array was performed using a DC sputterer (CVC Products, Inc., Rochester, NY). Careful control of sputtering parameters was required to minimize heat generation during sputtering, which causes deformation of the structure. The seed layer was patterned by excimer laser ablation (Resonetics Inc., Nashua, NH) to isolate adjacent microneedle rows with a 100μm gap. Excimer lasers are used for micromachining polymers, but it was found that a thin metal layer can also be ablated by the same laser. The process parameters used in this work were as follows: 248nm wavelength, 200mJ energy, 25% power attenuation, 100μm/sec scribing speed. After isolation, a 20μm thick Ni layer was electrodeposited at room temperature with stirring to enhance structural rigidity. For an electrical connection between the microneedle array and external electroporation electronics, a backside contact is required so that there is no interference with insertion of the array into skin. To achieve this contact, a via was formed from the backside of the PMMA substrate using a CO_2 laser (LS500 Laser Engraving System, New Hermes-Gravograph, Inc., Duluth, GA). Copper wire was then inserted through the via and connected to the underside of the metallization using silver paste followed by an epoxy mechanical connection. Figure 4.3 shows the fabrication process and Figure 4.4 shows the fabricated device containing a 16x16 array of electrically active microneedles, with adjacent microneedle rows electrically isolated. The height of the microneedles is approximately 400μm, bottom diameter is 110μm, tip diameter is 15μm, and center-to-center distance between microneedles is 250μm.

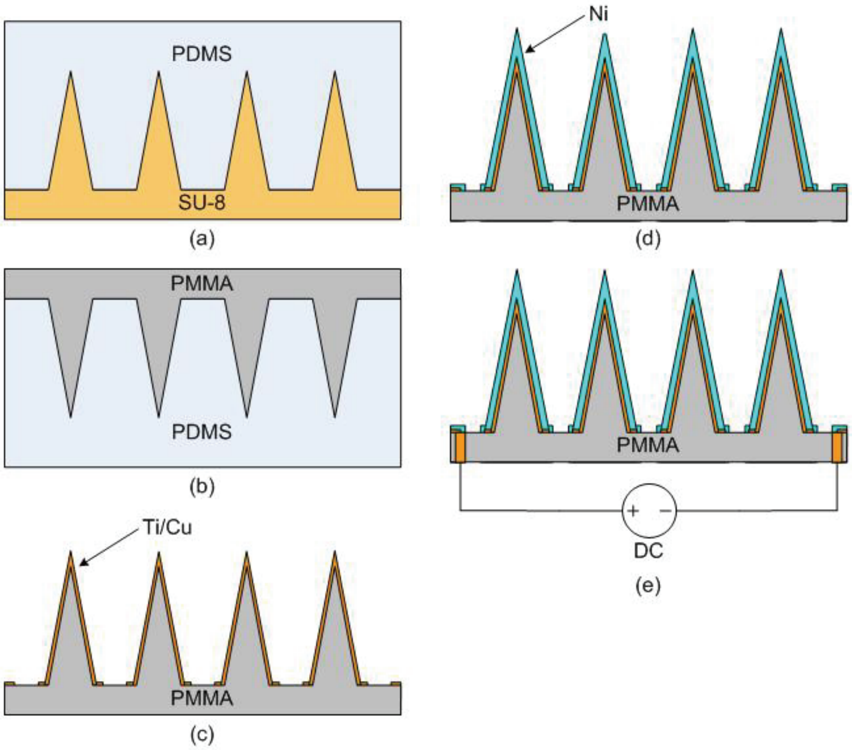

Figure 4.3 Fabrication process of the metal-patterned PMMA microneedle array

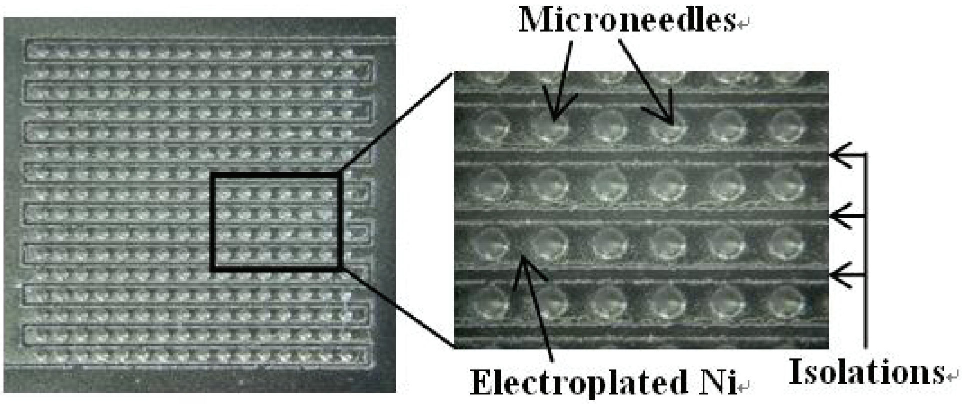

Figure 4.4 The fabricated electrically active microneedle array

4.2.2 Insertion Test

To examine the skin penetration ability of the microneedle array, several insertion tests were performed on human subjects using either non-coated (polymer-only) PMMA microneedles or nickel-coated PMMA microneedles of various nickel thicknesses. The microneedle array was placed on the hand of a human subject, and pushed using the thumb. After the test, the microneedle array was examined under the microscope. It was observed that the polymer-only microneedle array could not penetrate through human skin. The PMMA microneedle array was deformed during the penetration process shown in Figure 4.5. This seems to be contrary to the result of Moon et.al [90] who showed that a PMMA microneedle array could be successfully inserted into skin. The ability of skin penetration depends not only on the mechanical strength of a microneedle, but also on the geometry of the microneedle. Even though both works used the same material, there is a difference in the mechanical properties between the solvent-cast PMMA used in this work and the PMMA sheet used in Moon's work. The degree of crystallinity of the

PMMA sheet, which is commercially available and manufactured by an extrusion process, is greater than that of the solvent-cast PMMA, thus leading to higher mechanical strength. Compared to Moon's microneedle structure, the fabricated microneedle structure has a smaller base with a larger aspect ratio, indicating that this structure is inherently mechanically weaker than Moon's structure.

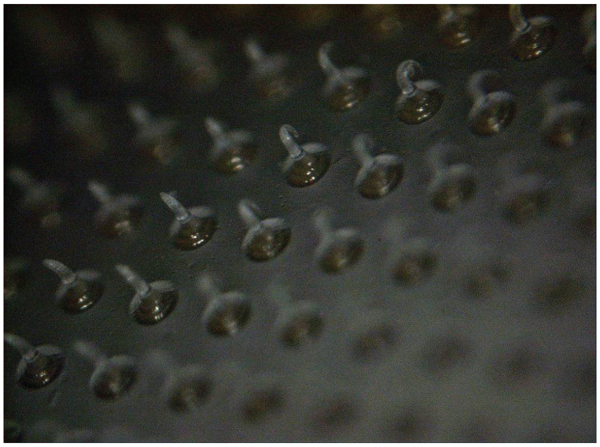

Figure 4.5 Optical micrograph of the PMMA microneedle array after insertion test

The rationale behind testing polymer-only microneedle arrays was to determine the metal layer thickness needed for implementing electrical functionality. If the polymer-only microneedle array demonstrated successful insertion into skin without damage, the electrical functionality could be realized by a thin metal layer, which would in turn reduce process time and cost. Since the experiment for insertion of a PMMA microneedle array failed, a thicker metallization is required. This was realized by electroplating a 10μm thick Ni layer on a PMMA microneedle array and testing the array on a human subject with same protocol as before. This test proved to be a success and is consistent with the previous studies [127]. However, it was observed that these needles were bent after several successive insertions. This might be due to accumulation of fatigue during the insertion/removal procedure. Usually a microneedle experiences not only axial force but also lateral forces, especially during removal. Therefore, multiple insertion tests could induce mechanical failures in the microneedles. To resolve this issue, thicker (20µm-thick Ni) coated arrays were tested. After the array was removed, the skin was stained with blue dye and then observed by microscopy. Figure 4.6 shows the stained skin in the pattern of the microneedle electrode array, indicating that the microneedle electrodes pierced the skin. Subsequent microscopic examination of the arrays showed that microneedle electrode tips were not damaged, even after multiple insertions, as shown in Figure 4.7.

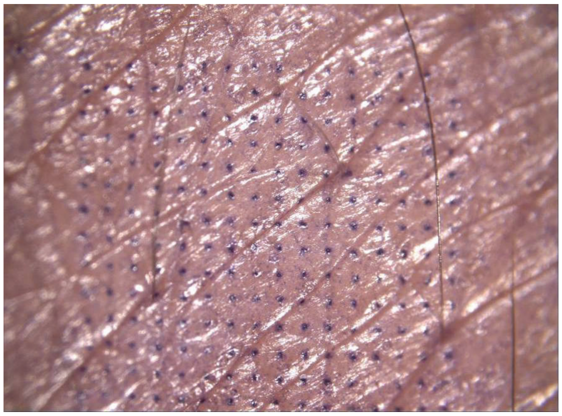

Figure 4.6 Photomicrograph of human skin *in vivo* after piercing with microneedle electrodes and staining with blue dye

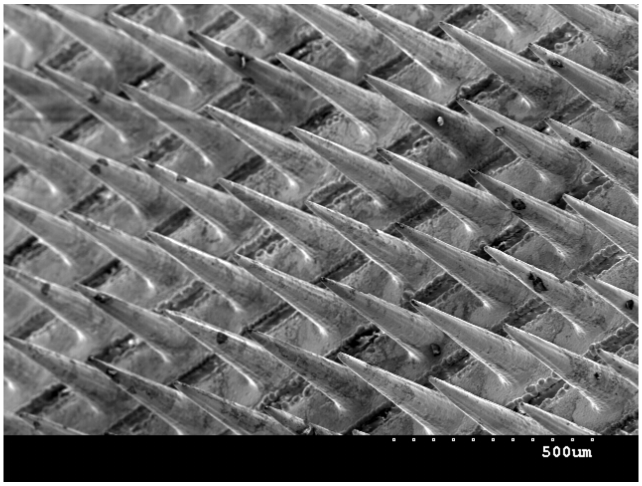

Figure 4.7 SEM picture of microneedle array after multiple insertion tests. Tissue debris is shown on the surface of intact microneedles

4.2.3 Electric Field Simulation

Since electroporation occurs when the cellular transmembrane potential induced by an external electric field exceeds a threshold value, it is desirable to generate a homogeneous electric field which can affect the cells uniformly, thereby maximizing the effect of electroporation. If the strength of the external electric field is too high, cell death can result. Therefore, electroporation should be performed within a specific range of electric field strength to achieve high uptake rate with high viability of cells. Since the electric field generated by the microneedle arrays is inhomogeneous, it is important to estimate how much volume in the microneedle array can be effective for electroporation and design the arrays and electroporation conditions to maximize this volume.

To analyze the spatial distribution of the electric field generated by the microneedle array, a 3-D finite element (FE) model was created using FEMLAB 3.1 (COMSOL, Inc., MA, USA). The 3-D FE model consists of a 4 by 4 sub-array of microneedles with the same geometry of the fabricated microneedle array, as shown in Figure 4.8.

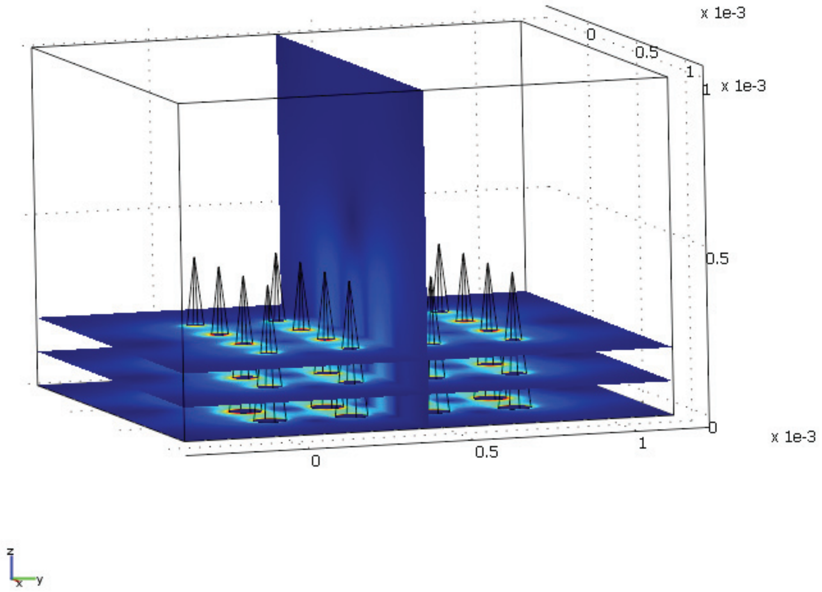

Figure 4.8 3-D finite element model for electric field simulation

The best way to investigate the distribution of the field strength over space is to generate homogeneous meshes, examine the field strength of each mesh, and count the number of meshes that correspond to the same field strength. However, it is not easy to generate homogeneous meshes especially when the geometry for simulation is complex. The other approach to extract the distribution of the field strength from inhomogeneous meshes is to calculate the area of meshes corresponding to the same field strength. This approach is statistically reasonable, but it requires heavy computation. In this work, another approach called the "grid approach" was attempted. Instead of counting the number of meshes with the same field strength, a grid was defined over the volume surrounded by four microneedles and the field strength at each intersecting point was examined. In principle, an infinitesimal grid is needed to accurately represent the entire area, but it was realized by several simulations that the overall shape of the distribution was not affected by the size of grid as long as the size of the grid is at least twice as small as that of the smallest mesh. After electric field simulation, data containing electric field strength at each grid point was exported to MATLAB to generate a histogram.

Using the grid approach with 10μm grid, a quarter of the volume surrounded by four microneedles located at the center of the model was analyzed. For analysis, electric field strength at each intersecting point was extracted from the model, and histogram was generated using MATLAB. Figure 4.9 shows a histogram of electric field strength when 6 V was applied between microneedles. The x axis represents electric field strength, and the y axis represents the number of grid points per electric field strength. The width of the bin for the histogram was 1 V/cm.

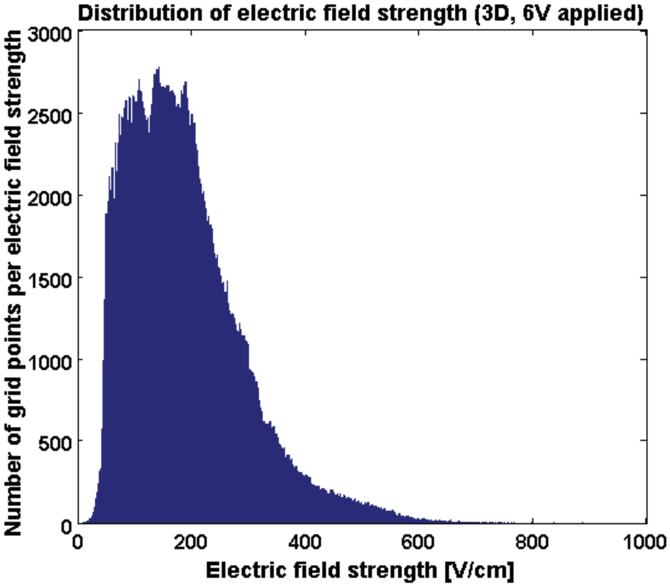

Figure 4.9 Distribution of the electric field strength when 6V was applied between the microneedle electrodes

Due to the geometry of the microneedle array, the electric field generated was inhomogeneous. The gap between microneedles varies linearly from 150μm at the bottom to 240μm at the tip. It was expected that the distribution of the electric field strength would be centered at the field strength given by the applied voltage divided by the average distance between microneedles. In this case, the electric field strength can be calculated as 300 V/cm. However, the peak of the distribution was shown near 200 V/cm. Also, a field strength higher than 400 V/cm, which corresponds to the field strength given by dividing the applied voltage by the shortest distance between the microneedle electrodes, was generated near the electrodes due to the concentration of the electric field.

The problem of 3-D modeling is that it requires heavy computation. Since the geometry contained high-aspect-ratio structures (i.e. microneedles), small meshes were needed to compute the electric field near the tips. Therefore, the total number of meshes required for the simulation exceeded more than 100,000 even with rough meshes. This implies that accurate 3-D modeling of high-aspect-ratio geometries is computationally burdensome, so it is desirable to simulate in 2-D if possible.

A series of 2-D finite element (FE) models that represent cross-section of the 3-D model at certain heights was created to approximate the 3-D model using FEMLAB 3.1. The limitation of this approach was that the distribution of electric field strength above the tips cannot be represented by the 2-D model. However, it was realized from the 3-D model that the contribution of the fringing field above the tips to electroporation could be neglected, enabling to use the 2-D models to estimate the electric field distribution at certain heights. To examine the effect of a fringing field near the tip of the microneedle array, an electric field in the volume between the tip and 50μm above the tip was analyzed from the 3-D model, as shown in Figure 4.10.

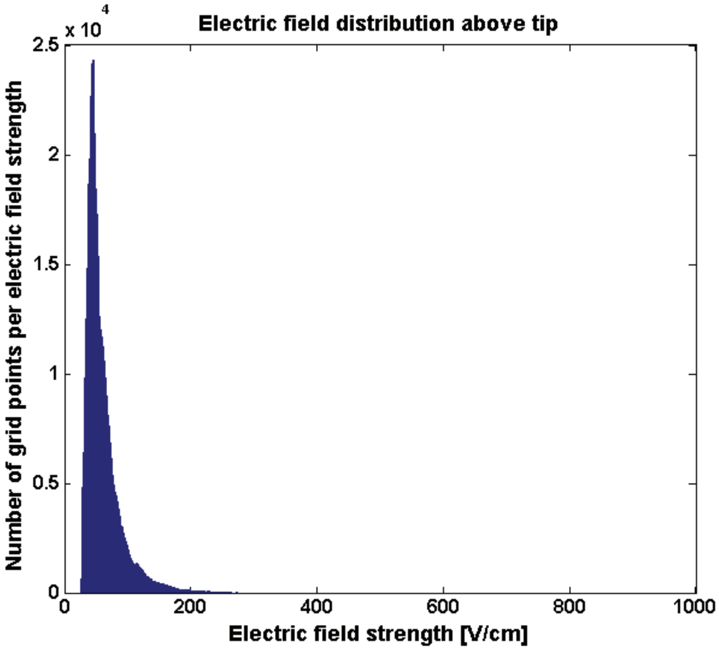

Figure 4.10 Distribution of the electric field strength above tips when 6V was applied between the microneedle electrodes

It was observed that the field strength due to the fringing field was mostly confined to a low field region compared to the field strength within the volume surrounded by the microneedle array. Also, the volume fraction occupied by relatively high electric field strength, which potentially contributes to electroporation, is small; suggesting that the contribution of the fringing field to electroporation should be negligible.

The 2-D model consisted of 16 circles, which represent the microneedle array at a certain height. The geometrical parameters as the microneedle array was maintained similar to the fabricated needles and the region surrounded by 4 circles located at the center of the model were analyzed. Figure 4.11a shows a model which mimics the bottom of the microneedle array. Regions with the same electric field strength are depicted by contours. Figure 4.11b shows the variation of the electrical field strength along the lines A and B, which are denoted in Figure 4.11a.

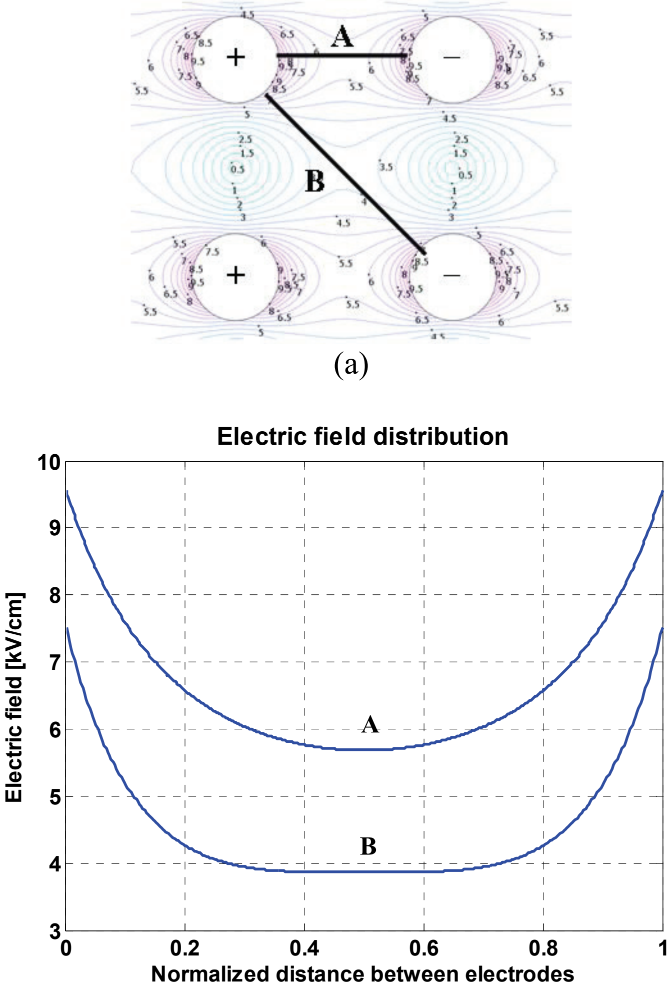

(a)

(b)

Figure 4.11 2-D finite element simulation results; (a) 2-D model also contains 4x4 electrodes, and only 2x2 electrodes at the center was used for the analysis. Geometric parameters are same as the 3-D model. For the analysis, 100 V was applied, and the electric field distribution along the two lines denoted as A and B was plotted, (b) Electric field distribution along line A (top) and B (bottom)

For line A, when 100 V was applied between the electrodes the maximum field strength was 9.5 kV/cm at the edge of the electrode and the minimum field strength was 5.7 kV/cm at the middle of the electrodes. For line B, the maximum and the minimum field strengths were 7.5 kV/cm and 3.9 kV/cm, respectively. Since the distance between the nearest electrodes in A is 150 μm, the field strength generated by the applied voltage of 100 V would be 6.67 kV/cm in the case of ideal parallel plates. However, a maximum field strength of 9.5 kV/cm was generated due to the field concentration on uneven surfaces. For further analysis, the average field strength between the 4 electrodes was calculated by integrating the electric field inside the electrodes numerically and dividing it by the area as follows:

$$E_{ave} = \frac{\iint E(x,y)dxdy}{Area} \tag{4.1}$$

where E(x,y) represents an electric field strength at the location (x,y).

The field strength at (x,y) was extracted from the simulation results, and the calculated average field strength was 4.37 kV/cm with a standard deviation σ = 1.595 kV/cm. Standard deviation was also calculated numerically by the following equation:

$$\sigma = \sqrt{\frac{\iint (E_{norm} - E_{ave})^2 dxdy}{Area}} \tag{4.2}$$

where $E_{norm} = \sqrt{E_x^2 + E_y^2}$ at (x,y).

Since the microneedle array generates an inhomogeneous electric field, it is important to know the degree of inhomogeneity of the field. For the case of the ideal parallel plate which generates a homogeneous electric field, the histogram of the field strength could be represented by the delta function and its field strength is simply found by dividing the applied voltage by the distance between two plates. For the microneedle case, the field strength varies spatially due to interaction between electrodes. This necessitates the use of a distribution function to represent field strength spatially. To estimate the distribution of the electric field strength generated by the microneedle array, a total of 10 2-D FE models, which mimic the cross section of the microneedle at a certain height from the microneedle substrate, were created. From the distribution of the electric field strength at a certain height given by the 2-D FE models, the 3-D distribution of the electric field strength was approximated by interpolation of the 2-D models. For simplicity, it was assumed that the distribution of the electric field strength between two slices was the same as that of the bottom slice. When the number of the 2-D models is too small (i.e. 3 slices), the error due to interpolation is significant. However, this error can be reduced by increasing the number of 2-D models. Also, the overall distribution constructed from the 2-D models will underestimate the relatively lower field region where the field strength is lower than the mean value of the distribution and overestimate the relatively higher field region. The extremes of the simulation were the cross sections of the bottom of the microneedle array (1st Model) and of the tip of the microneedle array (10th Model). For each simulation, 6 V was applied between electrodes, and a quarter of the area (due to geometrical symmetry) surrounded by the 4 electrodes was used for the analysis. The analysis was performed using the grid approach described previously. For each simulation, the smallest mesh size was controlled to be approximately 1 μm, and the size of grid was fixed to be 0.5 μm. The simulation was performed by FEMLAB 3.1, and the extracted data was processed by MATLAB 7.2 (The MathWorks, Inc., MA, USA). A histogram was used to express the distribution of the field strength, and some of the results are shown in Figure 4.12. The x axis represents electric field strength (V/cm), and the y axis represents the number of points per electric field strength defined by the grid.

Figure 4.12a shows the electric field distribution at the bottom of the microneedle array, and two peaks with an exponential decay around the peaks can be seen. These two peaks indicate that the field distribution is mainly determined by interaction of the nearest two electrodes, and an exponentially decaying tail is due to a fringing field generated by the uneven shape of the electrode. Figure 4.12b,c, and d show the field distribution at different heights, and two peaks move toward lower field region since the gap between electrodes increases along the height of the microneedle due to its tapered geometry. It is noticeable that even though overall field strength decreases along the height, the tail in the high field region becomes longer due to the electric field concentration on small features.

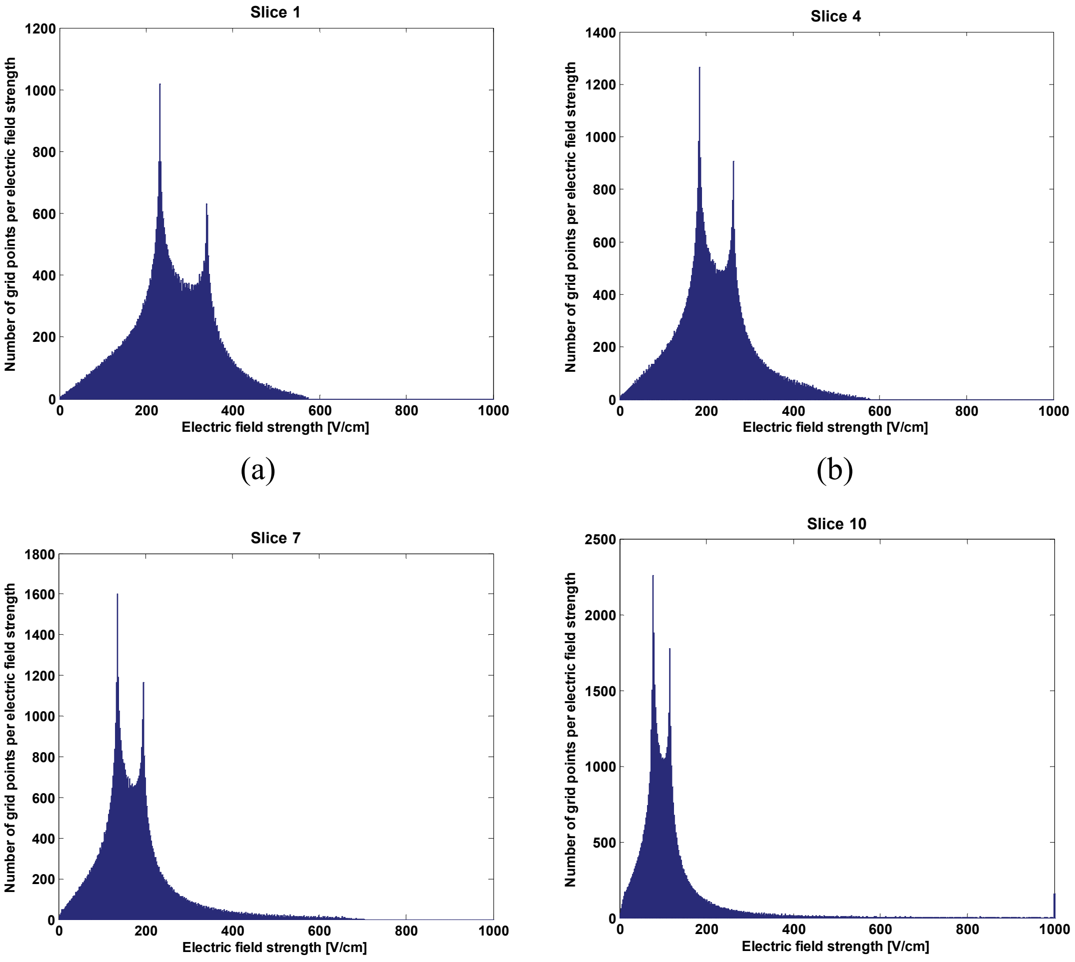

(a) (b)

(c) (d)

Figure 4.12 Distribution of the electric field strength at different heights; (a) at the bottom of the microneedle array, (b),(c) in the middle of the microneedle array, and (d) at the tip of the microneedle array

To estimate the overall field distribution within the volume surrounded by the microneedle array from the 2-D simulation results, the electric field distribution in the volume between 2 slices was assumed to be same as the distribution of the bottom slice. The total distribution of the electric field strength was estimated by adding each distribution, and the distribution was divided by the total number of grid points. Figure 4.13 shows the result of the estimation of the distribution of electric field strengths.

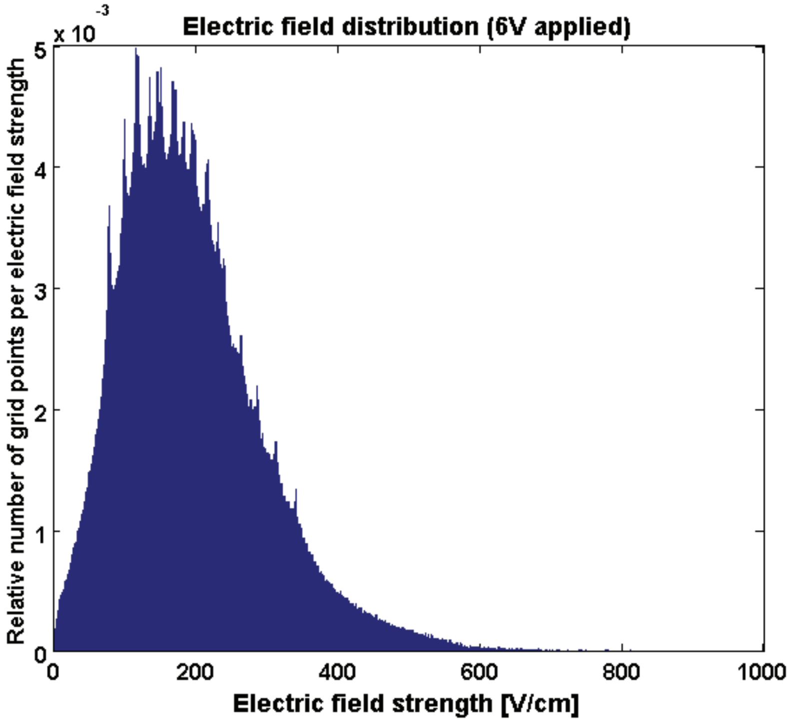

Figure 4.13 The distribution of electric field strength when 6V was applied

To derive an analytical expression of the distribution from the simulation result, curve fitting was performed by MATLAB. For curve fitting, several combinations of general functions such as polynomial, exponential, and Gaussian were tested. The distribution was best fitted using a combination of two Gaussian functions. Since the purpose of the simulation was to derive a general expression of the distribution to predict how much percent of the total volume could contribute to electroporation, normalization of the distribution was performed. We assumed that the distribution can be expressed by a function f(x), and the distribution after normalization is f(x'). The function f(x) is the probability density function, and the area under the probability density function between any two points, x_1 and x_2, represents the probability that a randomly chosen variable value will lie between these two values. In our case, the random variable is the electric field strength, and the area under the probability density function corresponds to the volume fraction corresponding to this field strength. If the relationship between x and x' is x' = x/k where k is normalization constant, then f(x') = kf(x). The proof of this relationship is given below:

$$x' = x/k \text{ and } \int f(x')dx' = \int f(x)dx = const$$

since $dx' = dx/k$,

$$\int f(x')dx' = \int \frac{f(x')}{k}dx = \int f(x)dx = const$$

$$\therefore f(x') = k \cdot f(x) \tag{4.3}$$

For normalization, the nominal field strength, which is given by the applied voltage divided by the nearest distance between two electrodes at the bottom of the microneedle array (150 μm for the fabricated device), was chosen as normalization constant *k*. For example, if 6 V was applied between electrodes, the nominal field strength would be 400 V/cm (6 V divided by 150 μm). Figure 4.14a shows two distributions of electric field strength generated by two applied voltages of 3 and 6 V, and Figure 4.14b shows the distribution after normalization. The analytical expression of the fitted curve was given by two Gaussian functions with the coefficient of determination R^2=0.9998 as follows:

$$f = 1.303e^{-((x-0.4051)/0.2241)^2} + 0.6986e^{-((x-0.6033)/0.3873)^2} \tag{4.4}$$

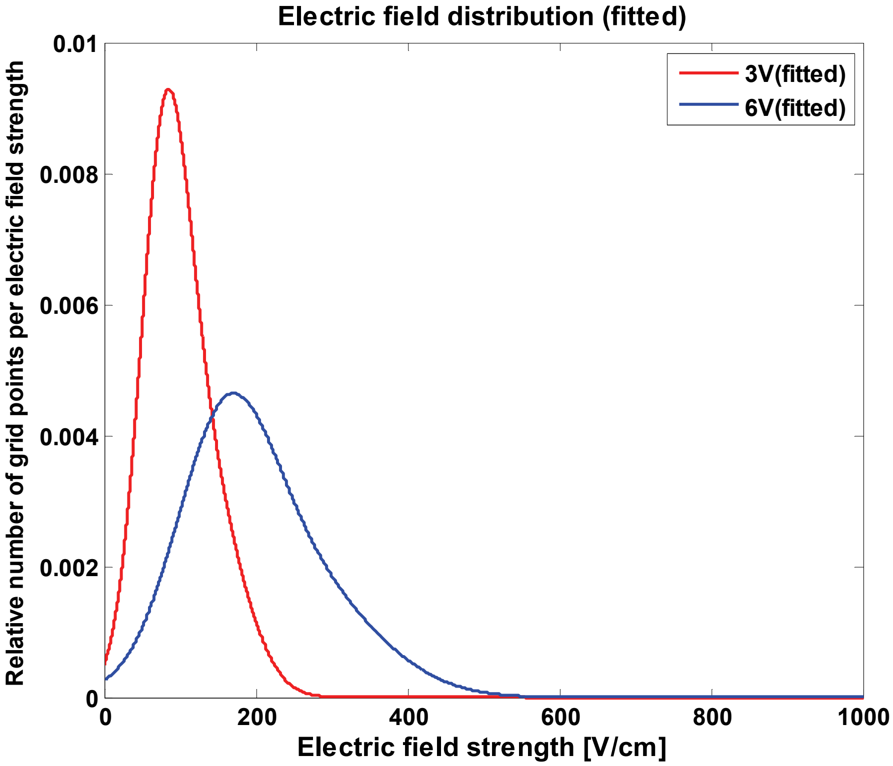

(a)

Figure 4.14 The distribution of electric field strength; (a) before normalization and (b) after normalization

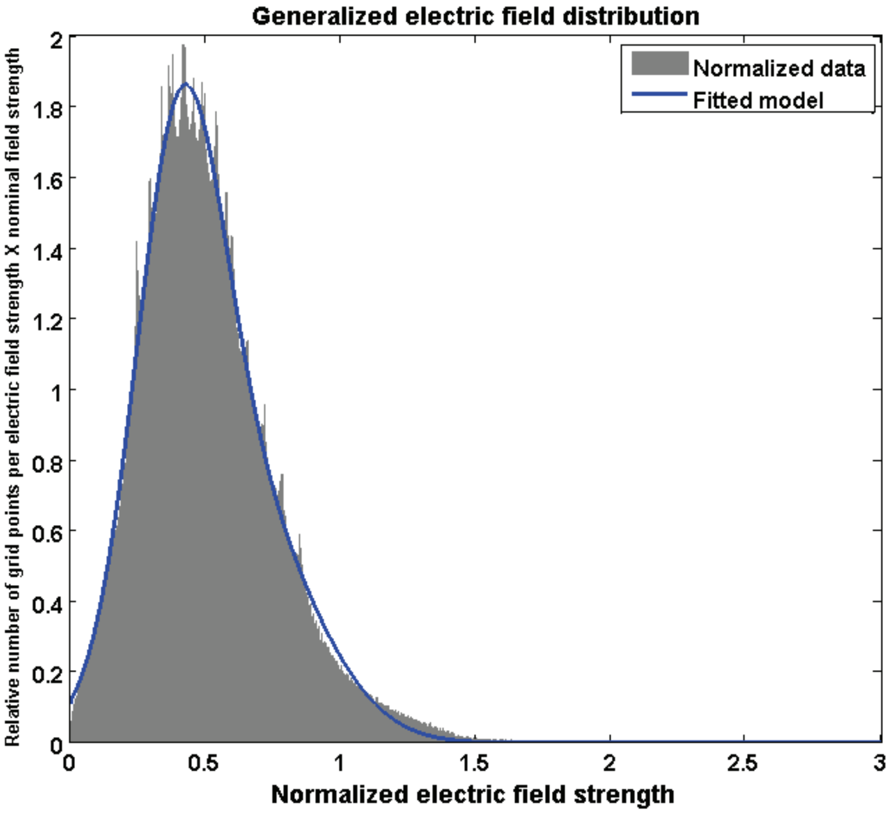

(b)

Figure 4.14 continued

Since the electric field distribution was modeled analytically, it is possible to determine the optimal field strength required for electroporation. For example, if we know the lower bound (cell membrane permeabilization) and the upper bound (cell death) for effective electroporation, the applied voltage required for generating the field strength that can maximize the effect of electroporation can be estimated from the model. Suppose that the target cell is DU 145 whose diameter is approximately 20μm. According to Schwann's equation (Eq. 2.1), the threshold electric field strength is 166 V/cm (0.5 V of transmembrane potential is used for calculation [128]). From the literature [129], approximately 90 % viability was achieved when a field strength of 500 V/cm with 2.8 msec pulse length was applied to DU 145 for calcein delivery. By defining a “window” with these bounds, it is possible to predict a volume fraction which contributes to effective electroporation at different voltages applied for experiments. For example, if voltages that induce the nominal field strength of 250 V/cm, 500 V/cm, 750 V/cm, and 1 kV/cm were applied, the volume fraction which contributes to the delivery of molecules can be calculated from the model as 22 %, 72 %, 68 %, and 49 %, respectively. The volume fraction that exceeds the assumed upper bound for each condition can be given as 0 %, 3.6 %, 22.4 %, and 46 %, respectively. From these results, it can be expected that a field strength of 500 V/cm would be the best condition among the 4 different conditions.

4.3 Checkerboard-type Microneedle Array

4.3.1 Fabrication

To fabricate the microneedle array for electroporation, the double-layer micromold approach combined with metal transfer micromolding, which was discussed in chapter 3, was adopted. As described before, a rigid mold for the microneedle array was fabricated by inclined lithography and a protrusion structure for electrical isolation was formed successively (Figure 4.15a). From the SU-8 rigid mold, either a flexible or a rigid master structure was copied (Figure 4.15b). For the fabrication of a flexible master, PDMS (Sylgard 184, Dow Corning, Midland, MI) was cast into the rigid mold and separated from the mold after curing. To enhance the wettability of PDMS on the surface of the mold, a thin Au layer (1000Å) was deposited (EFFA Sputter Coater, Ernest F. Fullam, Inc., Clifton Park, NY) onto the mold prior to PDMS casting. For the fabrication of a rigid master, a Ti/Cu layer (300Å/5000Å) was deposited (DC sputterer, CVC Products, Inc., Rochester, NY) into the SU-8 mold as a seed layer and Ni was electroplated into the mold. Before electroplating Ni, the sample was degassed in water. Once a 300μm thick layer of Ni was electroplated at a deposition rate of 15μm/hour, the sample was washed with DI water and immersed in copper etchant for Cu etching. By etching the Cu layer, the electroplated Ni master structure was separated from the SU-8 mold. A PDMS mold was then copied from the master and metallized with Au/Ti (2000Å/500Å), followed by the removal of the metal layer on the protrusion (Figure 4.15c and d) by bringing it in contact with adhesive tape (Scotch Magic Tape 810, 3M Corp., St. Paul, MN). The remaining metal in the PDMS mold was then transferred to the cast materials such as PMMA (M_W=75,000, Scientific Polymer Products Inc., Ontario, NY), polyurehtane (PU) (Smooth-Cast 310, Smooth-On, Easton, PA), polylactic acid (PLA) (L-PLA, 1.1 dL/g, BPI, Birmingham, AL), and epoxy resin (SL. 7510, 3D Systems, Valencia, CA) during the separation process (Figure 4.15e). The transferred metal layer was then used as a seed layer for electroplating. Even though the transferred metal layer could be sufficient for implementing the electrical functionality on the final electroporation needle structure, the main purpose of strengthening the metal layer by electroplating is to provide structural rigidity to the microneedles for easy and safe insertion into skin. Also, a sufficiently thick metal layer can be used as an "etch stop" for drilling holes from the backside of the sample by laser machining. A Ni layer with a thickness of 15-20μm was electrodeposited on the seed layer (Figure 4.15f), followed by drilling holes from the backside of the sample by a CO_2 laser for electrical interconnects (Figure 4.15g). Thin copper wires were then inserted into the holes to construct electrical pathways to the outer electronics, and the holes were filled with conductive polymer (Figure 4.15h).

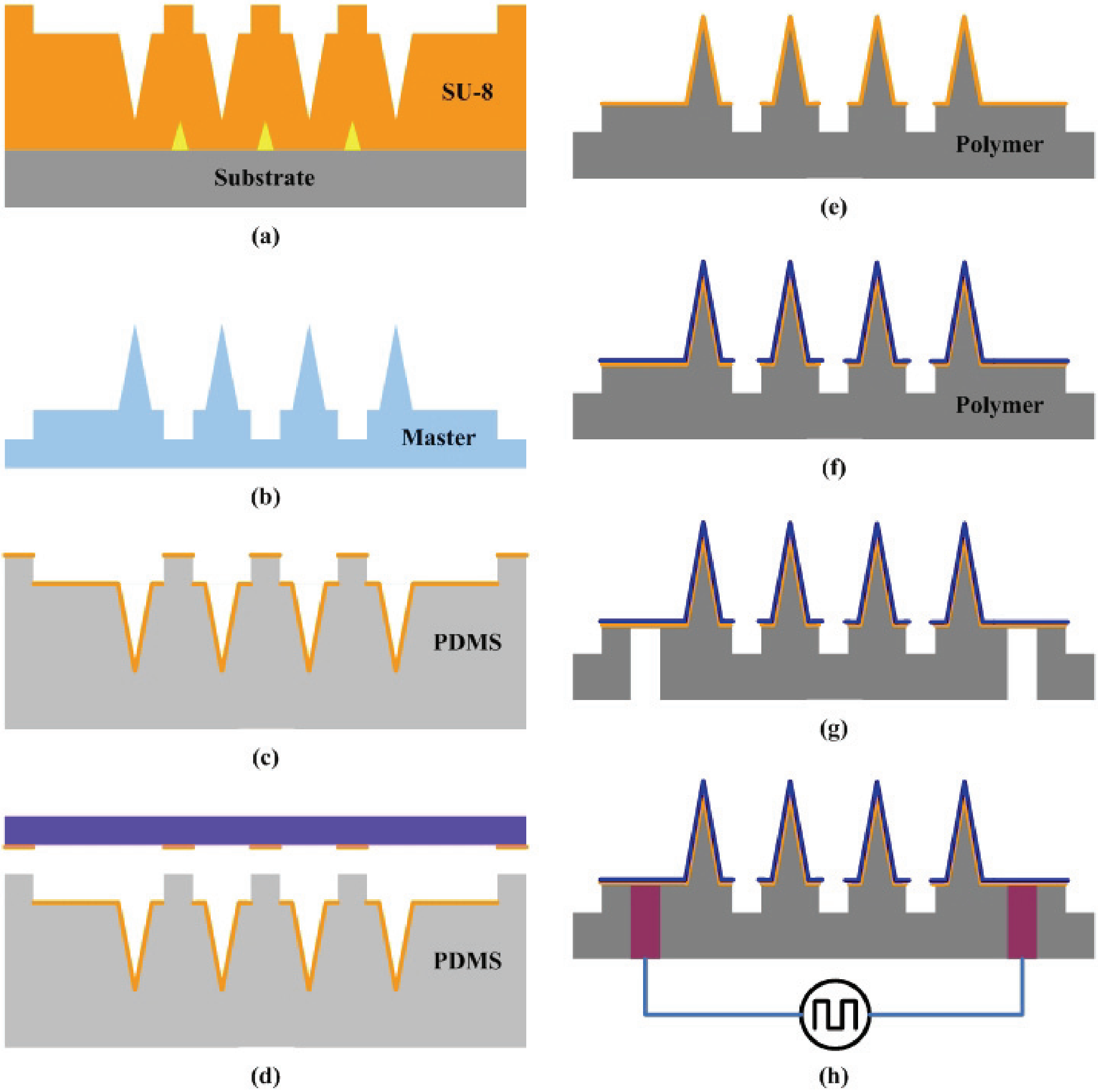

Figure 4.15 Schematic illustration of the fabrication process for an electrically active microneedle for electroporation

For the fabrication of the rigid SU-8 mold, approximately 800μm thick SU-8 2025 was deposited on a silicon substrate, followed by a soft-baking process at 95°C on a hot plate for 30 hours. The negative of the microneedle array was then formed by the inclined/rotational UV lithography discussed in Chapter 3, followed by post-exposure baking (PEB) at 95°C on a hot plate for 30 min. During the PEB, the epoxy exposed to UV changed to a dark yellow hue. Since there was a difference in color between the exposed and the unexposed areas, it was possible to align and pattern the second SU-8 layer without developing the first SU-8 layer. The second SU-8 layer was spun on the first SU-8 layer, baked, exposed, and developed in PGMEA along with the first layer after PEB. For an 80μm thick SU-8 layer, SU-8 2025 was spun on the first SU-8 layer at 1000 rpm for 40 sec, and baked in an oven at 95°C for 30 min. An exposure dose of 400 mJ/cm^2 was applied under a 365nm wavelength UV lamp. PEB was done in an oven at 95°C for 15 min. The fabrication results are shown in Figure 4.16.

The fabricated SU-8 mold consists of 10 by 10 tapered square wells. The size of the squares was 200μm x 200μm, and the gap between each square was also 200μm. The protrusion structure was designed to isolate adjacent wells; thereby, the electric polarity of each adjacent electrode pairs was opposite in the final device.

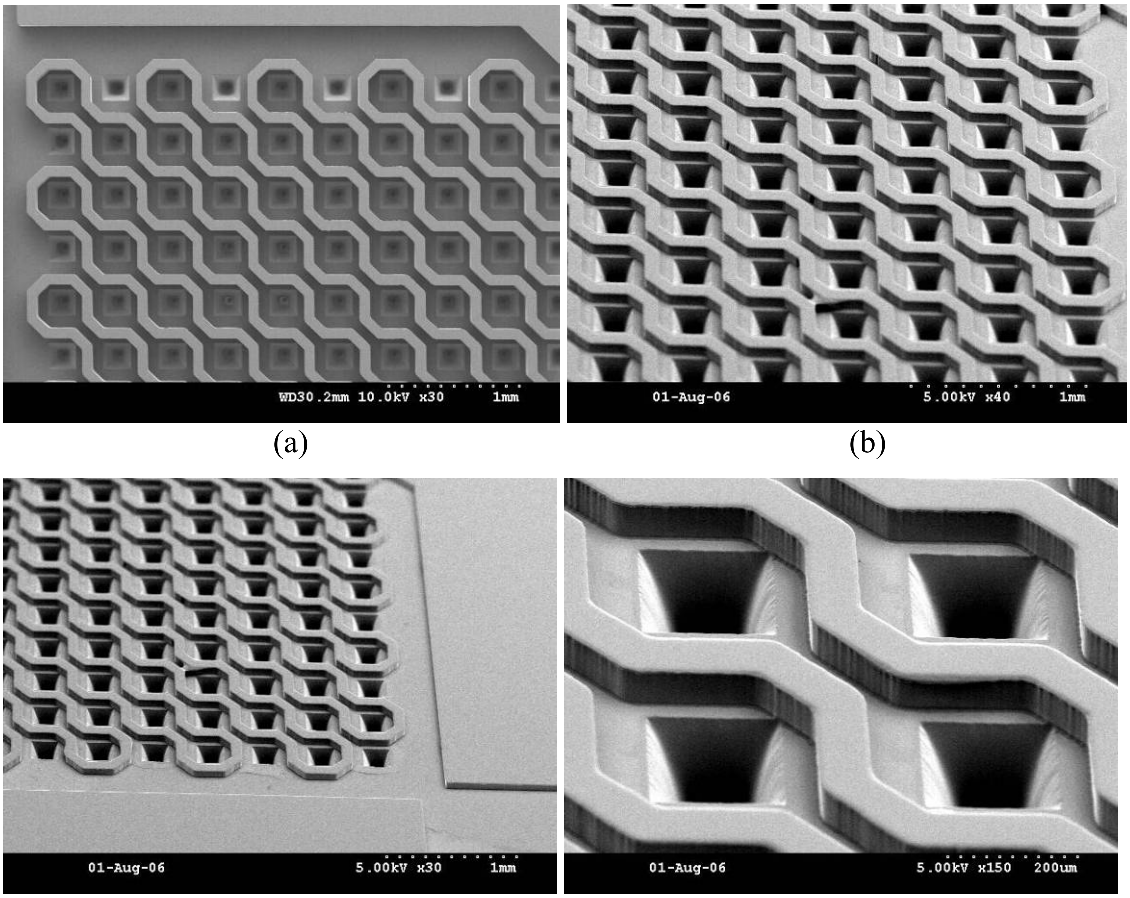

(a) (b)

(c) (d)

Figure 4.16 Fabricated double-layer SU-8 mold; (a) Top view, (b) Oblique view of the center of the mold, (c) Oblique view showing area where micro-via will be formed, (d) Close-up view of the mold

For easy and stable removal of the metal on top of the protrusion of the PDMS mold, a thick protrusion structure is preferable because the PDMS mold is deformed during the 1st metal transfer process. To minimize the possibility of the removal of metal on a region where metal should reside, a thicker 2nd SU-8 layer was prepared and was spun cast. This resulted in a 250μm thick protrusive structure. The fabrication results are shown in Figure 4.17.

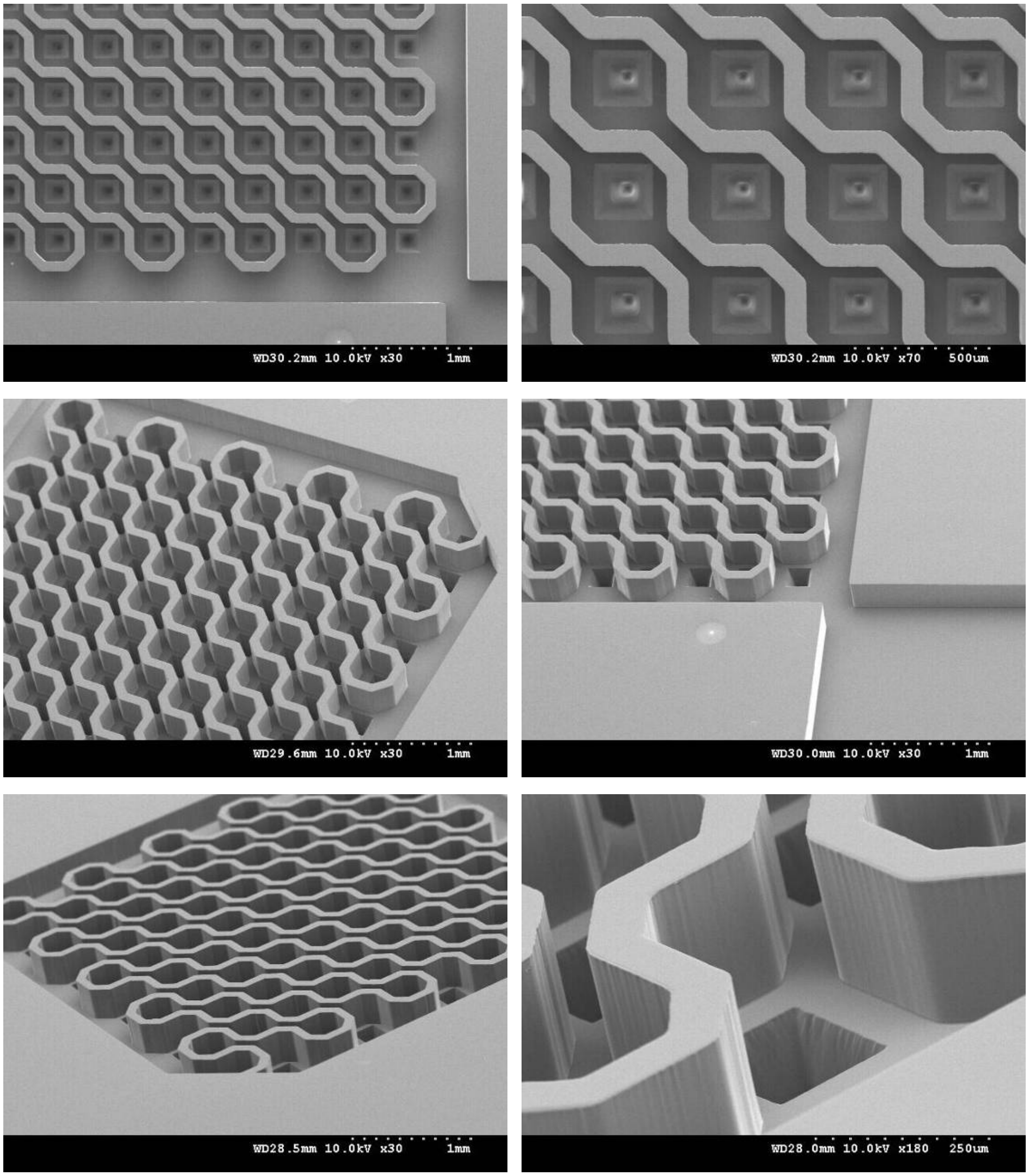

Figure 4.17 Fabricated SU-8 mold with 250μm thick 2nd layer for electrical isolation

From the SU-8 mold, a master structure was subsequently fabricated either by PDMS casting or Ni electroplating as described earlier. To fabricate a Ni master, a Ti/Cu seed layer (500Å/5000Å) was deposited into the SU-8 mold using a CVC DC sputterer (CVC products, Inc., Rochester, NY), and Ni was electroplated with a deposition rate of

15μm/hour. After a 20 hour electrodeposition of Ni, the SU-8 mold was soaked in copper etchant to etch the Cu seed layer. Etching the Cu seed layer served as a release for the electroplated Ni master from the SU-8 mold. The fabricated Ni master structure is shown in Figure 4.18.

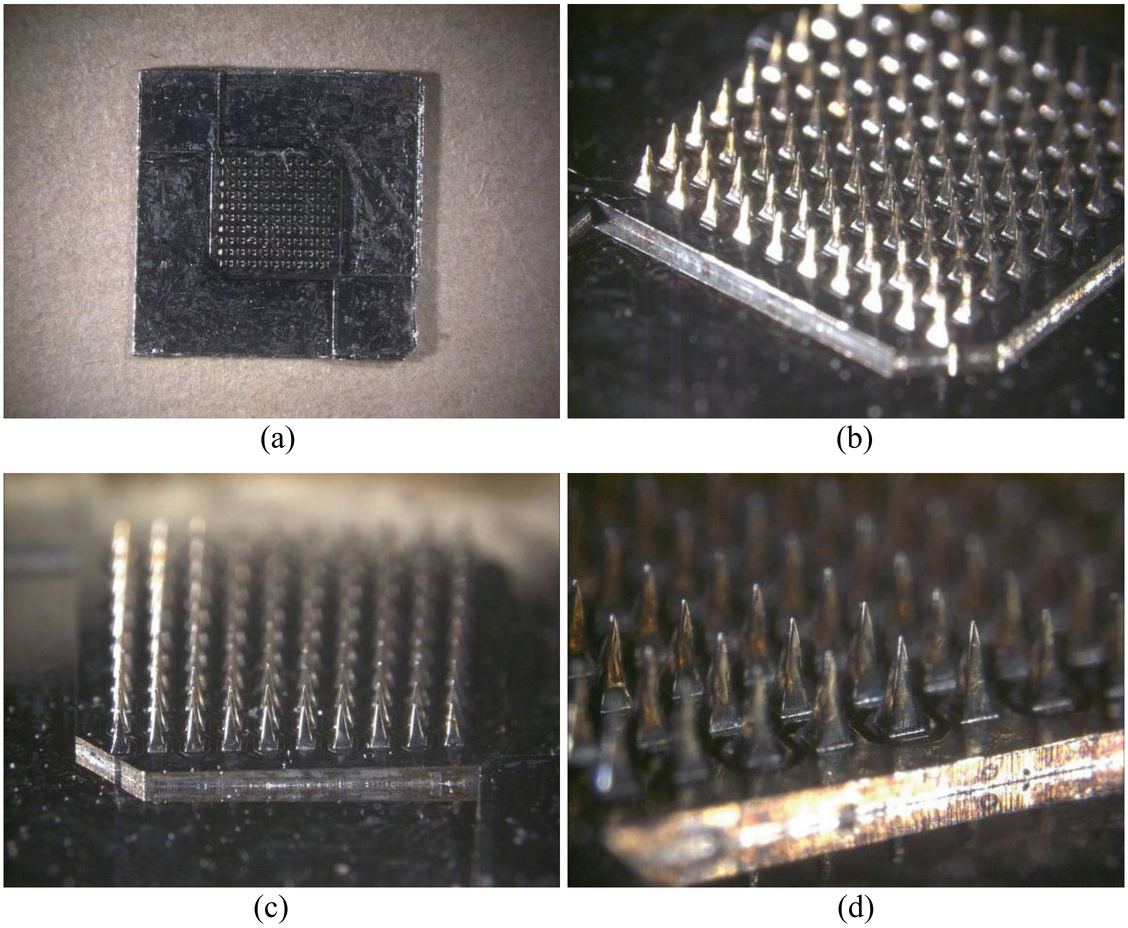

Figure 4.18 Fabricated Ni master structure; (a) overall view from the top, (b) oblique view, (c) side view, and (d) close-up view of (c)

The fabricated master was then placed in a PS container, and PDMS was poured into the container to fabricate a PDMS mold. The detailed fabrication steps were described in Chapter 3. Once the PDMS mold was prepared, the mold was metallized using an e-beam evaporator. Since PDMS expands during the metal deposition process due to temperature elevation inside the chamber, micro-cracks were found along the structures. To minimize the formation of these micro-cracks, the PDMS mold was slowly cooled down inside the chamber after the deposition of metals for 15 min, and the chamber was vented afterward. The metallized PDMS mold is shown in Figure 4.19.

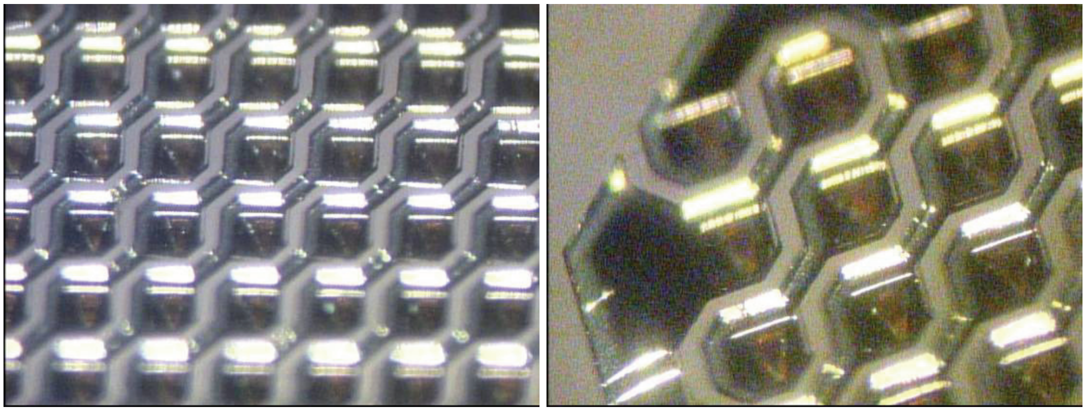
(a) (b)

Figure 4.19 Optical micrographs of the metallized PDMS mold; (a) center of the mold, (b) close-up view

After the metallization of the PDMS mold with Ti/Au (500Å/2000Å), an adhesive tape was gently placed on the mold to remove the metal layer on the protrusion. After the removal of the metal layer, the sample was examined under a microscope. Until the metal layer on the protrusion was completely removed, this process was repeated. It was realized that if too much pressure was applied during the removal process, micro-cracks were generated due to the flexibility of the PDMS mold. Figure 4.20 shows the PDMS mold after the removal of the metal layer on the protrusion.

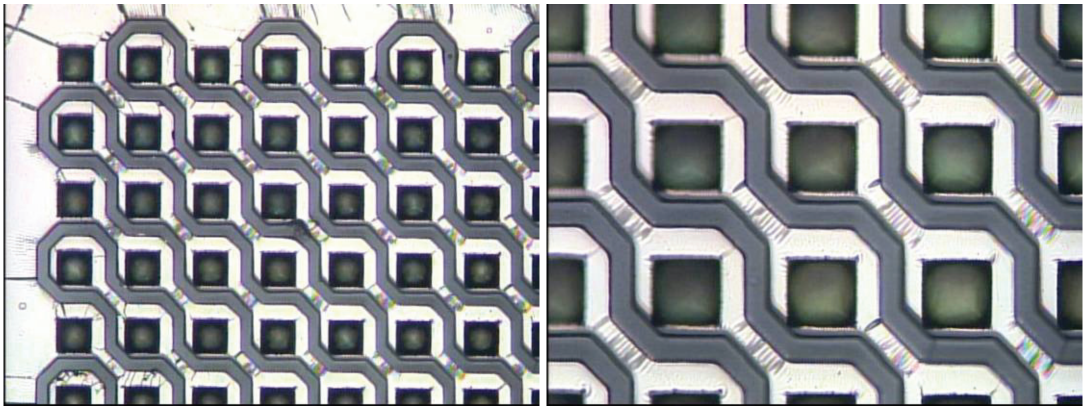
(a) (b)

Figure 4.20 The PDMS mold after the removal of the metal layer on the protrusion. White region represents Ti layer, and gray region represents PDMS; (a) micro-cracks were shown around the structure, and (b) close-up view of the mold

After the selective removal of the metal layer from the PDMS mold, the target polymer was cast into the mold. For PLA casting, PLA pellets were stacked in the mold and melted in a vacuum oven (1415M, VWR, West Chester, PA) at 190°C for 2 hours. Since the mold contains high-aspect-ratio tapered well structures, the application of a vacuum was necessary to fill the mold with PLA. Degassing was performed at 25 torr for 30 sec, and the pressure inside the oven was then brought back to atmospheric pressure. This process was repeated 3 times. The sample was then further melted for 1 hour and degassed again to remove any remaining bubbles on the surface of the sample. After degassing, the sample was cooled down at room temperature for 2 hours and the molded PLA was separated from the PDMS mold. In addition to PLA, other polymers such as PU and epoxy resin were used as casting materials. For the PU process, a pre-polymer and the corresponding curing agent were mixed in a 1:1 ratio before casting into the mold. Since the viscosity of the mixture was relatively low (80 cps), it was expected that the material could copy high-aspect-ratio structures without the application of vacuum. However, it was found that this process was not suitable for sharp tips, and this resulted in the process being performed under vacuum. The degassing process was the same as that of PLA. The cast PU was then cured at room temperature for 4 hours and post-cured at 65°C for 2 hours to both increase physical performance and enhance the metal transfer process. The epoxy resin was also processed under vacuum and was cured by UV light (OAI mask aligner, Optical Associates, Inc., San Jose, CA) with an exposure energy of 6000 mJ/cm^2 at 365 nm wavelength, followed by separation from the mold. In all cases, the metal layer originally residing on the PDMS mold was successfully transferred to the molded material, as shown in Figure 4.21.

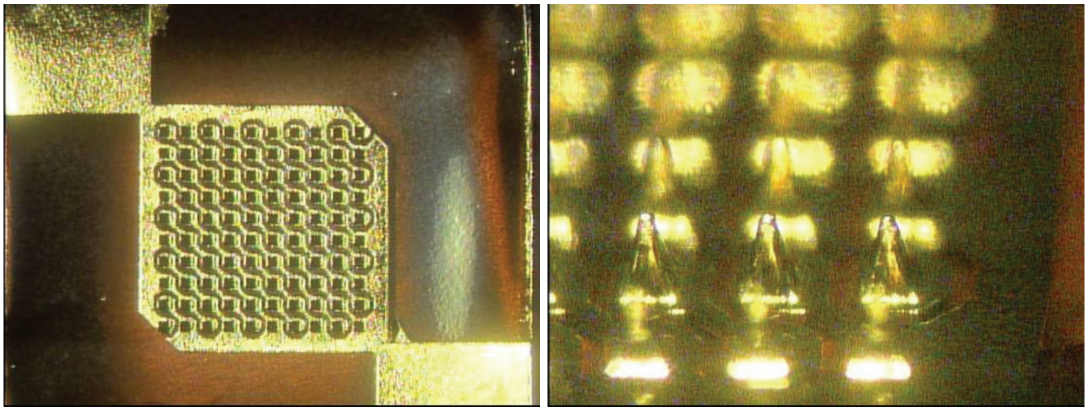

(a) (b)

Figure 4.21 Optical micrographs of the molded structure. The metal layer was successfully transferred to the molded material; (a) top view, and (b) side view

Before electroplating Ni to enhance the mechanical rigidity of the device, the sample was examined by scanning electron microscopy (Hitachi 3500H, Hitachi, Ltd., Tokyo, Japan). The SEM pictures of the fabricated device are shown in Figure 4.22.

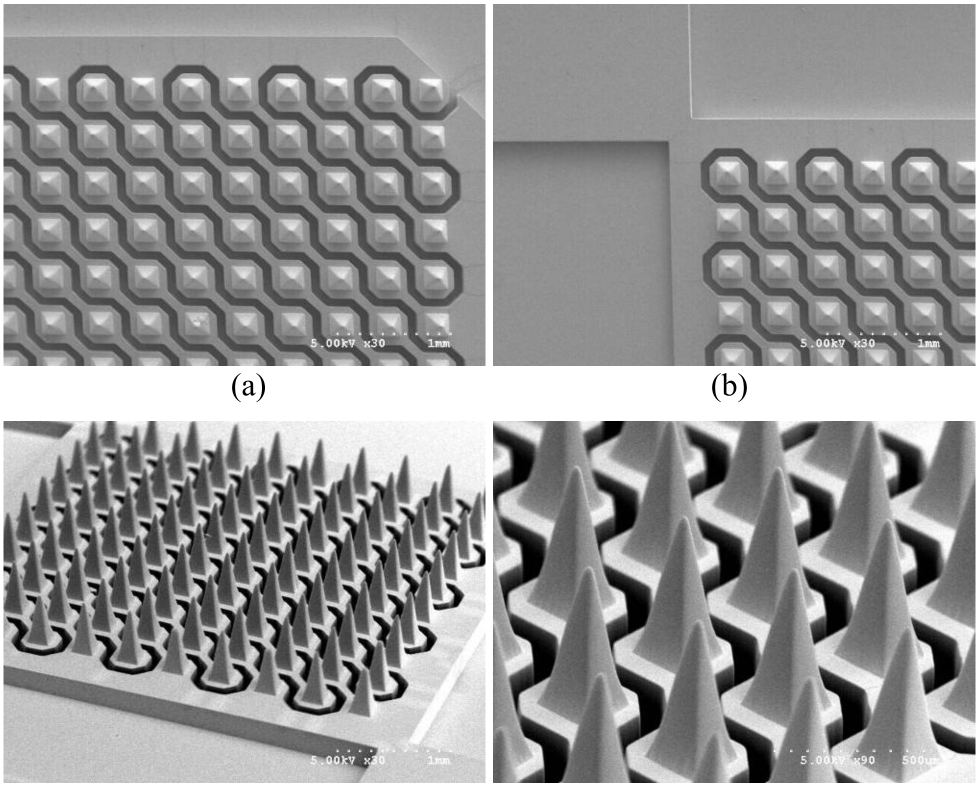

(a) (b)

(c) (d)

Figure 4.22 SEM pictures of the fabricated device; (a) Top view showing electrical isolation, (b) pad area, (c) oblique view of the device, and (d) close-up view of the microneedle array

After the examination, the sample was attached to a glass slide which bears a pre-deposited Cu seed layer. To make an electrical pathway between the sample and the glass slide, silver paste was applied to the edge of the sample. Once the silver paste was cured, the glass slide was covered with polyimide tape except for the sample area where Ni would be deposited. Ni electroplating was performed for 1.5 hours with a 10mA/cm^2 current density, resulting in the formation of an approximately 20µm thick Ni layer. The results of Ni-plating are shown in Figure 4.23.

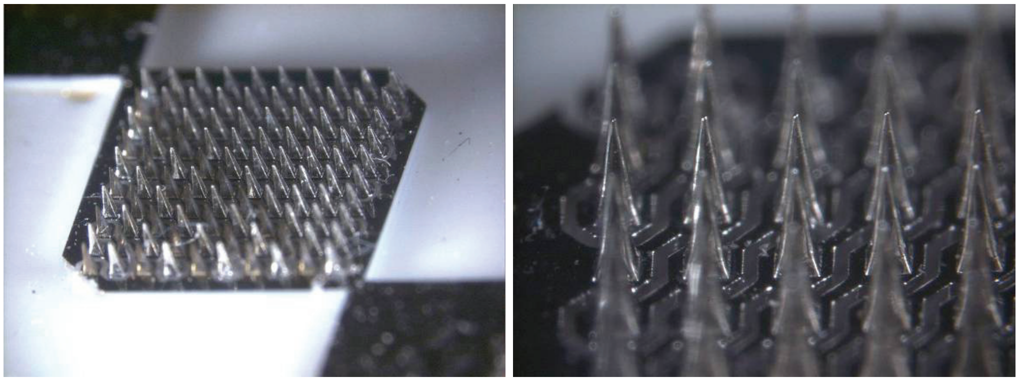
(a) (b)

Figure 4.23 Fabricated device after 20µm thick Ni electroplating; (a) overall view, and (b) close-up view

To implement an electrical connection to the pulse generator for electroporation, 200µm diameter micro-vias were drilled from the backside of the device using a CO_2 laser operating at 10 µm wavelength. Before drilling micro-vias, the backside of the device was covered with 25µm thick polyimide tape. The micro-vias were then filled with conductive ink by applying a vacuum. After the filling process, the excessive conductive ink was cleaned, followed by removal of the tape. The fabrication results are shown in Figure 4.24.

(a) (b)

Figure 4.24 Electrical interconnects through micro-vias; (a) overall view showing two micro-vias filled with conductive ink, and (b) close-up view of the micro-via filled with conductive ink

Once the electrical interconnects were formed, copper wires were attached to the interconnects using silver paste. For the electroporation experiments with cells, the device was firmly attached to a glass slide for convenient handling of the device.

4.3.2 Insertion Test

To verify the mechanical functionality of the microneedle array, an insertion test was performed using pig cadaver skin. The polymers used to fabricate microneedles arrays were: PU and PLA. Full-thickness pig skin with the subcutaneous fat removed was affixed to a wooden plate for the test. The fabricated microneedle array was placed on this affixed skin and insertion was attempted by applying pressure using the thumb. The array was taken off the wooden plate immediately after the test. A red tissue-marking dye (Shandon, Pittsburgh, PA, USA), which stains sites of stratum corneum perforation selectively, was applied to the site of insertion and gently cleaned with a swab after 10 min of exposure. After removal of residual dye, the skin was observed under an optical microscope. Also the tested microneedle array was examined optically. Figure 4.25 shows the stained pig cadaver skin and the microneedle array after the insertion test.

For the PU microneedle array, a few of the microneedles successfully penetrated the stratum corneum. However, it was found that most of the tips were bent during the test, indicating that a bare PU microneedle was not mechanically strong enough for insertion. In contrast to the PU microneedle array, the PLA microneedle array was successfully inserted into skin without severe damage. After careful examination under the microscope, it was found that while several tips were broken, most of the tips maintained their original shape.

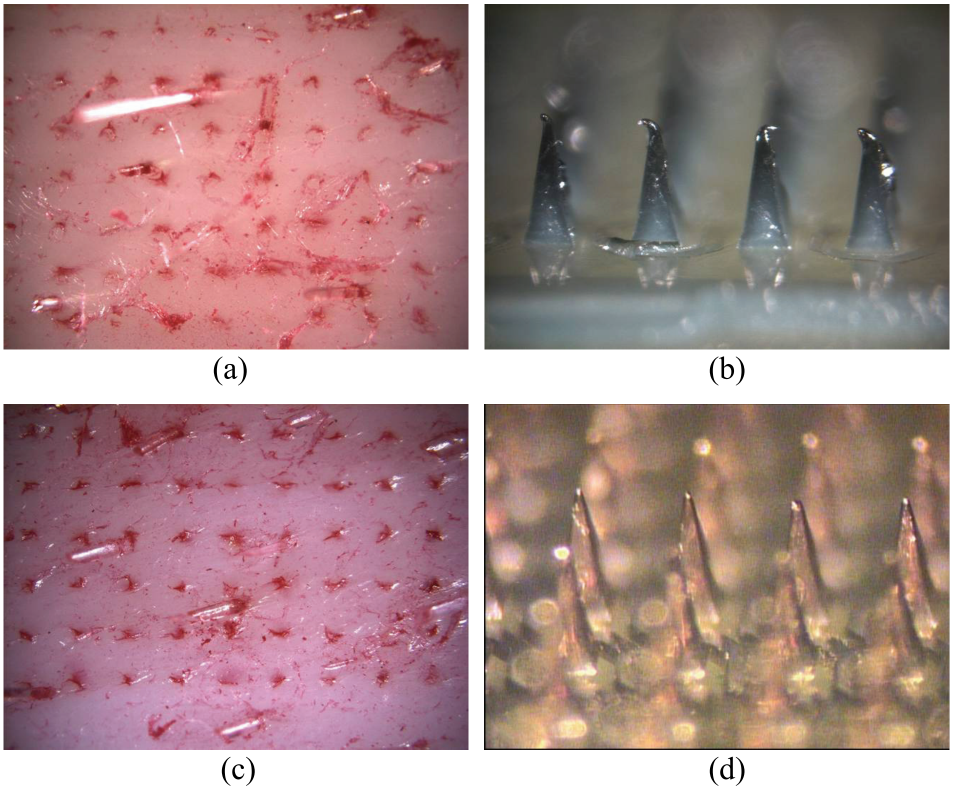
(a) (b) (c) (d)

Figure 4.25 Optical micrographs of the pig cadaver skin and the microneedle array after insertion test; (a) the stained pig skin after the insertion of PU microneedle array, (b) the PU microneedle array after the insertion test, (c) the stained pig skin after the insertion of PLA microneedle array, and (d) the PLA microneedle array after the insertion test

Since electrical functionality is required, all microneedle arrays need to be coated with a relatively thick layer of metal. In addition to providing electrical functionality the coated metal layer enhances the structural rigidity of the array, enabling skin penetration without damage. To determine the proper thickness of the metal layer, microneedle arrays with different layer thicknesses of Ni were prepared. For PU microneedle arrays, 5, 10, and 15 μm thick Ni layers were electroplated. After Ni plating, the devices were tested using the same protocol described in 4.2.2 and the results are shown in Figure 4.26.

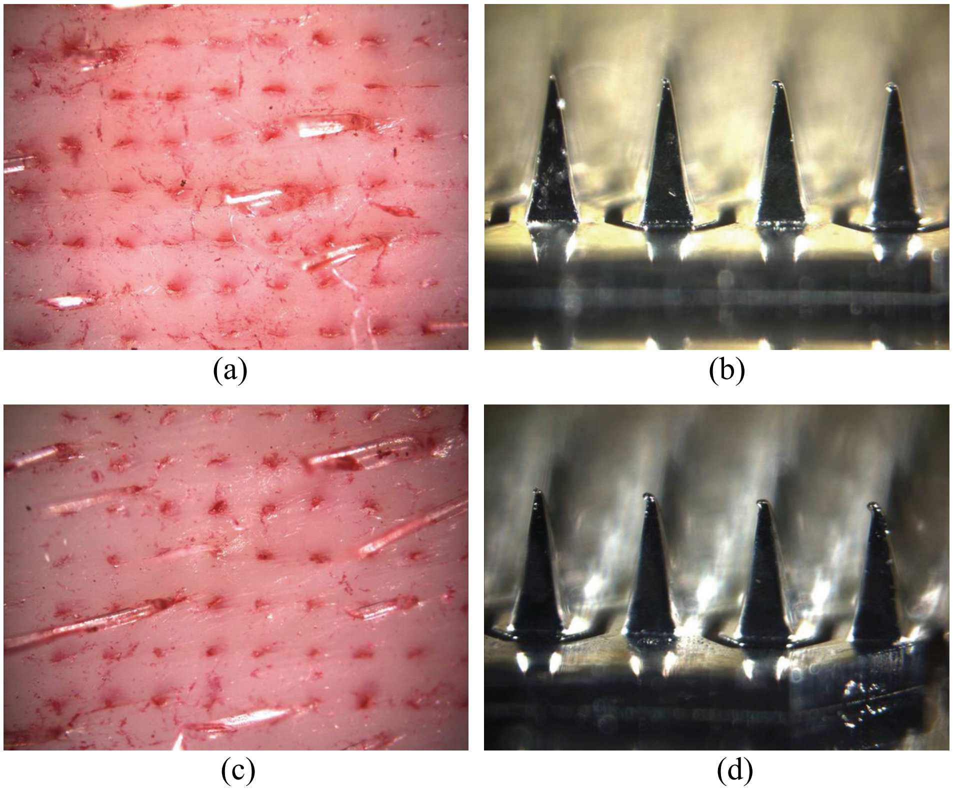

Figure 4.26 Optical micrographs of the stained pig cadaver skin and the Ni-plated PU microneedle array after multiple insertions; (a, b) 5 μm thick Ni, (c, d) 10 μm thick Ni, and (e, f) 15 μm thick Ni, respectively

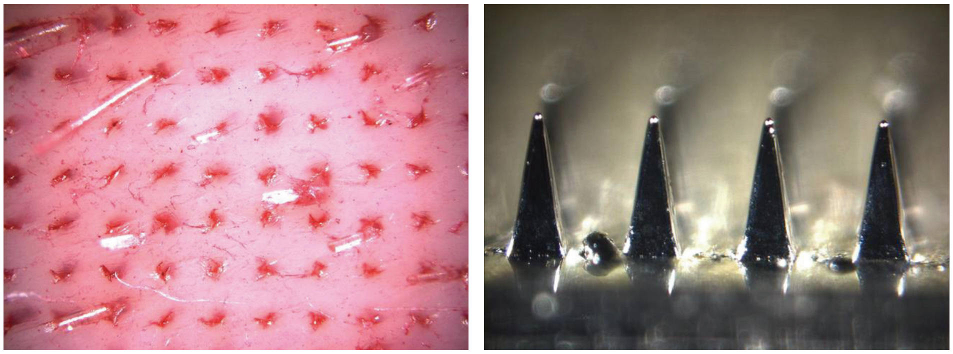
(e) (f)

Figure 4.26 continued

It was observed that all Ni-plated PU microneedle arrays were successfully inserted into the skin without tip bending or breaking. After multiple insertion tests, however, some of the tips with a 5 or 10 μm thick Ni layer were deformed. For the microneedle array with a 20 μm thick Ni layer, tip deformation was not observed after successive insertion tests. Since PLA is mechanically stronger than PU, it was expected that a PLA microneedle array would require a thinner Ni layer than PU for safe insertion. Based on the results from the PU microneedle array, a PLA microneedle array with a 5 μm thick Ni layer was prepared and tested. It was observed that it could be successfully inserted into skin without mechanical damage. The results are shown in Figure 4.27.

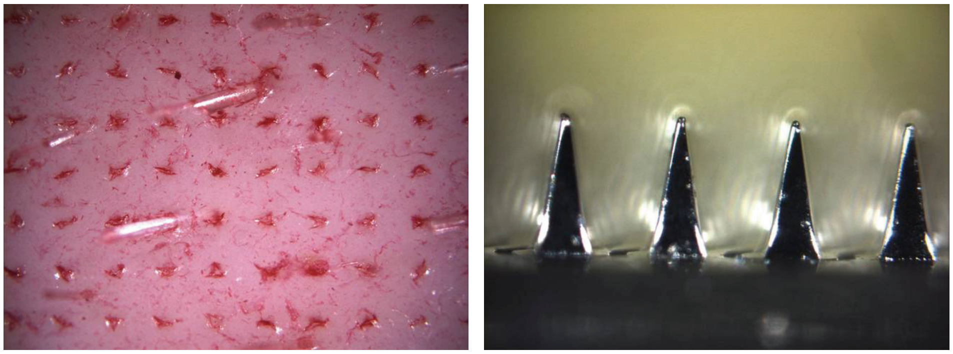
(a) (b)

Figure 4.27 Optical micrographs of (a) the stained pig cadaver skin and (b) the PLA microneedle array with a 5 μm thick Ni layer after multiple insertion tests

4.3.3 Electric Field Simulation

To estimate the distribution of electric field strength over the volume around the checkerboard-type microneedle arrays, a series of 2-D FE models was created in a similar way to the description of the parallel type microneedle array discussed in 4.2.3. Since the cross section of the device can be modeled by an array of squares, a 4 by 4 array of squares of various sizes was used to represent the microneedles at a certain height. For the analysis, 19 models were created to represent the cross section of the device at several heights. A voltage pulse of 4 V was applied between microneedles, and the electric field strength at each point defined by the grid was collected. The size of the grid was 1 μm by 1 μm, and approximately 30,000 data points were generated and exported to MATLAB for analysis. Figure 4.28 shows representative results of the FE simulation done by FEMLAB.

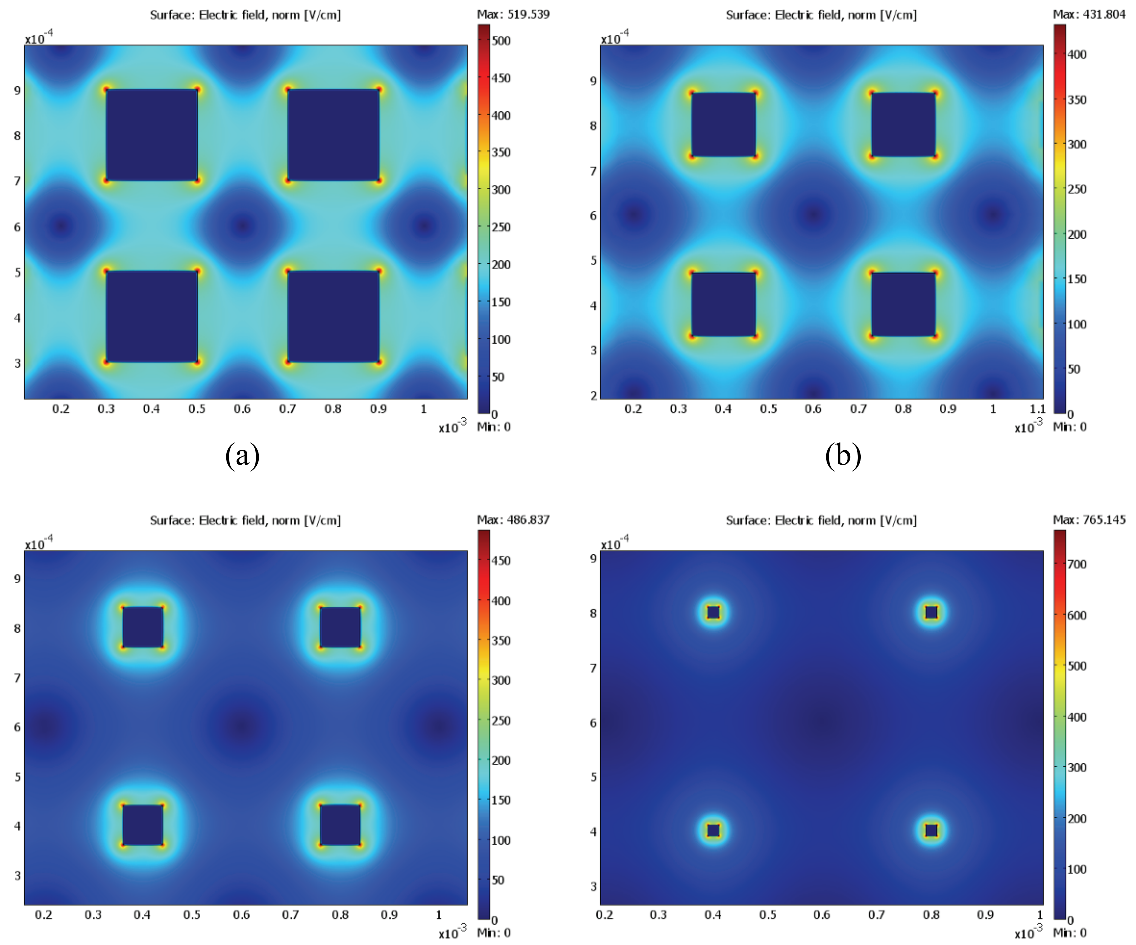

(a) (b)

(c) (d)

Figure 4.28 Electric field simulation results of 2-D FE models that represent the cross section of the pyramidal microneedle array at certain heights; (a) 1st slice, (b) 7th slice, (c) 13th slice, and (d) 19th slice

Due to symmetry in the 2-D model, only a quarter of the area surrounded by the four electrodes was examined for the analysis of the distribution of the electric field strength. Data containing information on the electric field strength in the selected area was created and exported to MATLAB for analysis. To examine the overall shape of the distribution at each height, a histogram was drawn based on the data, as shown in Figure 4.29.

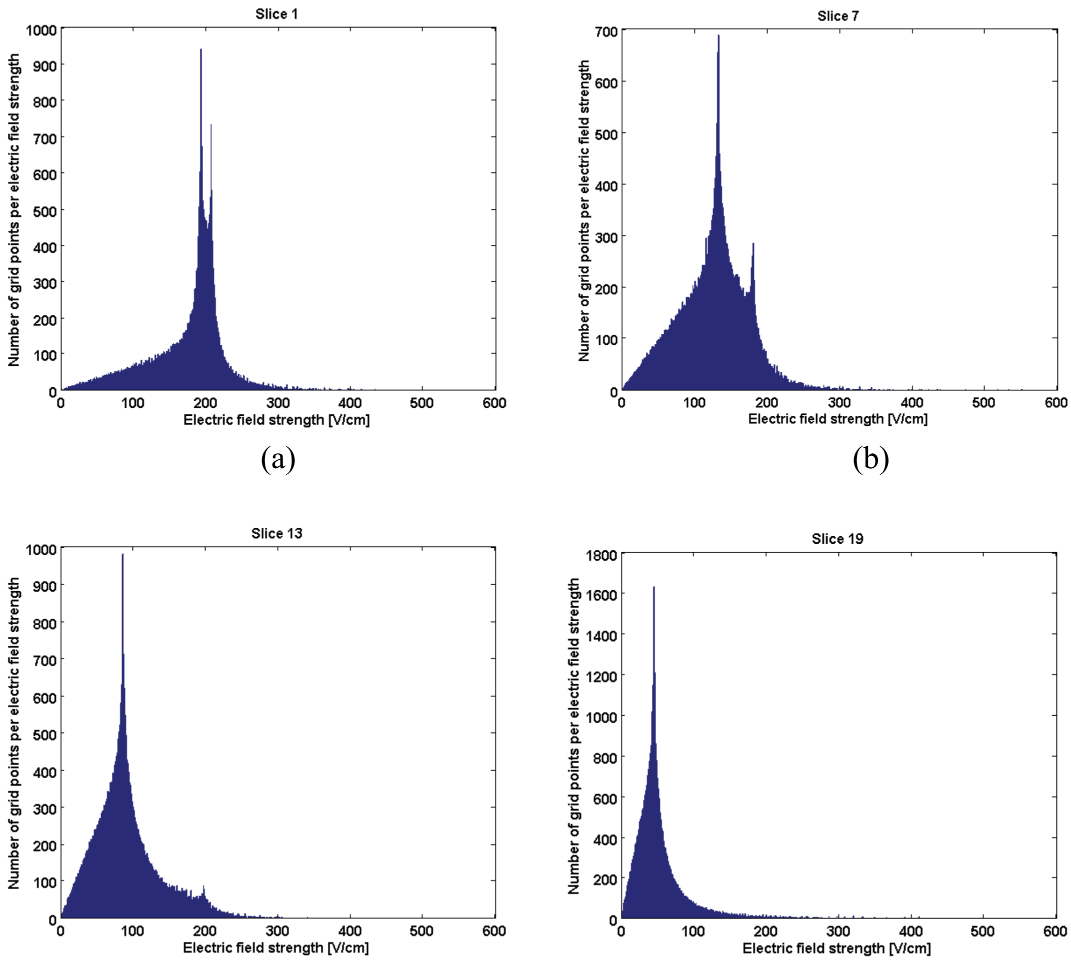

(a) (b)

(c) (d)

Figure 4.29 The distribution of the electric field strength for each 2-D models that represent the cross section of a 3-D model at certain heights; (a) at the bottom, (b),(c) in the middle, and (d) at the tip

After collecting data from 19 models, a 3-D distribution of electric field strength was approximated by the method described in section 4.1.3. After successive fittings, it was found that the overall distribution of the electric field strength was best fitted by the combination of 4 Gaussian functions. Figure 4.30 shows the normalized raw data and the fitted curve that represents the overall distribution of the electric field strength generated by the fabricated microneedle array.

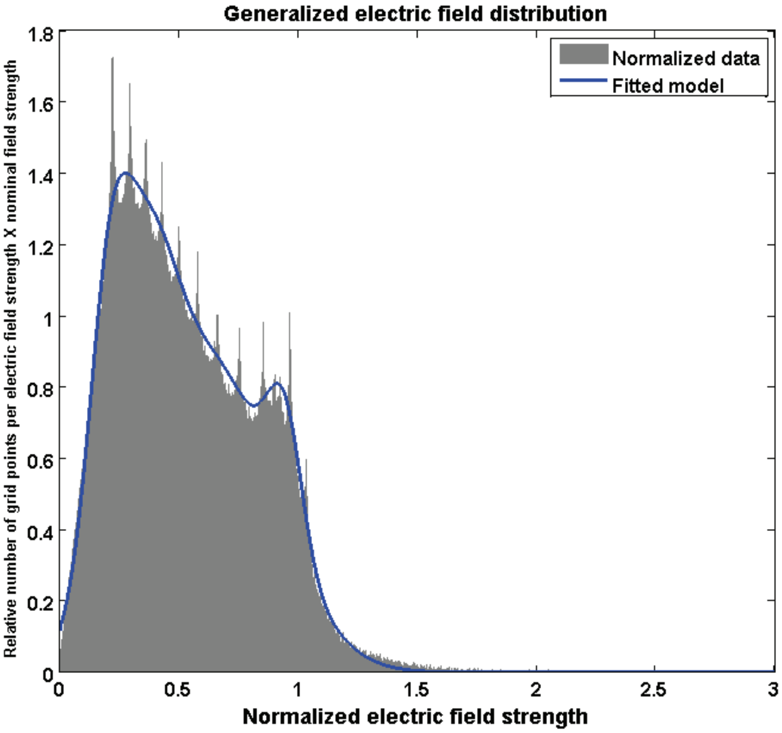

Figure 4.30 Normalized data from the 2-D FE models and the fitted model for estimating the overall distribution of the electric field strength generated by the microneedle array

The analytical expression of the fitted model is the sum of 4 Gaussian functions with the coefficient of determination R^2=0.9991 as follows:

$$f = \sum_{i=1}^{4} a_i \exp(-((x - b_i)/c_i)^2) \tag{4.5}$$

The coefficients for the fitted model are summarized in Table 4.1.

Table 4.1 Summary of the coefficients of the model

	a_i	b_i	c_i
1	0.7804	0.2122	0.127
2	0.5815	0.3744	0.1592
3	0.8751	0.6198	0.3857
4	0.3507	0.9449	0.1023

As discussed in 4.1.3, it is possible to estimate a volume fraction that contributes to the delivery of molecules into cells using the calculated model. Suppose that the target cell is DU 145 whose diameter is approximately 20µm. According to Schwann's equation (Eq. 2.1), the threshold electric field strength is 166 V/cm (0.5 V of transmembrane potential is used for calculation [128]). From the literature [129], approximately 90 % viability was achieved when a field strength of 500 V/cm with 2.8 msec pulse length was applied to DU 145 for calcein delivery. By defining a "window" with these bounds, it is possible to predict a volume fraction which contributes to effective electroporation at different voltages applied for experiments. For example, if voltages that induce the nominal field strength of 250 V/cm, 500 V/cm, 750 V/cm, and 1 kV/cm were applied, the effective volume fraction for electroporation can be calculated as 33 %, 63 %, 53 %, and 43 %, respectively. For each condition, the volume fraction in which the electric field strength exceeds the assumed upper limit is given as 0%, 6 %, 32 %, and 48 %, respectively.

The simulation results showed that the fabricated microneedle array generated an inhomogeneous electric field, and the effective volume for electroporation can be estimated from the models. This inhomogeneity of the electric field results in lower efficiency of the device, compared to the parallel-type macro cuvette. However, the fabricated microneedle arrays can achieve the field strength required for effective electroporation at lower voltages due to the smaller gap between electrodes. For example, plasmid DNA was successfully delivered into skin with parallel-type electrodes [130] by using electric field strengths of 400, 500, 750, and 1500 V/cm with a pulse length of 0.1 msec. The gap between electrodes was 6 mm. The voltages required to achieve these field strength ranged from 240 V to 900 V. If a fabricated microneedle array with a 200 μm gap were used, these field strengths could be achieved with a voltage less than 30 V. In addition, the volume fraction for effective electroporation can be calculated as 6.3 %, 21.4 %, 45.5 %, and 72.4 %, respectively by assuming that lower and upper bounds for electroporation are 400 V/cm and 1500 V/cm, respectively.

4.4 Conclusion

Two different types of the microneedle arrays were successfully fabricated and characterized. With proper thickness of metal layer, the fabricated microneedle arrays were able to penetrate skin without breakage of the tips. The distribution of electric field strength for each microneedle array was modeled using a series of 2-D FE models. From the distribution, it was possible to estimate the effective volume for electroporation when a specific range of electric field strength was defined.

CHAPTER 5

ELECTROPORATION WITH MICRONEEDLE ARRAYS

5.1 Introduction

To verify the electrical functionality of the fabricated microneedle arrays, electroporation experiments using bovine red blood cells (RBC) and human prostate cancer cells (DU145) were performed. The amount of hemoglobin released from red blood cells after electroporation with the fabricated microneedle arrays was measured to determine whether the arrays can achieve the minimum field strength required for electroporation. Calcein and bovine serum albumin (BSA) were selected as model molecules for electroporation-mediated uptake into mammalian cells. Calcein delivery experiments of can demonstrate whether that the fabricated microneedle arrays are capable of transporting small molecules across the cell membrane while maintaining cell viability; BSA delivery experiments can determine if large molecules can be transported using the fabricated device.

5.2 Parallel-type Microneedle Array

The electrical functionality of the fabricated microneedle array was examined using experiments with bovine red blood cells and human prostate cancer cells. The purpose of the red blood cell experiments was to investigate the formation of pores on cell membranes after application of an electric field between the microneedle electrodes. When cell membranes are permeable or disrupted by an external electric field generated by the microneedle array, hemoglobin inside cells is released into the extracellular environment. Hemoglobin can be released through pores formed in the cell membrane or by cell rupture. Both cases verify the electrical activity of the fabricated microneedle array. Since it is hard to discriminate between the two mechanisms, it was assumed that hemoglobin was released by only cell rupture. To examine whether impermeant molecules could be delivered through cell membranes, calcein and bovine serum albumin (BSA) delivery experiments were performed. The purpose of these experiments was to investigate the effects of external electric fields on uptake of molecules and viability of cells. For the effective delivery of molecules, it was desirable to optimize the electroporation parameters to those where high molecular uptake and high viability are achieved.

5.2.1 Hemoglobin Release Experiment

5.2.1.1 Red Blood Cell Preparation

Approximately 20 ml of bovine blood in Alsevers anticoagulant (Rockland Inc., USA) was measured into a 50 ml polypropylene centrifuge tube (BD Biosciences, San Jose, CA). Phosphate buffered saline (PBS) was added to the tube which was then centrifuged at 236×g (relative centrifugal force) for 10 minutes at room temperature. The supernatant was discarded and approximately 20 ml PBS was added for another wash. A total of three PBS washes were done, after which the supernatant was discarded and a resultant RBC pellet was formed, which was used intact for experiment.

5.2.1.2 Electroporation Apparatus and Protocols

To apply an electric field, a high pulse voltage source (BTX ElectroCell Manipulator 600, Genetronics, San Diego, CA) was connected to the microneedle array. This system can supply voltages ranging from 10 V to 2.5 kV with an exponential decay waveform. The pulse length can be adjusted by changing the resistance and the capacitance of the system. The actual voltage and the pulse length delivered by the system was measured using an oscilloscope (TDS 2014B, Tektronix Inc., Beaverton, OR) connected to the system.

The microneedle array under testing was fixed to a glass slide with the microneedles facing up. The array was connected to the electroporation apparatus to provide a controlled pulse with an exponential decay waveform. For each electroporation experiment, 25 μl of RBC pellet was pipetted onto the microneedle array.

After pulse application, the 25 μl RBC suspension was pipetted off into a centrifuge tube (Eppendorf 1.5 ml tube, Eppendorf North America Inc., Westbury, NY). One ml of PBS was added and the suspension was centrifuged at 735×g for 5 min at room temperature. After centrifugation, 700 μl of the supernatant was collected for absorption spectroscopy to quantify the amount of hemoglobin released. A negative control was prepared by repeating this procedure without the application of the electrical pulse. A positive control was also prepared by lysing 25 μl RBC pellet with 1 ml deionized water. All experimental conditions were repeated three times to generate triplicate data points. A total of two identical microneedle arrays were used to perform the electroporation experiments. The arrays were washed with PBS between each electroporation experiment.

The amount of released hemoglobin was quantified by measuring the absorbance of the supernatant at 575 nm (Spectramax plus 384, Molecular Devices, USA). Hemoglobin release after electroporation was calculated as a percentage of total hemoglobin (positive control) and reported as RBC lysis (%). Since only 6 μl of the 25 μl RBC dispensed on the array was in the electric field, the results were normalized by multiplying by a factor of 4.17. RBC lysis from different electroporation conditions were statistically compared with $\alpha = 0.05$.

5.2.1.3 Experimental Results

Based on the protocols previously described, hemoglobin release experiments were performed. After electroporation, RBCs rupture and release hemoglobin that can be easily quantified by absorption spectroscopy. 25 μl of washed and pelletted RBC pellet was spread over the microneedle array and three different peak voltage levels: 53, 108 or 173 V, were applied using (i) 1 pulse with an exponential decay time constant $\tau = 0.5$ ms, (ii) 3 pulses with $\tau = 0.5$ ms, or (iii) 1 pulse with $\tau = 1$ ms. The inter-pulse spacing for the 3-pulse experiment was 20 s. After pulse application, the RBC pellet was collected and diluted with 1ml PBS. Centrifugation was used to remove RBC from the supernatant, ensuring that only hemoglobin release was measured by spectroscopy at 575 nm absorption.

Results from RBC electroporation via microneedles are shown in Figure 5.1. The figure summarizes all the electroporation conditions used. Percent RBC lysis is represented along the y-axis and the results are grouped on the x-axis according to the voltage applied. There is a statistically significant increase in electroporation of RBCs as the applied voltage increases (ANOVA, p<0.0001). Electroporation of as high as 90% was achieved at 173 V and 1 pulse with 1 ms pulse duration. RBC lysis also increased with both pulse length and pulse duration (ANOVA, p<0.0001).

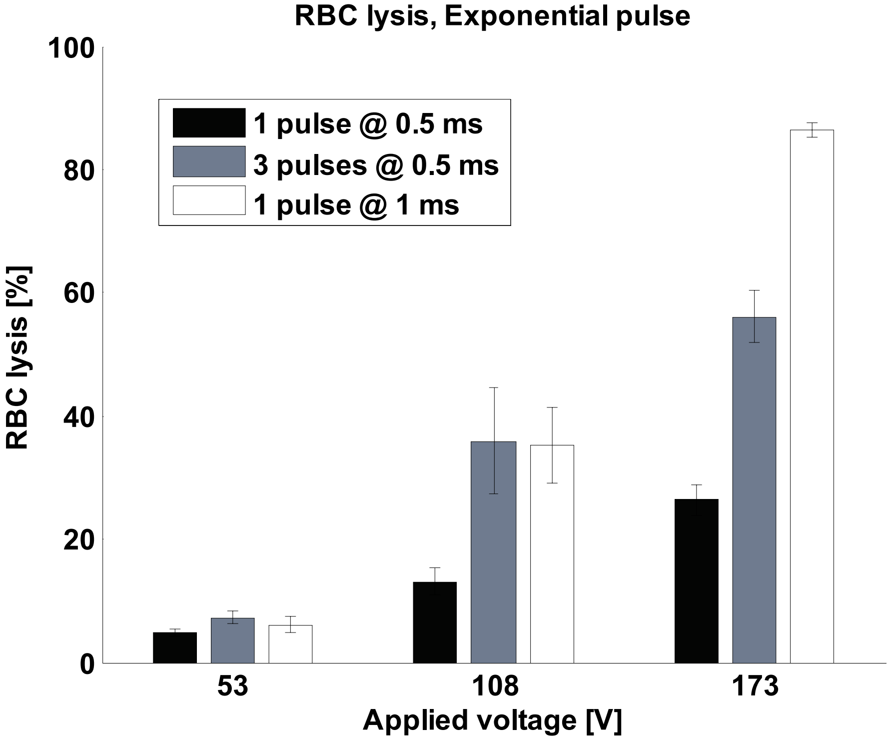

Figure 5.1 Hemoglobin released from red blood cells after electroporation using the microneedle electrode array

Since electroporation is a threshold phenomenon, it can only occur when the induced transmembrane potential exceeds a certain value, typically 0.2-1 V. Previous studies have reported that the threshold field strength for hemolysis of human red blood cell was approximately 4 kV/cm with 15 μs pulse length [131], and the threshold for delivering molecules into human red blood cell ghosts (red blood cells with the hemoglobin removed) ranged 0.5–2 kV/cm with 1-2 ms pulse length [128]. For 1 kV/cm field strength, the transmembrane voltage was calculated using Schwan's equation to be approximately 0.5 V.

In this study 0.5–1ms pulse length was used and RBC hemolysis seems to first occur near 50 V, which corresponds to 2-3 kV/cm field strength depending on the location of the microneedle electrodes. This value is quite reasonable compared to previous studies [128, 131]. Since we used a highly concentrated RBC pellet, Schwann's equation can not be applied to directly calculate the threshold voltage because Schwann's equation models a single sphere in a homogeneous electric field. As the density of cells in the suspension increases, the electric field is locally distorted by neighboring cells. Susil et al. [132] described the relationship between transmembrane potential and cell density, and it showed that the form factor (the 3/2 term in Schwann's equation) disappears when cells are fully packed (i.e. the interspacing between cells is zero). Assuming that the RBC pellet is fully packed, the radius of the RBC is 3.3 μm [133], and the distance between electrodes is 150 μm, an applied voltage of 50 V should induce a transmembrane voltage of approximately 1.1 V, which exceeds the threshold for electroporation.

Using these hemoglobin release experiments, it was proven that fabricated microneedle arrays are electrically active and capable of generating sufficient electric field strength to electroporate red blood cells.

5.2.2 Calcein Delivery Experiment

5.2.2.1 Human Prostate Cancer Cell (DU145) Preparation

Human prostate cancer cells (DU145, American Type Culture Collection, Manassas, VA, USA, item no. HTB-81) were grown on T-150 flasks (BD Falcon, Franklin Lakes, NJ, USA) as monolayers in RMPI-1640 medium, supplemented with 100 μg/ml penicillin-streptomycin (Cellgro, Mediatech, Herndon, VA, USA) and 10%(v/v) heat inactivated fetal bovine serum (Atlanta Biologicals, Atlanta, GA, USA) in a humidified condition of 5% CO_2 at 37°C. DU145 cells were harvested using 5 ml Trypsin-EDTA (Cellgro) to detach adherent cells from T-150 flasks. Cells were centrifuged at 1000×g (Beckman Coulter, Fullerton, CA, model GS-15R) after harvest and resuspended in fresh complete media.

5.2.2.2 Experimental Protocols

DU145 samples were prepared at a concentration of 2.5×10^6 cells/ml. Calcein (623 Da, radius = 0.6 nm; Molecular Probes, Eugene, OR, 22 catalog no. C481), a green fluorescent molecule that cannot cross intact cell membranes, was used to quantitatively monitor the transport of molecules across the membranes of viable cells. Prior to electroporation, calcein at a concentration of 30 μM was added to the cell suspension, and homogeneously mixed by vortexing.

6 μL of DU145 samples were suspended on the microneedle array and collected after application of voltages ranging 10–45 V with an exponential decay waveform. This step was repeated 10 times to collect 60 μL of cell samples per condition. The samples were incubated at 37 °C for 10 min and were washed with PBS (Cellgro) and washed

with PBS by centrifugation (3500×g, 5 min, Eppendorf 5415C, Brinkman, Westbury, NY, USA) three times to remove extracellular calcein from the supernatant. The subsequent cell pellets were resuspended in a final volume of 60 µl of PBS containing 2 µl of propidium 25 iodide (PI) (Molecular Probes, catalog no. P-1304), a viability marker that stains nonviable cells with red fluorescence.

Flow cytometry was used to determine molecular uptake, i.e., fraction of cells containing intracellular calcein, and loss of cell viability by detecting the fluorescence intensity of intracellular calcein and propidium iodide, respectively, on a cell-by-cell basis. A BD LSR benchtop flow cytometer (BD Biosciences, San Jose, CA, USA) was used to measure the fluorescence of cells with calcein uptake (FITC fluorescence excited using a 488 nm Argon laser, 530/28 nm bandpass filter) and to distinguish viable from nonviable cells by the red fluorescence of propidium iodide (Per-CP fluorescence excited using a 633 nm HeNe laser, 670 nm longpass filter). Each analysis sampled approximately 20000 cells.

A Zeiss LSM 510 multiphoton microscope (Zeiss, Thornwood, NY) with an oil-immersion lens of 40× magnification was used to image 5µL of cell sample placed on a 25mm microscope cover glass (Fisher Scientific, Waltham, MA, USA). Similar lasers and filtersets to the flow cytometer were used in order to get comparable results.

5.2.2.3 Experimental Results

Figure 5.2 shows fluorescent images taken with the multi-photon microscope. The left image shows the green channel, and the right image shows the red channel. The delivery of calcein into cells by electroporation is determined by the presence of green fluorescence, and dead cells are shown by the presence of red fluorescence. By examining the images from the multi-photon microscope qualitatively, it was found that the number of cells with uptake of calcein increased as the applied voltage increased. Also, the number of dead cells showed a similar trend. No fluorescence in control (non-electroporated) samples was observed, indicating that fluorescent cellular effects were caused by electroporation.

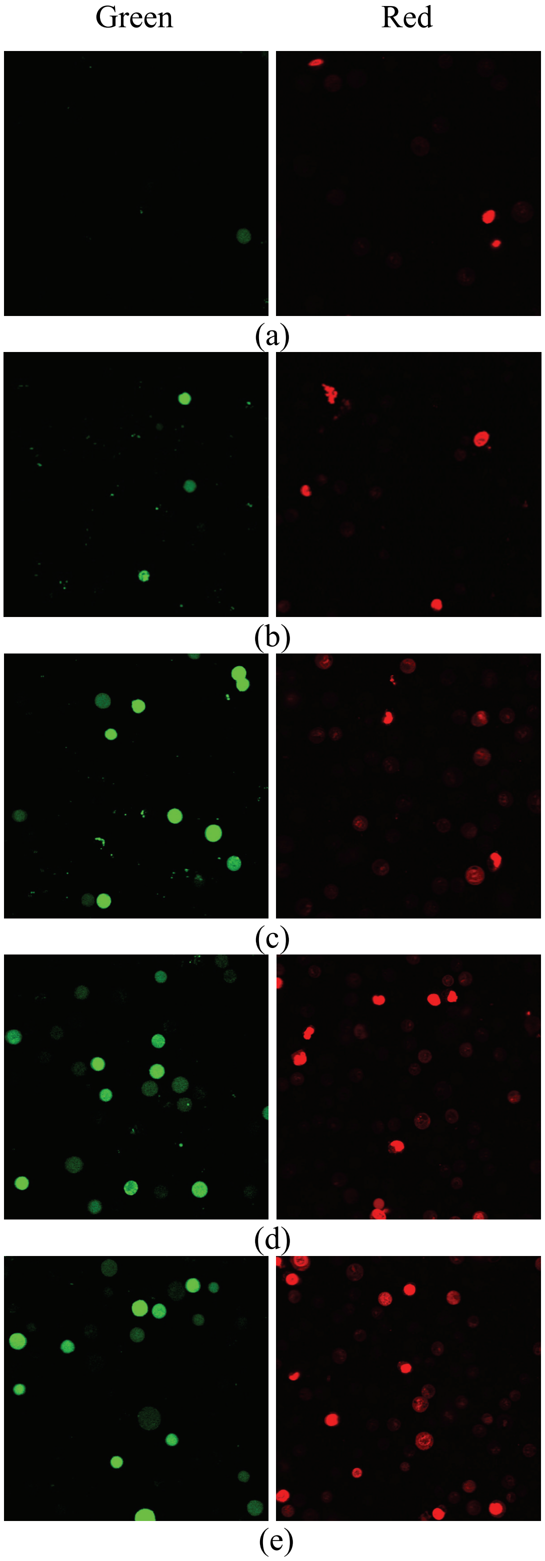

Figure 5.2 Confocal microscopy images of DU 145 after electroporation under different applied voltages; (a) control, (b) 11 V, (c) 23 V, (d) 37 V, and (e) 50 V, respectively.

Flow cytometry was used to quantify the effects observed in microscopy. For each sample, 20000 cells were examined at a maximum rate of 550 cells/sec. Figure 5.3 shows a typical histogram output as obtained via flow cytometry. The X-axis represents the level of green fluorescence (arbitrary units), and the Y-axis represents the number of cells with a particular level of fluorescence. The fluorescence of the control was due to autofluorescence, calcein surface binding, and noise from the flow cytometer. As compared to controls, electroporated cell populations had higher green fluorescence intensity, indicating that calcein was delivered across the cell membrane. This effect increased as the applied voltage increased. Using the histogram data, the percentage of uptake cells was determined using analysis software, FCS Express (De Novo Software, Los Angeles, CA). Similarly, the viability of the electroporated cells was calculated using the red fluorescence channel, which corresponds to the intensity level of propidium iodide among the cell population. Non-electroporated cells were normalized to have 100% viability. An increase in red fluorescence indicates that a cell has lost viability. As shown in Figure 5.4, about 40% of cells had calcein uptake at 50V with high viability (~90%).

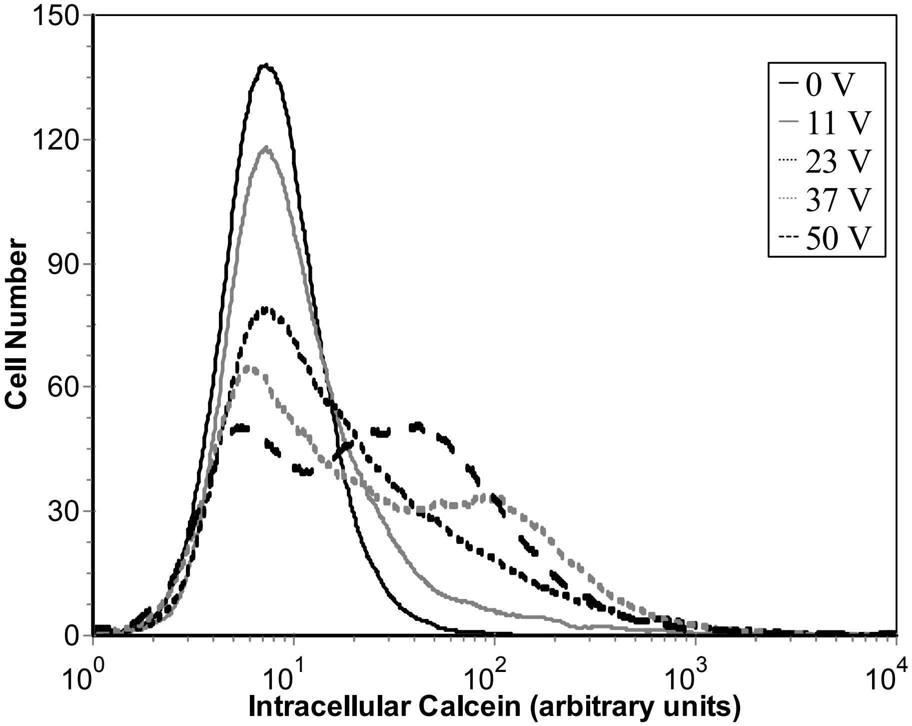

Figure 5.3 Flow cytometry results of calcein uptake at different conditions

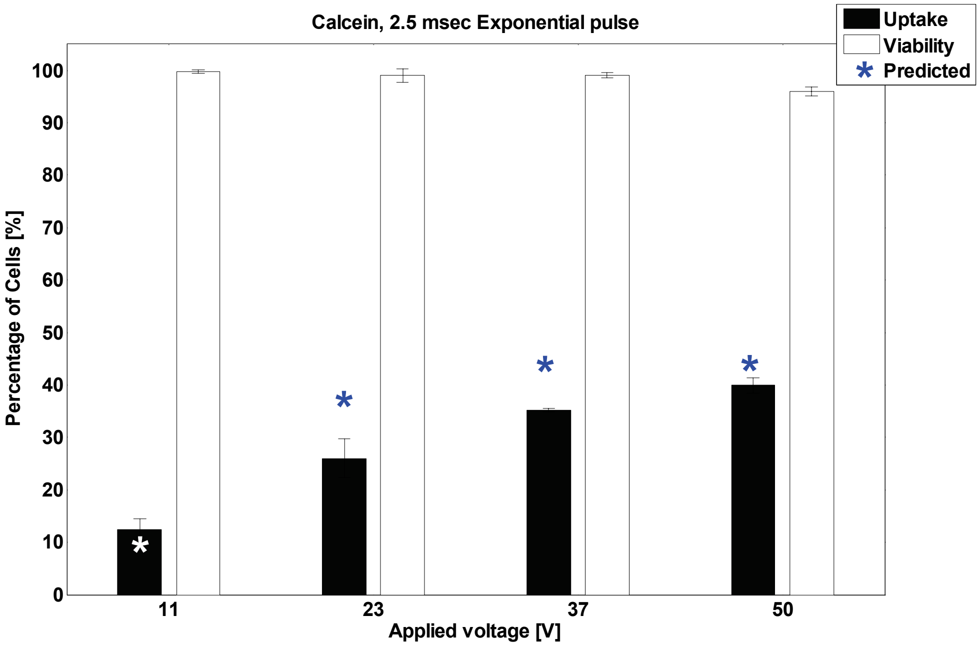

Figure 5.4 Calcein uptake and cell viability with respect to applied voltages

DU145 cells are spherical cells with a diameter of 20 ± 2 μm. At a cell concentration of 2.5×10^6 cells/ml, the volume percentage occupied by the cells is only 1%. Therefore, Schwan's model can be applied to estimate the threshold voltage for electroporation. The electric field strength needed for electroporation using this model is calculated to be 333 V/cm at $\varphi=0$, assuming that the transmembrane potential is 0.5 V. Figure 5.4 shows that calcein was delivered to approximately 10 % of the cells at 11 V, indicating that 11 V can generate an electric field strong enough to electroporate DU145 cells. With the applied voltage of 11 V, the electric field strength at the microneedle substrate was 733 V/cm and the induced transmembrane potential was 1.01 V, calculated using Schwann's equation. This result is also comparable with our previous electroporation studies performed with a 2-mm gap cuvette [129]. In that study, the field strength required for uptake of calcein varied with pulse length (~0.7 kV/cm for 1 ms, ~0.4 kV/cm for 10 ms), suggesting that not only electric field strength but also pulse length is strongly involved in the transporting mechanism. Typically, a high field strength is needed to electroplate cells at a short pulse length. We used a 2.5 millisecond pulse length, implying that the field strength required for electroporation exists the value between 0.4 kV/cm and 0.7 kV/cm, which is consistent with the results shown in Figure 5.4.

In chapter 4, a model for estimating the distribution of electric field strength was described. According to data reported in the literature [129], uptake of calcein requires a minimum of 0.5 kV/cm to occur with a 2.8 ms exponential decay pulse. This pulse condition is similar to that reported in this work (2.5 ms, exponential decay pulse); therefore, the electric field strength of 0.5 kV/cm can be used as the lower limit for effective electroporation. The calcein delivery experiments performed in this work showed that cell viability began to decrease at 3.3 kV/cm; thus, this field strength was used for as the upper limit for effective electroporation. With these values as the “window” for effective delivery of calcein, the volume fraction that contributes to electroporation at each applied voltage can be estimated from the model as: 21 %, 76 %, 91 %, and 91 %, respectively. For each condition, the volume fraction that can cause cell death is: 0 %, 0 %, 0.19 %, and 3.54 %, respectively. Assuming that the uptake efficiency is 50 %, then the percentage of cells with uptake at each applied voltage (11, 23, 37, and 50 V) can be estimated as: 10.5 %, 38 %, 45.5 % and 45.5 %, respectively, as shown in Figure 5.4.

5.3 Checkerboard-type Microneedle Array

The checkerboard-type microneedle array discussed in chapter 4 was tested using human prostate cancer cells. Two different types of pulses (i.e. exponential and square) were used to deliver molecules into the cells. In addition to calcein, fluorescein-tagged bovine serum albumin (BSA) was chosen as a large molecule model.

5.3.1 Calcein Delivery Experiment

5.3.1.1 Calcein Delivery Using Exponential Pulse

To validate the electrical functionality of the fabricated device, calcein delivery experiments were performed with human prostate cancer cells. To create an electric field between microneedle electrodes, the fabricated device was connected to the pulse generator using the protocols for the experiments described previously. The pulse width was fixed to 2.5 ms, and 7 different voltages were applied. For each experiment, 6 μl of cell suspension at a concentration of 2.5 million cells per ml was spread over the device and collected with a micropipette. Since the amount of a sample was insufficient for the analysis by flow cytometry, 10 experiments were performed for each experimental condition to make a 60 μl sample. To examine the consistency of the results, each experiment was performed three times and the results were averaged.

Figure 5.5 shows the representative pictures taken by the confocal microscope for each experimental condition. Each picture contains 4 sections, and each section represents an image taken by different channels such as normal, green fluorescence, red fluorescence, and a combination of all channels.

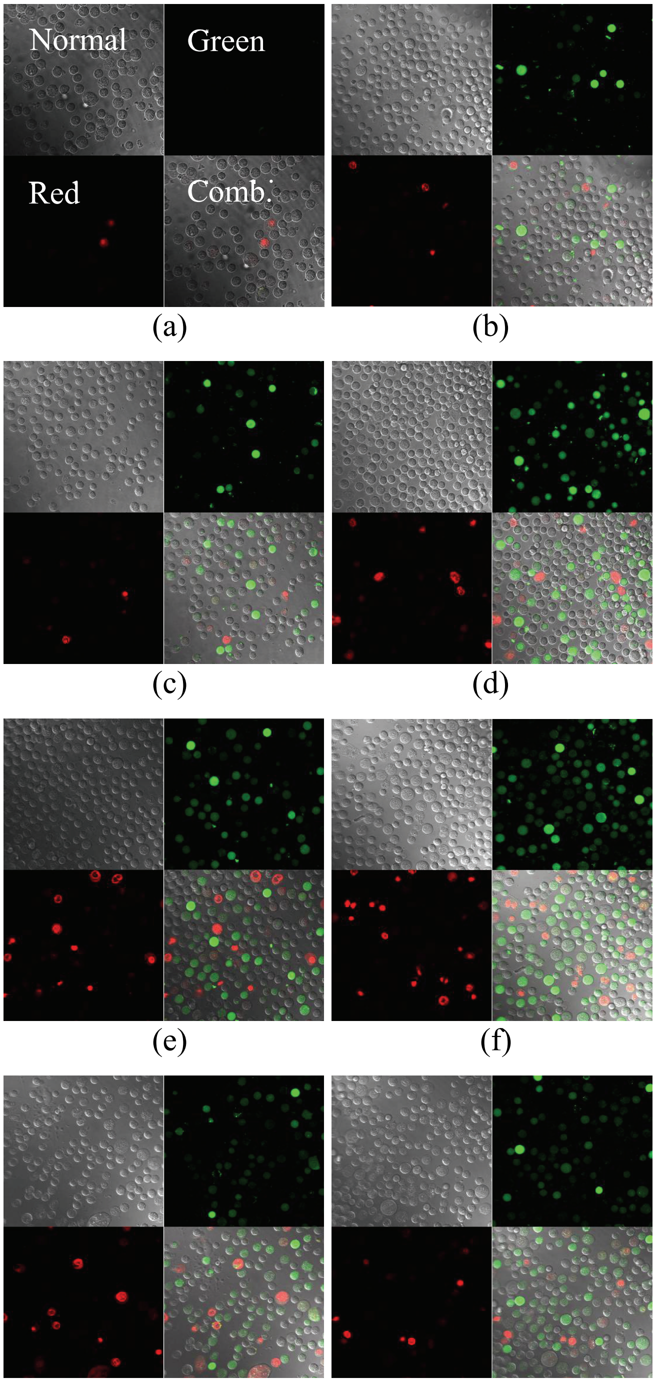

(a) (b) (c) (d) (e) (f) (g) (h)

Figure 5.5 Confocal microscopic images of human prostate cancer cells after the delivery of calcein by electroporation; (a) control, (b) 12 V, (c) 25 V, (d) 38 V, (e) 49 V, (f) 69 V, (g) 82 V, and (h) 91 V applied for the experiment

Six μl was extracted from the 60 μl total sample for confocal microscopy. The remaining sample was diluted with 200 μl PBS for flow cytometry. By examining the pictures from confocal microscopy, it was possible to see the effect of the applied electric field on the delivery of calcein qualitatively. As shown in Figure 5.5, the number of cells with uptake of calcein increased as the applied voltage increased, and the maximum uptake seemed to occur at 69 V. After 69 V, the number of cells with uptake started to decrease. To examine the results quantitatively, samples were analyzed by flow cytometry. The raw data from the flow cytometer was further processed by FCS Express (De Novo Software, CA, USA) to quantify the uptake and viability of each sample. Since each experiment was triplicated, the result from each experiment was averaged. The results are shown in Figure 5.6 with error bars (standard error).

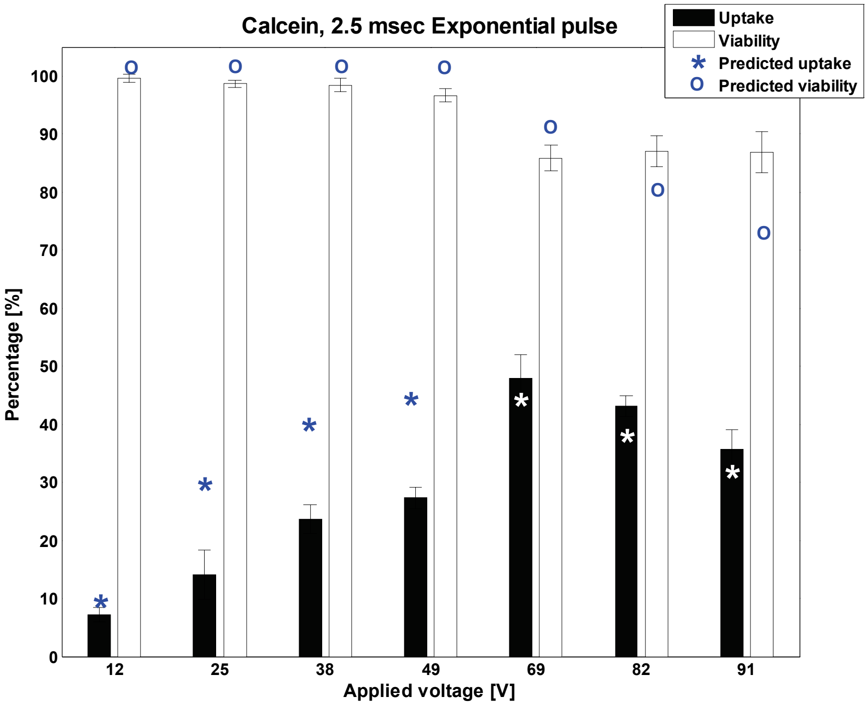

Figure 5.6 Uptake of calcein and cell viability at each applied voltage

When 12 V was applied for 2.5 ms, the average uptake of calcein was 7 %. The uptake of calcein increased until 69 V was applied and then decreased as the applied voltage increased. At 69 V, which corresponds to the nominal field strength (applied voltage divided by the distance between electrodes at the bottom of the device) of 3.45 kV/cm, a maximum uptake of 48 % was achieved. However, cell viability suddenly dropped at that point, indicating that the field strength induced by the applied voltage started to cause cell death rather than uptake of calcein.

The gap between the microneedle electrodes varies along the height, ranging from 200 μm to 400 μm. From Schwann's equation, the induced transmembrane potential at an applied voltage of 12 V can be calculated, and it ranges from 0.45 V to 0.9 V depending on the gap between the electrodes. It has been observed that electroporation occurs if the transmembrane potential exceeds a value of 0.2-0.5 V for pulses longer than 100 μs [128], therefore, our results are in good agreement with previous observations.

Using the model of electric field strength distribution with the same window defined in section 5.1.1.3, the effective volume fraction for calcein delivery at each condition (list) can be estimated as: 19 %, 60 %, 79 %, 87 %, 84 %, 74 %, and 69 %, respectively. In addition, the volume fractions of field strength higher than upper limit are: 0%, 0%, 0%, 0.25 %, 9.7 %, 21 %, and 26.8 %, respectively. If the uptake efficiency is assumed to be 50 %, then the percent of cells with uptake can be predicted as 9.5 %, 30 %, 39.5 %, 43.5 %, 42 %, 37 %, and 34.5 %, respectively. It is apparent that the overall trend estimated from the model is similar to that of the experimental results, as shown in Figure 5.6. Although the effective volume fraction at 49 V was higher than at 69 V, according to the model, the actual uptake of calcein at 69 V was higher than at 49 V. This can be interpreted as follows: the number of pores created by an external electric field depends on the field strength. As the field strength increases, the number of pores also increases. This implies that there is much higher chance to transport molecules across the cell membrane as the field strength becomes higher. The portion of the effective volume containing high field strength becomes larger as the applied voltage increases. For example, 23 % and 45.8 % of the volume exceeds 2 kV/cm when the applied voltages are 49 V, and 69 V, respectively.

5.3.1.2 Calcein Delivery Using Square Pulse

For effective delivery of molecules into cells by electroporation, experimental parameters such as field strength, pulse length, number of pulses, and pulse shape must be considered. By optimizing these parameters, it is possible to maximize cell permeabilization and viability. Traditionally, a cuvette containing parallel electrodes inside has been used for electroporation of cells *in vitro*. Since the electric field induced by parallel electrodes is homogeneous, it was possible to achieve more than 90 % of uptake with high viability by optimizing experimental parameters. As shown in the previous chapter using an electric field simulation, the fabricated microneedle array inherently generates an inhomogeneous field, suggesting that it is valuable to study the influence of experimental parameters for delivery of molecules by this modality of electroporation. In this study, the effect of pulse length on calcein delivery into human prostate cancer cells was examined using a square pulse. To apply a square pulse to the fabricated device, a square pulse generator (Pulse Agile, Cyto Pulse Sciences, Inc., MD, USA) was connected to the microneedle array, and an oscilloscope was also used to examine the actual pulse shape, length, and magnitude in situ. The experimental protocol was the same as that for exponential pulse experiments, described previously. A total of 4 different voltages were applied for the experiments, and 3 different pulse lengths were tested. Originally, the applied voltages were set to be 20, 40, 60, and 80 V, but actual voltages measured for the oscilloscope were 19, 38, 57, and 75 V, respectively. The actual pulse length was the same as the pre-set value in the pulse generator. Both confocal microscopy and flow cytometry were used for the analysis, and the representative pictures taken from the confocal microscope are shown in Figure 5.7.

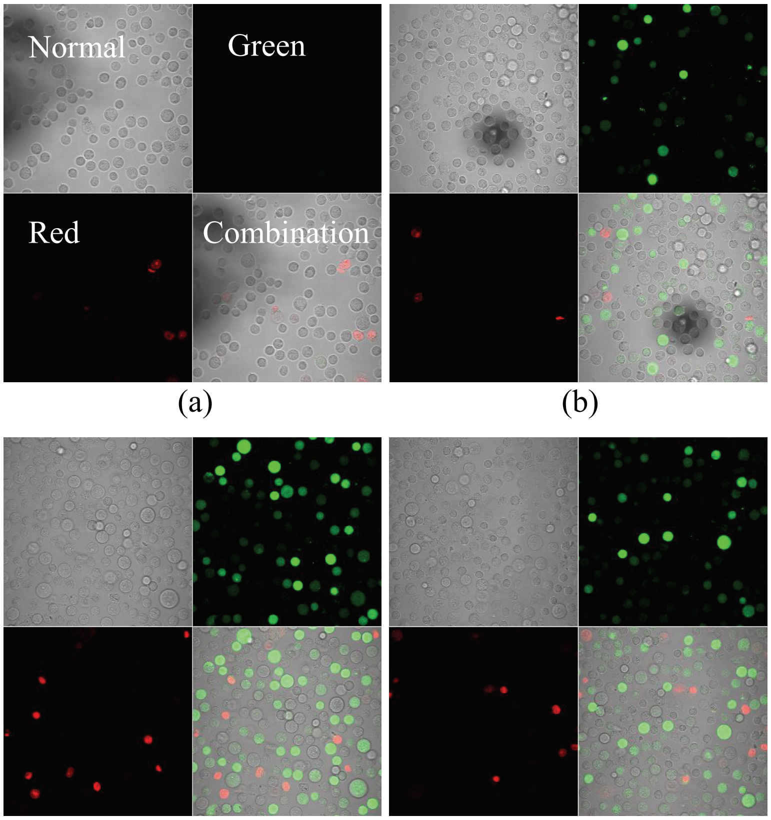

(a) (b)

(c) (d)

Figure 5.7 Confocal microscopic images of human prostate cancer cells after electroporation. Calcein was delivered into the cells with 2 ms square pulse by different voltages; (a) control, (b) 19 V, (c) 38 V, (d) 57 V, and (e) 75 V

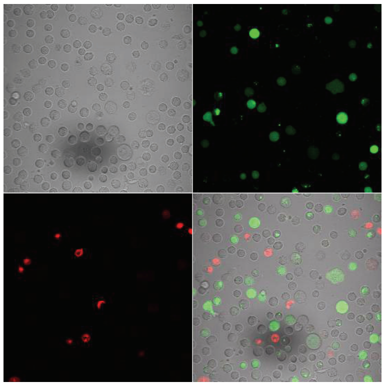

(e)

Figure 5.7 continued

To examine the effect of pulse length on cellular uptake of calcein, three different pulse lengths (0.5 ms, 1 ms, and 2 ms) were used. For each pulse length, 4 different voltages were applied as described before, and each sample was analyzed by flow cytometry. Figure 5.8 - 5.10 show uptake and viability data for each pulse length.

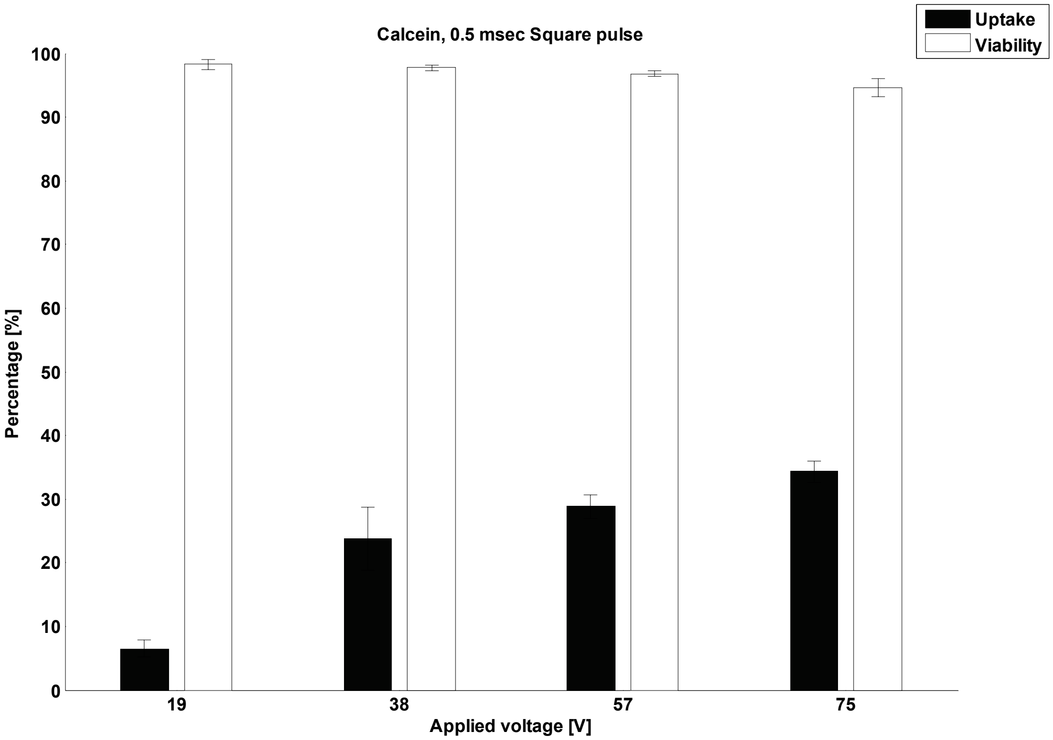

Figure 5.8 Uptake and viability for a 0.5 ms square pulse

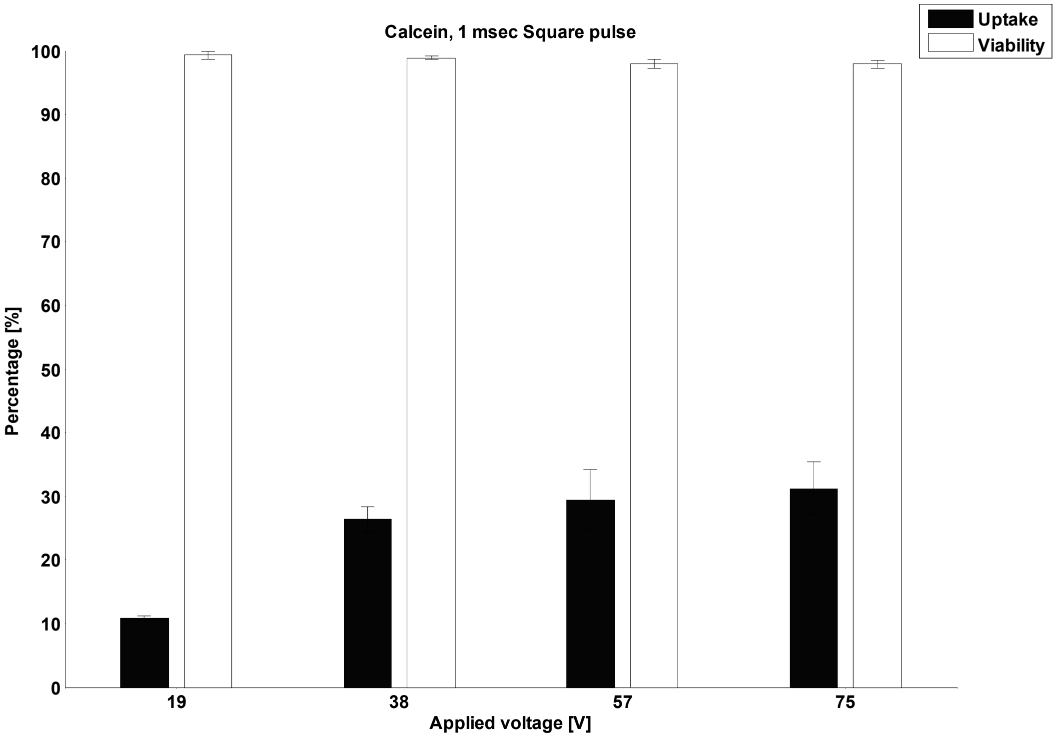

Figure 5.9 Uptake and viability for a 1 ms square pulse

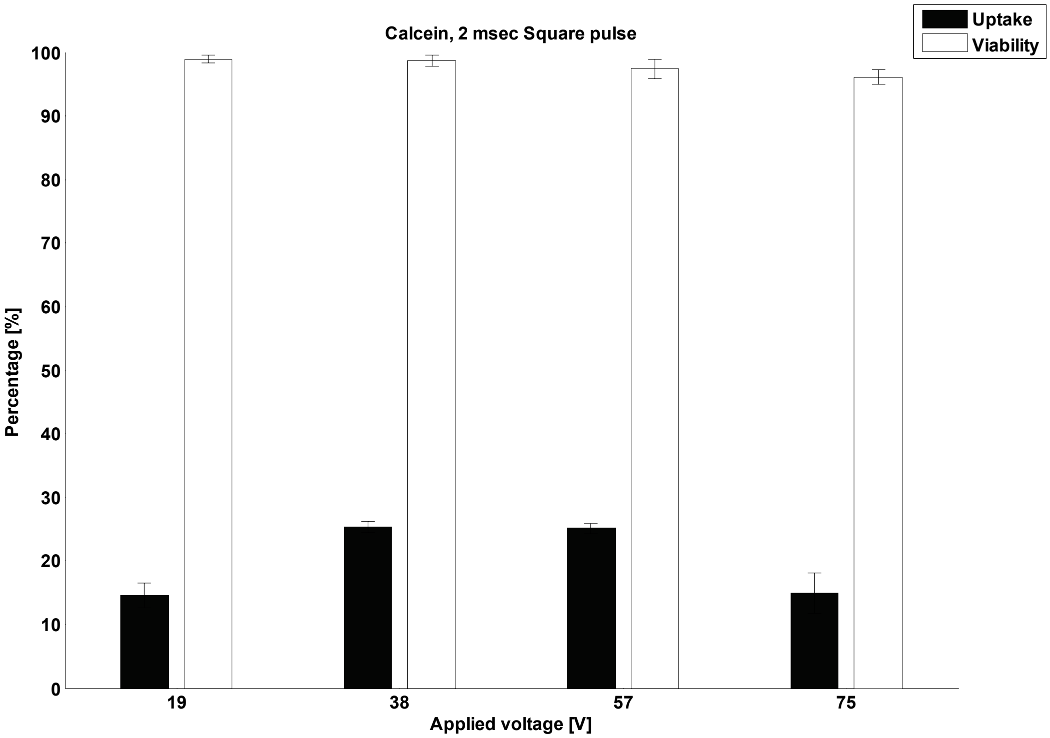

Figure 5.10 Uptake and viability for a 2 ms square pulse

Using 0.5 and 1 ms pulses, the uptake of calcein increased as the applied voltage increased. For the 2 ms pulse, the maximum uptake seemed to occur between 38 V and 57 V. These results suggest that pulse length plays an important role in delivering molecules into cells by electroporation. If we recall Schwann's equation, the induced transmembrane voltage is dependent on the angle between the applied field and the cell membrane, and aqueous pores are created on the cell membrane when the induced transmembrane voltage exceeds a certain value. The number of pores created on the cell membrane is completely dependent on the applied field strength; therefore, there is a high chance for molecules to get into the cell membrane when the applied field strength is high enough. However, if the applied field strength is too high, some pores can not be resealed after pulsation, causing cell death. It is thought that the size of pore is dependent on the applied field strength and if the pores are too big, a cell loses its ability to reseal its membrane. Once pores are formed by an external electric field, molecules which are impermeable to an intact cell membrane can be transported into the cell through the pores by mechanisms such as osmosis and electrophoresis. During the transport phase, pulse length will contribute to electrophoresis and longer pulses can transport more molecules into a cell. The effect of pulse length on calcein uptake was well studied by Canatella et al. [129]. Viability is also strongly dependent on pulse length, indicating that both applied field strength and the duration of a pulse should be considered for effective transport of molecules into a cell by electroporation.

Figure 5.11 summarizes the effect of pulse length on calcein uptake. It was found that the percentage of uptake increased as the pulse length increased at relatively low voltages, below 40 V. However, shorter pulses showed higher uptake at relatively high voltages, above 60 V. The results suggest that the range for effective delivery of molecules is dependent on the applied pulse length. For a shorter pulse, the range of applied voltages for effective delivery of molecules with high viability is wider than the voltage range for a longer pulse. If we compare the relative field strengths, a shorter pulse needs higher field strength than a longer pulse to reach the maximum uptake. However, the maximum uptake induced by a shorter pulse was higher than the uptake induced by a longer pulse.

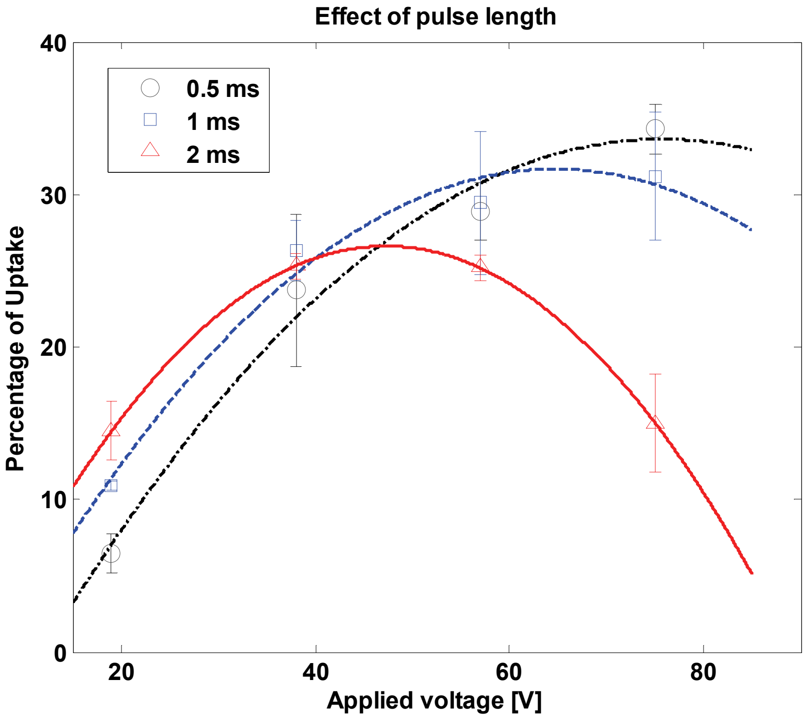

Figure 5.11 The effect of pulse length on calcein uptake

5.3.2 Bovine Serum Albumin (BSA) Delivery Experiment

Since the ultimate goal of the electroporation microneedle is to deliver large molecules such as DNA through the skin, it is desirable to show its ability to deliver large molecules into cells. Therefore, fluorescein-tagged bovine serum albumin (BSA), which has a molecular weight of 68 kDa, was chosen as a model molecule. For electroporation, both exponential and square pulses were used. The concentration of BSA was 2.5×10-5 M. As described above, DU145 human prostate cancer cells with a concentration of 2.5 million cells per ml were used. The experimental protocol was similar to that of calcein delivery experiment, described previously. To remove the extracellular BSA remaining in suspension after electroporation, the cells were re-suspended in 200 μl of PBS which as then centrifuged. Since BSA tends to adhere to the cell membrane, 0.1 % trypsin was used to wash cells after PBS washing. Cell washing with trypsin was done twice, and then the cells were further washed by PBS alone twice.

5.3.2.1 BSA Delivery Using Exponential Pulse

Using the BTX pulse generator, a 2.5 ms exponential pulse was applied to the microneedle array. 6 μl of cell suspension was used for the experiment, and a total of 60 μl of cell suspension was collected in a micro-centrifuge tube by performing 10 experiments for each experimental condition. From the 60 μl sample, 6 μl was used for taking confocal microscopic images, and the remaining 54 μl was diluted in 200 μl PBS for flow cytometry. A total of 7 different voltages were applied for the experiment, and the representative images from the confocal microscope are shown in Figure 5.12.

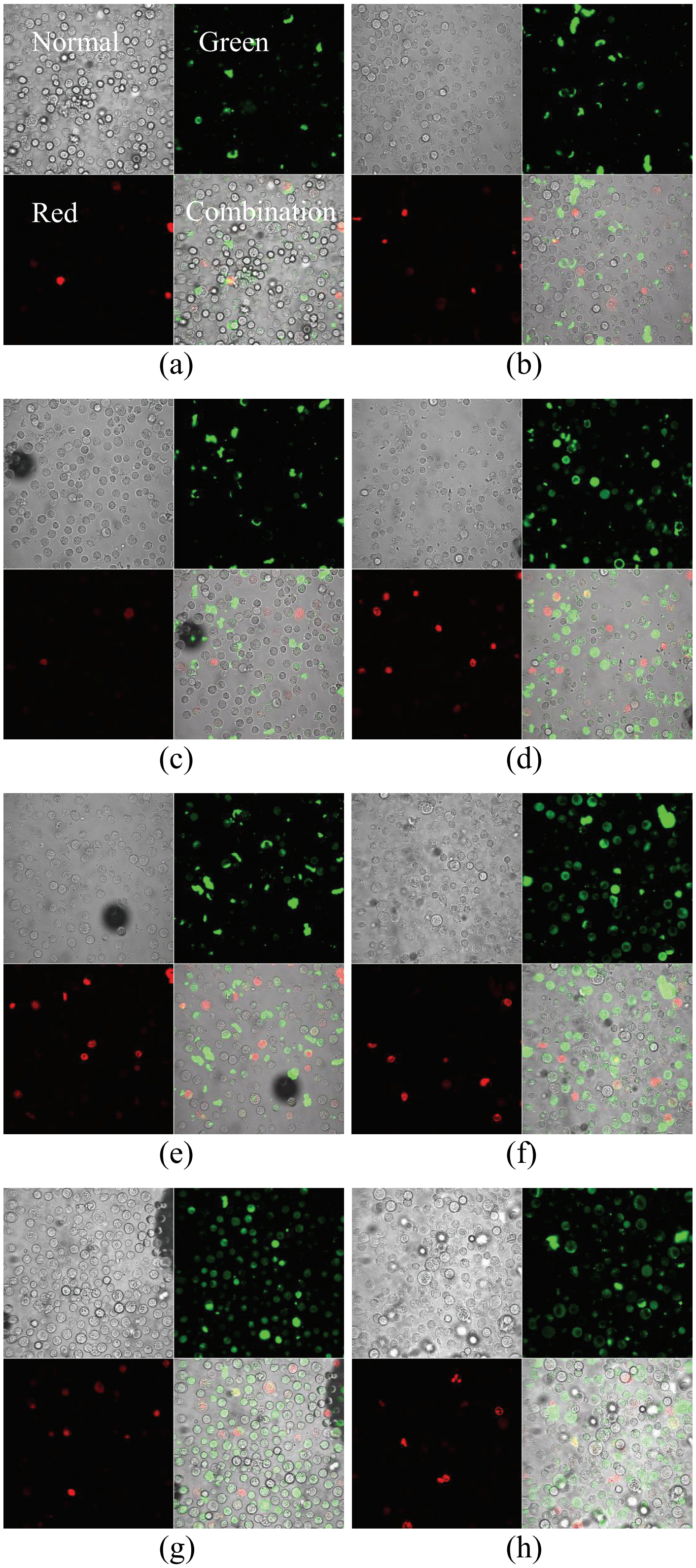

(a) (b) (c) (d) (e) (f) (g) (h)

Figure 5.12 Confocal microscopic images of the human prostate cancer cell after delivering BSA; (a) control, (b) 14 V, (c) 28 V, (d) 42 V, (e) 56 V, (f) 75 V, (g) 86 V, and (h) 96 V, respectively

In the confocal microscopic images it was apparent that residual BSA was still found on cell membranes after washing with PBS and trypsin. However, it was found that the trypsin-mediated washing protocol helped remove BSA from the cell membrane compared to washing the cells with PBS only. Due to the residual BSA on the cell membrane, green fluorescence was detected in the control sample during flow cytometric analyses. To remove this artifact, the percentage of uptake in the control samples, which was due to the surface BSA, was substracted from the percentage of uptake in each electroporated sample. Figure 5.13 shows BSA uptake and viability for each experimental condition. In addition, uptake and viability were estimated from the model of electric field strength distribution using the same window as that used for the calcein delivery model shown in Figure 5.13. An uptake efficiency of 30 % was used, and the overall trend of the predicted uptake was similar to that of the experimental results. According to the model, uptake increased as the applied voltage increased, and the highest uptake was predicted at 56 V. After 56 V, uptake started to decrease, which was consistent with the experimental results.

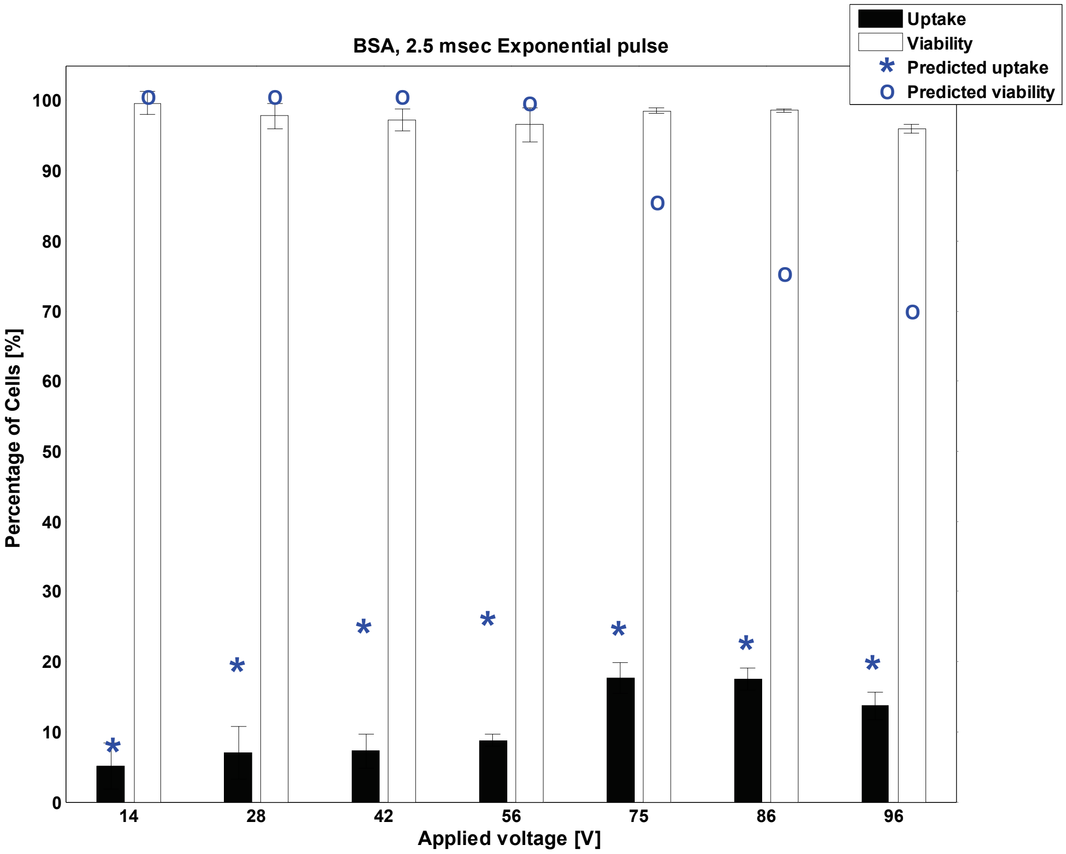

Figure 5.13 BSA uptake and viability using a 2.5 ms exponential pulse

Compared to calcein delivery experiments performed at the same pulse length, the amount of uptake was reduced. This indicates that it is more difficult to deliver large molecules across the cell membrane. Statistically, it was determined that the uptake rates for the first 4 conditions were not different. Also the last 3 conditions showed the same percentage of uptake statistically (Student's t-test, $p<0.05$). This may be due to the limitation in transporting large molecules by diffusion and the dependency of the size of pores on the external field strength. However, further investigation is required to prove this hypothesis, and it is beyond the scope of this study.

5.3.2.2 BSA Delivery Using Square Pulse

BSA delivery was also attempted by applying a square pulse using the square pulse generator (Pulse Agile, Cyto Pulse Sciences, Inc., MD, USA). For the experiment, a 2 ms single square pulse was applied at four different voltages ranging from 20 V to 80 V. As described before, the actual voltage applied was recorded by an oscilloscope, and the actual values from the oscilloscope were: 19 V, 38 V, 57 V, and 75 V, respectively. The experimental protocol was the same as the experiment with exponential pulse, and the results are shown in Figure 5.14.

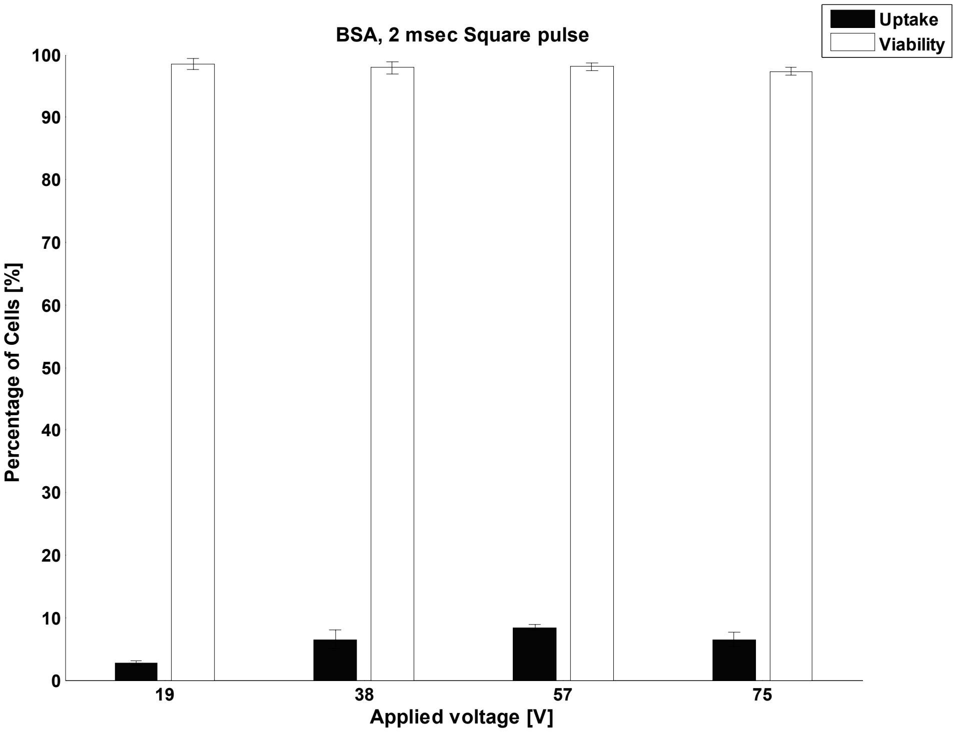

Figure 5.14 BSA uptake and viability using a 2 ms square pulse

The experimental results of BSA uptake by the application of square pulse were similar to the results of those obtained with the exponential pulse. The percentage of uptake at each condition was not statistically different (Student's t-test, p<0.05), except at first condition. Using a 2.5 ms exponential pulse, the percentage of uptake increased at 75 V. With a 2 ms square pulse, however, this increase was not observed. As discussed previously, pulse length is associated with the molecular transporting mechanism. Typically, short pulses require higher field strengths for transporting molecules than longer pulses require. This observation possibly explains why increased cellular uptake did not occur at 75 V.

5.4 Conclusion

Electroporation experiments with the fabricated microneedle arrays were performed. The hemoglobin release experiment confirmed that fabricated microneedle arrays were electrically functional and could lyse red blood cells. Although the electric field generated by the microneedle array was inherently inhomogeneous, up to approximately 50 % of cells had uptake of calcein while maintaining high viability (over 85 %). These results demonstrate that microneedle arrays can effectively deliver small molecules by means of electroporation. BSA, a large molecule, could also be transported across the cell membrane using the microneedle arrays; however, transport efficiency of BSA was lower than that of calcein. The efficiency of delivering large molecules may be improved by optimizing parameters such as pulse length.

CHAPTER 6

CONCLUSIONS

6.1 Summary

The ultimate goal of this research was to develop a micro-scale electroporation device that can deliver molecules into skin cells. To achieve this goal, the device should have two functionalities: 1) mechanical functionality to overcome the stratum corneum, the outermost layer of skin, which presents the largest barrier to drug transport; and 2) electrical functionality to generate an electric field required for electroporation. Those goals were successfully implemented in a single device by adding electrical functionality to a microneedle array.

Micromolding techniques were exploited to fabricate the microneedle arrays, thereby using a fabrication process is suitable for cost-effective mass production. PDMS was selected as the mold material, and different materials such as PMMA, PU, SU-8, and PLA were successfully cast using the PDMS mold to create functional microneedle arrays. Even highly viscous materials, such as molten PLA, were able to achieve sharp microneedle tips by using vacuum.

Inclined/rotational UV lithography was utilized to fabricate a negative of the microneedle array. The advantage of this approach is that it does not require a dry or wet etching process, which is necessary for conventional approaches, to form a sharp tip. Also, other geometrical parameters such as shape and height of the microneedle, tip angle, and spacing between microneedles can be easily controlled by changing the mask footprints or incident angle of the UV light. Combined with micromolding techniques, this approach can produce 3-D microstructures of varying heights from a single mask. A microneedle array composed of microneedles with different heights can thus be formed. Extending this technique with proper masks and further fabrication steps would make it possible to fabricate complex 3-D microstructures that would be nearly impossible using conventional approaches.

Laser ablation and metal transfer micromolding were investigated as methods for implementing electrical functionality to the microneedle array. An excimer laser was used to pattern a thin layer of metal (~3000 Å) deposited on the microneedle array. By optimizing ablation parameters such as energy density, scribing speed, and number of pulses, the metal layer was clearly patterned without generating cracks around the patterns. Laser ablation is a serial process, and may not be suitable for mass production; however, it is valuable for prototyping because any changes in design can be easily made by modifying the design file in situ.

A double-layer micromold approach was developed to pattern a metal layer on a 3-D microstructure by combining metal transfer techniques and micromolding. Since this approach does not require any photolithography steps for patterning the metal layer, difficulties associated with the metallization of 3-D microstructures using photolithography can be avoided. Therefore, this approach is suitable for generating metal patterns on a substrate which contains high-aspect-ratio structures, such as metallized microneedles.

Fabricated microneedle arrays should be mechanically strong enough to penetrate skin; therefore, insertion tests with human and pig skin were performed. It was shown that the polymeric microneedle array with a thin metal layer (~3000 Å) could not penetrate skin without tip breakage. To solve this problem, Ni was electroplated onto the microneedle array to enhance the rigidity. The thickness of the Ni layer required for safe insertion varied with the materials and the geometry of the microneedle array. It was shown that as the thickness of Ni increases, the mechanical strength of the structure increases. However, the insertion force required to penetrate skin also increases as a function of the expansion of the tip diameter of the microneedle due to the Ni layer. This suggests that the optimal thickness of an electroplated metal layer should be determined by considering both enhancement of the mechanical rigidity and acceptability of the required insertion force due to the thickened metal layer.

A series of 2-D finite element (FE) models was used to determine the distribution of electric field strength generated by the fabricated microneedle arrays. A spatial distribution of electric field strength was constructed by interpolating the 2-D models, which represent cross-sections of a microneedle array at specfic heights. An analytical expression of the distribution was derived by fitting the distribution with Gaussian functions. The effective volume for electroporation could be estimated from the analytical model within a specific range of electric field strength.

To verify the electrical functionality of the microneedle arrays, hemoglobin release from bovine red blood cells and the delivery of calcein and bovine serum albumin into DU145 human prostate cancer cells were performed *in vitro*. By these experiments, it was shown that the fabricated microneedle array could cause electrical permeation of cells, or electroporation. Furthermore, it was seen that aqueous pores on the intact cell membrane were created, allowing the transport of both small molecules, calcein, and large proteins, BSA, into cells via electroporation.

Since the fabricated microneedle array generates an inhomogeneous electric field, the efficiency of electroporation using this device can not exceed that of a cuvette in which parallel electrodes are embedded for generating a homogeneous electric field. The advantage of the fabricated microneedle array over the cuvette is that the same electric field strength can be generated by a lower applied voltage, due to the smaller gap between the electrodes, e.g. microneedles. No uptake of calcein was observed at an applied voltage of 50 V with the cuvette, which has a 2 mm gap between electrodes; however, the microneedle array caused approximately 40 % of the cells to have uptake at the same condition. This result implies that the fabricated microneedle array requires a lower voltage for electroporation to occur than a conventional caliper-type skin electroporation device. When compared to electroporation devices that use hypodermic needles as electrodes, the fabricated microneedle array can reduce pain during insertion, as well as lower the voltage required for electroporation. A third type of skin electroporation device, surface electrodes, is capable of alleviating pain during the application of an electric field by confining most of the electric field to the stratum corneum. However, this approach requires initial administration of a drug by either injection with a hypodermic needle, which causes pain, or by disrupting the stratum corneum with a high electric field, which can cause burning.

An insertion test of the microneedle array into *in vivo* human skin pain indicated that no pain was felt by the subject during the insertion. It was also shown that the arrays can electroporate cells at lower voltages than those required for conventional cuvettes.

Overall, fabricated microneedle arrays are a better option for electroporation treatment than conventional electroporation devices in terms of pain reduction and low voltage requirements due to the much smaller scale. In conclusion, it was demonstrated that electroporation using a microneedle array device may be a promising method for delivery of molecules into skin.

6.2 Suggestions for Future Work

It was demonstrated that inclined UV lithography combined with a micromolding technique was useful for fabricating 3-D microstructures. The combination of inclined/rotational UV lithography and metal transfer micromolding showed that 3-D metal-patterned polymeric microstructures can be created. By extending these newly developed technologies, it would be possible to fabricate much more complex 3-D microstructures, including an implantable microelectrode array.

For biomedical applications, material selection is very important. For implantable devices, biocompatibility of the material is critical. The fabrication processes should be tailored based on the material selection. Although Ni was used in this study and did not show cytotoxicity to DU145 cells, Ni can cause skin irritation. Therefore, other materials such as Au or Pt, which are more biocompatible and also compatible with microfabrication techniques such as electroplating, would be desirable for *in vivo* experiments.

The original goal of the fabricated microneedle arrays was to deliver DNA vaccines across the skin and into appropriate cells. These devices demonstrated the ability to create pathways for molecular transport *in vitro*. However, DNA transfection experiments *in* *vivo* still need to be performed. One of the main issues associated with completing an *in vivo* study is determining how to inject the target molecules into the skin. There are two potential approaches: 1) coating the target molecules on the microneedle array; or 2) forming holes (hollow microneedle array) through which the molecules can be injected into the skin.

For efficacious electroporation, a homogeneous distribution of an electric field is desirable. Although the microneedle array cannot avoid inhomogeneity of electric field distribution, the heterogeneity may be able to be minimized by considering the geometry of the microneedles and the configuration of the electrodes. Therefore, the optimization of design parameters with finite element simulation is highly recommended for future studies.

REFERENCES

[1] D. V. McAllister, P. M. Wang, S. P. Davis, J.-H. Park, P. J. Canatella, M. G. Allen, and M. R. Prausnitz, "Microfabricated needles for transdermal delivery of macromolecules and nanoparticles: Fabrication methods and transport studies," *Proceedings of the National Academy of Sciences of the United States of America,* vol. 100, pp. 13755-13760, 2003.

[2] M. R. Prausnitz, "Microneedles for transdermal drug delivery," *Advanced Drug Delivery Reviews,* vol. 56, pp. 581-587, 2004.

[3] H. H. Huang, J. Zhou, Y. P. Huang, and J. L. Kong, "A novel multichannel immunosensor for determination of serum hepatic fibrosis markers," *Sensors and Materials,* vol. 18, pp. 445-456, 2006.

[4] S. Iguchi, H. Kudo, T. Saito, M. Ogawa, H. Saito, K. Otsuka, A. Funakubo, and K. Mitsubayashi, "A flexible and wearable biosensor for tear glucose measurement," *Biomedical Microdevices,* vol. 9, pp. 603-609, 2007.

[5] H. Kudo, T. Sawada, E. Kazawa, H. Yoshida, Y. Iwasaki, and K. Mitsubayashi, "A flexible and wearable glucose sensor based on functional polymers with soft-MEMS techniques," *Biosensors & Bioelectronics,* vol. 22, pp. 558-562, 2006.

[6] J. Pepper, R. Noring, M. Klempner, B. Cunningham, A. Petrovich, R. Bousquet, C. Clapp, J. Brady, and B. Hugh, "Detection of proteins and intact microorganisms using microfabricated flexural plate silicon resonator arrays," *Sensors and Actuators B-Chemical,* vol. 96, pp. 565-575, 2003.

[7] Z. A. Strong, A. W. Wang, and C. F. McConaghy, "Hydrogel-actuated capacitive transducer for wireless biosensors," *Biomedical Microdevices,* vol. 4, pp. 97-103, 2002.

[8] H. H. Weetall, "Chemical sensors and biosensors, update, what, where, when and how," *Biosensors & Bioelectronics,* vol. 14, pp. 237-242, 1999.

[9] S. K. Yoo, J. H. Lee, S. S. Yun, M. B. Gu, and J. H. Lee, "Fabrication of a bio-MEMS based cell-chip for toxicity monitoring," *Biosensors & Bioelectronics,* vol. 22, pp. 1586-1592, 2007.

[10] H. Y. Tseng, C. H. Wang, W. Y. Lin, and G. B. Lee, "Membrane-activated microfluidic rotary devices for pumping and mixing," *Biomedical Microdevices,* vol. 9, pp. 545-554, 2007.

[11] J. S. Park, K. B. Park, K. S. Shin, H. D. Park, M. C. Kim, J. R. Kim, S. J. Park, and Y. H. Song, "Design, fabrication and characterization of an integrated micro ammonia analysis system (IMAAS) with microreactor and in-plane type optical detector based on the Berthelot reaction," *Sensors and Actuators B-Chemical,* vol. 117, pp. 516-522, 2006.

[12] Z. Q. Zou, X. Chen, Q. H. Jin, M. S. Yang, and J. L. Zhao, "A novel miniaturized PCR multi-reactor array fabricated using flip-chip bonding techniques," *Journal of Micromechanics and Microengineering,* vol. 15, pp. 1476-1481, 2005.

[13] C. Y. Shih, Y. Chen, W. Li, J. Xie, Q. He, and Y. C. Tai, "An integrated system for on-chip temperature gradient interaction chromatography," *Sensors and Actuators A-Physical,* vol. 127, pp. 207-215, 2006.

[14] J. H. Min and A. Baeumner, "The micro-total analytical system for the detection of bacteria/viruses," *Journal of Industrial and Engineering Chemistry,* vol. 9, pp. 1-8, 2003.

[15] M. Mojarradi, D. Binkley, B. Blalock, R. Andersen, N. Ulshoefer, T. Johnson, and L. Del Castillo, "A miniaturized neuroprosthesis suitable for implantation into the brain," *IEEE Transactions on Neural Systems and Rehabilitation Engineering,* vol. 11, pp. 38-42, 2003.

[16] J. Muthuswamy, M. Okandan, A. Gilletti, M. S. Baker, and T. Jain, "An array of microactuated microelectrodes for monitoring single-neuronal activity in rodents," *IEEE Transactions on Biomedical Engineering,* vol. 52, pp. 1470-1477, 2005.

[17] S. Snow, S. C. Jacobsen, D. L. Wells, and K. W. Horch, "Microfabricated cylindrical multielectrodes for neural stimulation," *IEEE Transactions on Biomedical Engineering,* vol. 53, pp. 320-326, 2006.

[18] P. T. Bhatti and K. D. Wise, "A 32-site 4-channel high-density electrode array for a cochlear prosthesis," *IEEE Journal of Solid-State Circuits,* vol. 41, pp. 2965-2973, 2006.

[19] H. Zhang, D. W. Hutmacher, F. Chollet, A. N. Poo, and E. Burdet, "Microrobotics and MEMS-based fabrication techniques for scaffold-based tissue engineering," *Macromolecular Bioscience,* vol. 5, pp. 477-489, 2005.

[20] G. J. Wang, C. L. Chen, S. H. Hsu, and Y. L. Chiang, "Bio-MEMS fabricated artificial capillaries for tissue engineering," *Microsystem Technologies,* vol. 12, pp. 120-127, 2005.

[21] K. M. Kulig and J. R. Vacanti, "Hepatic tissue engineering," *Transplant Immunology,* vol. 12, pp. 303-310, 2004.

[22] R. S. Shawgo, A. C. R. Grayson, Y. W. Li, and M. J. Cima, "BioMEMS for drug delivery," *Current Opinion in Solid State & Materials Science,* vol. 6, pp. 329-334, 2002.

[23] A. C. R. Grayson, R. S. Shawgo, Y. W. Li, and M. J. Cima, "Electronic MEMS for triggered delivery," *Advanced Drug Delivery Reviews,* vol. 56, pp. 173-184, 2004.

[24] Y. W. Li, R. S. Shawgo, B. Tyler, P. T. Henderson, J. S. Vogel, A. Rosenberg, P. B. Storm, R. Langer, H. Brem, and M. J. Cima, "In vivo release from a drug delivery MEMS device," *Journal of Controlled Release,* vol. 100, pp. 211-219, 2004.

[25] A. Arora, I. Hakim, J. Baxter, R. Rathnasingham, R. Srinivasan, D. A. Fletcher, and S. Mitragotri, "Needle-free delivery of macromolecules across the skin by nanoliter-volume pulsed microjets," *Proceedings of the National Academy of Sciences of the United States of America,* vol. 104, pp. 4255-4260, 2007.

[26] J. D. Boss, *Skin Immune System*, CRC Press, 1997.

[27] http://www.essentialdayspa.com/Skin_Anathomy_and_Physiology.htm.

[28] U. R. Hengge, P. S. Walker, and J. C. Vogel, "Expression of naked DNA in human, pig, and mouse skin," *The Journal of clinical investigation*, vol. 97, pp. 2911-2916, 1996.

[29] L. Cheng, P. R. Ziegelhoffer, and N. S. Yang, "In vivo promoter activity and transgene expression in mammalian somatic tissues evaluated by using particle

bombardment," *Proceedings of the National Academy of Sciences of the United States of America,* vol. 90, pp. 4455-4459, 1993.

[30] D. Sawamura, S. Ina, K. Itai, X. Meng, A. Kon, K. Tamai, K. Hanada, and I. Hashimoto, "In vivo gene introduction into keratinocytes using jet injection," *Gene Theraphy,* vol. 6, pp. 1785-1787, 1999.

[31] I. F. Ciernik, B. H. Krayenbuhl, and D. P. Carbone, "Puncture-mediated gene transfer to the skin," *Human Gene Theraphy,* vol. 7, pp. 893-899, 1996.

[32] W. H. Yu, M. Kashani-Sabet, D. Liggitt, D. Moore, T. D. Heath, and R. J. Debs, "Topical gene delivery to murine skin," *Journal of Investigative Dermatology,* vol. 112, pp.370-375, 1999.

[33] B. Lu, H. Federoff, Y. Wang, L. Goldsmith, and G. Scott, "Topical applications of viral vectors for epidermal gene transfer," *Journal of Investigative Dermatology,* vol. 108, pp. 803-808, 1997.

[34] L. Li and R. M. Hoffman, "The feasibility of targeted selective gene therapy of the hair follicle," *Nature Medicine,* vol. 1, pp. 705-706, 1995.

[35] B. M. Medi, S. Hoselton, R. B. Marepalli, and J. Singh, "Skin targeted DNA vaccine delivery using electroporation in rabbits I: Efficacy," *International Journal of Pharmaceutics,* vol. 294, pp. 53-63, 2005.

[36] L. Zhang, E. Nolan, S. Kreitschitz, and D. P. Rabussay, "Enhanced delivery of naked DNA to the skin by non-invasive in vivo electroporation," *Biochimica Et Biophysica Acta,* vol. 1572, pp. 1-9, 2002.

[37] C. C. Norbury, D. Malide, J. S. Gibbs, J. R. Bennink, and J. W. Yewdell, "Visualizing priming of virus-specific CD8+ T cells by infected dendritic cells in vivo," *Nature Immunology,* vol. 3, pp. 265-271, 2002.

[38] R. Stampfli, "Reversible electrical breakdown of the excitable membrane of a ranvier node," *Anais da Academia Brasileira de Ciencias,* vol. 30, pp. 57-63, 1958.

[39] A. Sale and W. Hamilton, "Effects of high electric fields on microorganisms: I. Killing of bacteria and yeasts," *Biochimica Et Biophysica Acta,* vol. 148, pp. 781-788, 1967.

[40] E. Neumann and K. Rosenheck, "Permeability changes induced by electric impulses in visicular membranes," *The Journal of Membrane Biology,* vol. 10, pp. 279-290, 1972.

[41] L. V. Chernomordik, *Electropores in lipid biliayers and cell membranes*, Academic Press, 1992.

[42] J. C. Weaver, "Electroporation: a general phenomenon for manipulating cells and tissues," *Journal of Cellular Biochemistry,* vol. 51, pp. 426-435, 1993.

[43] D. Miklavcic and T. Kotnik, "Electroporation for electrochemotherapy and gene therapy," in *Bioelectromagnetic Medicine*, pp. 637-656, 2004.

[44] L. M. Mir, H. Banoun, and C. Paoletti, "Introduction of definite amounts of nonpermeant molecules into living cells after electropermeabilization: direct access to the cytosol*," Experimental Cell Research,* vol. 175, pp. 15-25, 1988.

[45] J. E. Dinchuck, K. A. Kelley, and G. N. Callahan, "Flow cytometric analysis of transport activity in lymphocytes electroporated with a fluorescent organic anion dye," *Journal of Immunological Methods,* vol. 155, pp. 257-265, 1992.

[46] J. Gehl, T. Skovsgaard, and L. M. Mir, "Enhancement of cytotoxicity by electropermeabilization: an improved method for screening drugs," *Anticancer Drugs,* vol. 9, pp. 319-325, 1998.

[47] P. E. Engstrom, B. R. Persson, and L. G. Salford, "Studies of in vivo electropermeabilization by gamma camera measurements of (99m)Tc-DTPA," *Biochimica Et Biophysica Acta,* vol. 1473, pp. 321-328, 1999.

[48] J. Gehl, T. H. Sørensen, K. Nielesen, P. Raskmart, S. L. Nielsen, T. Skovsgaard, and L. M. Mir, "In vivo electroporation of skeletal muscle: threshold, efficacy and relation to electric field distribution," *Biochimica Et Biophysica Acta,* vol. 1428, pp. 233-240, 1999.

[49] J. J. Belehradek, S. Orlowski, L. H. Ramirez, G. Pron, B. Poddevin, and L. M. Mir, "Electropermeabilization of cells in tissues assessed by the qualitative and quantitative electroloading of bleomycin," *Biochimica Et Biophysica Acta,* vol. 1190, pp. 155-163, 1994.

[50] G. Sersa, M. Cemazar, and D. Miklavcic, "Antitumor effectiveness of electrochemotherapy with *cis*-diamminedichloroplatinum(II) in mice," *Cancer Research,* vol. 55, pp. 3450-3455, 1995.

[51] M. J. Jaroszeski, V. Dang, C. Pottinger, J. Hickey, R. Gilbert, and R. Heller, "Toxicity of anticancer agents mediated by electroporation in vitro," *Anticancer Drugs,* vol. 11, pp. 201-208, 2000.

[52] D. G. Spiller, R. V. Giles, J. Grzybowski, D. M. Tidd, and R. E. Clark, "Improving the intracellular delivery and molecular efficacy of antisense oligonucleotides in chronic myeloid leukemia cells: a comparison of streptolysin-O permeabilization, electroporation, and lipophilic conjugation," *Blood,* vol. 91, pp. 4738-4746, 1998.

[53] M. N. Teruel, T. A. Blanpied, K. Shen, G. J. Augustine, and T. Meyer, "A versatile microporation technique for the tranfection of cultured CNS neurons," *Journal of Neuroscience Methods,* vol. 93, pp. 37-48, 1999.

[54] S. Saeboe-Larssen, E. Fossberg, and G. Gaudernack, "mRNA-based electrotransfection of human dendritic cells and induction of cytotoxic T lymphocyte responses against the telomerase catalytic subunit (hTERT)," *Journal of Immunological Methods,* vol. 259, pp. 191-203, 2002.

[55] E. Neumann, M. Schaefer-Ridder, Y. Wang, and P. H. Hofschneider, "Gene transfer into mouse lyoma cells by electroporation in high electric fields," *The EMBO Journal,* vol. 1, pp. 841-845, 1982.

[56] R. Heller, M. J. Jaroszeski, and A. Atkin, "In vivo gene electroinjection and expression in rat liver," *FEBS Letter,* vol. 389, pp. 225-228, 1996.

[57] M. P. Rols, C. Delteil, M. Golzio, P. Dumond, S. Cros, and J. Teissie, "In vivo electrically mediated protein and gene transfer in murine melanoma," *Nature Biotechnology,* vol. 16, pp. 168-171, 1998.

[58] L. M. Mir, M. F. Bureau, and J. Gehl, "High efficiency gene transfer into skeletal muscle mediated by electric pulses," *Proceedings of the National Academy of Sciences of the United States of America,* vol. 96, pp. 4262-4267, 1999.

[59] S. B. Dev and G. A. Hofmann, "Electrochemotherapy-A novel method of cancer treatment," *Cancer Treatment Reviews,* vol. 20, pp. 105-115, 1994.

[60] G. A. Hofmann, S. B. Dev, and G. S. Nanda, "Electrochemotherapy: Transition from laboratory to the clinic," *IEEE Engineering in Medicine and Biology Magazine,* vol. 15, pp. 124-132, 1996.

[61] G. A. Hofmann, W. V. Rustrum, and K. S. Suder, "Electro-incorporation of microcarriers as a method for the transdermal delivery of large molecules," *Bioelectrochemistry and Bioenergetics,* vol. 38, pp. 209-222, 1995.

[62] T. Nishi, K. Yoshizato, S. Yamashiro, H. Takeshima, K. Sato, K. Hamada, I. Kitamura, T. Yoshimura, H. Saya, J. Kuratsu, and Y. Ushio, "High efficiency in vivo gene transfer using intra arterial plasmid DNA injection following in vivo electroporation," *Cancer Research,* vol. 56, pp. 1050-1055, 1996.

[63] K. Kinosita and T. Y. Tsong, "Voltage-induced pore formation and hemolysis of human erythrocytes," *Biochimica Et Biophysica Acta,* vol. 471, pp. 227-242, 1977.

[64] J. Teissie and M. P. Rols, "An experimental evaluation of the critical potential difference inducing cell membrane electropermeabilization," *Biophysical Journal,* vol. 65, pp. 409-413, 1993.

[65] S. B. Dev, D. P. Rabussay, G. Widera, and G. A. Hofmann, "Medical applications of electroporation," *IEEE Transactions on Plasma Science,* vol. 28, pp. 206-223, 2000.

[66] H. P. Schwan, "Electrical properties of tissue and cell suspensions," *Advances in Biological and Medical Physics*, vol. 5, pp. 147-209, 1957.

[67] T. Kotnik, F. Bobanović, and D. Miklavčič, "Sensitivity of transmembrane voltage induced by applied electric fields-a theoretical analysis," *Bioelectrochemistry and Bioenergetics,* vol. 43, pp. 285-291, 1997.

[68] T. Kotnik and D. Miklavčič, "Analytical description of transmembrane voltage induced by electric fields on spheroidal cells," *Biophysical Journal,* vol. 79, pp. 670-679, 2000.

[69] G. A. Hofmann, S. B. Dev, S. Dimmer, and G. S. Nanda, "Electroporation therapy: A new approach for the treatment of head and neck cancer," *IEEE Transactions on Biomedical Engineering,* vol. 46, pp. 752-759, 1999.

[70] M. S. Gerstel and V. A. Place, "Drug delivery device," in *United States Patent* 3,964,482, 1976.

[71] S. Hashmi, P. Ling, G. Hashmi, M. Reed, R. Gaugler, and W. Trimmer, "Genetic transformation of nematodes using arrays of micromechanical piercing structures," *Biotechniques,* vol. 19, pp. 766-770, 1995.

[72] S. Henry, D. V. McAllister, M. G. Allen, and M. R. Prausnitz, "Microfabricated microneedles: A novel approach to transdermal drug delivery," *Journal of Pharmaceutical Sciences,* vol. 87, pp. 922-925, 1998.

[73] J. A. Mikszta, J. B. Alarcon, J. M. Brittingham, D. E. Sutter, R. J. Pettis, and N. G. Harvey, "Improved genetic immunization via micromechanical disruption of skin-barrier function and targeted epidermal delivery," *Nature Medicine,* vol. 8, pp. 415-419, 2002.

[74] P. Griss, P. Enoksson, H. K. Tolvanen-Laakso, P. Meriläinen, S. Ollmar, and G. Stemme, "Micromachined electrodes for biopotential measurements," *Journal of Microelectromechanical Systems,* vol. 10, pp. 10-16, 2001.

[75] M. Shikida, M. Ando, Y. Ishihara, T. Ando, K. Sato, and K. Asaumi, "Non-photolithographic pattern transfer for fabricating pen-shaped microneedle structures," *Journal of Micromechanics and Microengineering,* vol. 14, pp. 1462-1467, 2004.

[76] J. A. Matriano, M. Cormier, J. Johnson, W. A. Young, M. Buttery, K. Nyam, and P. E. Daddona, "Microflux® microprojection array patch technology: a new and efficient approach for intracutaneous immunization," *Pharmceutical Research,* vol. 19, pp. 63-70, 2002.

[77] M. Cormier, B. Johnson, M. Ameri, K. Nyam, L. Libiran, D. D. Zhang, and P. Daddona, "Transdermal delivery of desmopressin using a coated microneedle array patch system," *Journal of Controlled Release,* vol. 97, pp. 503-511, 2004.

[78] W. Martanto, S. P. Davis, N. R. Holliday, J. Wang, H. S. Gill, and M. R. Prausnitz, "Transdermal delivery of insulin using microneedles in vivo," *Pharmceutical Research,* vol. 21, pp. 947-952, 2004.

[79] J.-H. Park, M. G. Allen, and M. R. Prausnitz, "Biodegradable polymer microneedles: fabrication, mechanics and transdermal drug delivery," *Journal of Controlled Release,* vol. 104, pp. 51-66, 2005.

[80] J. Brazzle, I. Papautsky, and A. B. Frazier, "Micromachined needle arrays for drug delivery or fluid extraction," *IEEE Engineering in Medicine and Biology Magazine,* vol. 18, pp. 53-58, 1999.

[81] L. Lin and A. P. Pisano, "Silicon-processed microneedles," *Journal of Microelectromechanical Systems,* vol. 8, pp. 78-84, 1999.

[82] S. Chandrasekaran, J. D. Brazzle, and A. B. Frazier, "Surface micromachined metallic microneedles," *Journal of Microelectromechanical Systems,* vol. 12, pp. 281-288, 2003.

[83] H. J. G. E. Gardeniers, R. Luttge, E. J. W. Berenschot, M. J. d. Boer, S. Y. Yeshurun, M. Hefetz, R. v. t. Oever, and A. v. d. Berg, "Silicon micromachined hollow microneedles for transdermal liquid transport," *Journal of Microelectromechanical Systems,* vol. 12, pp. 855-862, 2003.

[84] P. Griss and G. Stemme, "Side-opened out-of-plane microneedles for microfluidic transdermal liquid transfer," *Journal of Microelectromechanical Systems,* vol. 12, pp. 296-301, 2003.

[85] N. Roxhed, P. Griss, and G. Stemme, "A method for tapered deep reactive ion etching using a modified Bosch process," *Journal of Micromechanics and Microengineering,* vol. 17, pp. 1087-1092, 2007.

[86] E. V. Mukerjee, S. D. Collins, R. R. Isseroff, and R. L. Smith, "Microneedle array for transdermal biological fluid extraction and in situ analysis," *Sensors and Actuators A-Physical,* vol. 114, pp. 267-275, 2004.

[87] B. Stoeber and D. Liepmann, "Arrays of hollow out-of-plane microneedles for drug delivery," *Journal of Microelectromechanical Systems,* vol. 14, pp. 472-479, 2005.

[88] S. P. Davis, W. Martanto, M. G. Allen, and M. R. Prausnitz, "Hollow metal microneedles for insulin delivery to diabetic rats," *IEEE Transactions on Biomedical Engineering,* vol. 52, pp. 909-915, 2005.

[89] K. Kim, D. S. Park, H. M. Lu, W. Che, K. Kim, J.-B. Lee, and C. H. Ahn, "A tapered hollow metallic microneedle array using backside exposure of SU-8," *Journal of Micromechanics and Microengineering,* vol. 14, pp. 597-603, 2004.

[90] S. J. Moon and S. S. Lee, "A novel fabrication method of a microneedle array using inclined deep x-ray exposure," *Journal of Micromechanics and Microengineering,* vol. 15, pp. 903-911, 2005.

[91] C. Beuret, G.-A. Racine, J. Gobet, R. Luthier, and N. F. d. Rooij, "Microfabrication of 3D multidirectional inclined structures by UV lithography and electroplating," in *IEEE Workshop on Micro Electro Mechanical Systems*, Oiso, Japan, 1994, pp. 81-85.

[92] H. Sato, T. Kakinuma, J. S. Go, and S. Shoji, "In-channel 3-D micromesh structures using maskless multi-angle exposures and their microfilter application," *Sensors and Actuators A-Physical,* vol. 111, pp. 87-92, 2004.

[93] M. Han, W. Lee, S.-K. Lee, and S. S. Lee, "3D microfabrication with inclined/rotated UV lithography," *Sensors and Actuators A-Physical,* vol. 111, pp. 14-20, 2004.

[94] Y.-K. Yoon, J.-H. Park, F. Cros, and M. G. Allen, "Integrated vertical screen microfilter system using inclined SU-8 structures," in *16th IEEE International Conference on Micro Electro Mechanical Systems*, Kyoto, Japan, 2003, pp. 227-230.

[95] A. D. King and R. E. Walters, "Delivery of macromolecules into cells.", in *United States Patent* 6,603,998, 2003.

[96] S.-O. Choi, J.-H. Park, Y. Choi, Y. Kim, H. S. Gill, Y.-K. Yoon, M. R. Prausnitz, and M. G. Allen, "An electrically active microneedle array for electroporation of

skin for gene delivery," in *International Conference on Solid State Sensors and Actuators and Microsystems*, Seoul, Korea, 2005, pp. 1513-1516.

[97] N. Wilke, C. Hibert, J. O'Brien, and A. Morrissey, "Silicon microneedle electrode array with temperature monitoring for electroporation," *Sensors and Actuators, A-Physical,* vol. 123-124, pp. 319-325, 2005.

[98] J. W. Hooper, J. W. Golden, A. M. Ferro, and A. D. King, "Smallpox DNA vaccine delivered by novel skin electroporation device protects mice against intranasal poxvirus challenge," *Vaccine,* vol. 25, pp. 1814-1823, 2007.

[99] P. Yao, C. J. Schneider, and D. W. Prather, "Three-dimensional lithographical fabrication of microchannels," *Journal of Microelectromechanical Systems,* vol. 14, pp. 799-805, 2005.

[100] J. H. Moon, J. Ford, and S. Yang, "Fabricating three-dimensional polymeric photonic structures by multi-beam interference lithography," *Polymers for Advance Technologies,* vol. 17, pp. 83-93, 2006.

[101] K. Totsu, K. Fujishiro, S. Tanaka, and M. Esashi, "Fabrication of three-dimensional microstructure using maskless gray-scale lithography," *Sensors and Actuators A-Physical,* vol. 130, pp. 387-392, 2006.

[102] Y. Hirai, Y. Inamoto, K. Sugano, T. Tsuchiya, and O. Tabata, "Moving mask UV lithography for three-dimensional structuring," *Journal of Micromechanics and Microengineering,* vol. 17, pp. 199-206, 2007.

[103] D. Y. Oh, K. Gil, S. S. Chang, D. K. Jung, N. Y. Park, and S. S. Lee, "A tetrahedral three-facet micro mirror with the inclined deep X-ray process," *Sensors and Actuators a-Physical,* vol. 93, pp. 157-161, 2001.

[104] J. Schulz, A. Elkholi, J. Gottert, K. Kadel, and J. Mohr, "The influence of sloped absorber sidewalls in deep x-ray-lithography," *Microelectronic Engineering,* vol. 21, pp. 117-122, 1993.

[105] Y. K. Yoon, J. H. Park, and M. G. Allen, "Multidirectional UV lithography for complex 3-D MEMS structures," *Journal of Microelectromechanical Systems,* vol. 15, pp. 1121-1130, 2006.

[106] S. Arscott, F. Garet, P. Mounaix, L. Duvillaret, J. L. Coutaz, and D. Lippens, "Terahertz time-domain spectroscopy of films fabricated from SU-8," *Electronics Letters,* vol. 35, pp. 433-433, 1999.

[107] H. Lorenz, M. Despont, P. Vettiger, and P. Renaud, "Fabrication of photoplastic high-aspect ratio microparts and micromolds using SU-8 UV resist," *Microsystem Technologies*, vol.4, pp. 143-146, 1998.

[108] J. D. Williams and W. Wang, "Using megasonic development of SU-8 to yield ultra-high aspect ratio microstructures with UV lithography," *Microsystem Technologies,* vol. 10, pp. 694-698, 2004.

[109] J. H. Park, Y. K. Yoon, S. O. Choi, M. R. Prausnitz, and M. G. Allen, "Tapered conical polymer microneedles fabricated using an integrated lens technique for transdermal drug delivery," *IEEE Transactions on Biomedical Engineering,* vol. 54, pp. 903-913, 2007.

[110] R. T. Farouki and C. A. Neff, "Analytic properties of plane offset curves," *Computer Aided Geometric Design*, vol.7, pp. 83-99, 1990.

[111] G. Elber, I. K. Lee, and M. S. Kim, "Comparing offset curve approximation methods," *IEEE Computer Graphics and Applications,* vol. 17, pp. 62-71, 1997.

[112] G. Barequet, M. T. Dickerson, and M. T. Goodrich, "Voronoi diagrams for convex polygon-offset distance functions," *Discrete & Computational Geometry,* vol. 25, pp. 271-291, 2001.

[113] Y. Liming, L. Yong Yeow, F. E. H. Tay, and C. Iliescu, "Spray coating of photoresist for 3D microstructures with different geometries," *Journal of Physics: Conference Series*, vol. 34, pp. 937-942, 2006.

[114] P. Nga Phuong, E. Boellaard, J. N. Burghartz, and P. M. Sarro, "Photoresist coating methods for the integration of novel 3-D RF microstructures," *Journal of Microelectromechanical Systems,* vol. 13, pp. 491-499, 2004.

[115] A. Suriadi, F. Berauer, A. Yasunaga, A. Pan, and H. Vanderplas, "Uniform metal patterning on micromachined 3-D surfaces using multi-step exposure of UV light," in *Proceeding of SPIE*, vol. 4691, pp. 937-948, 2002.

[116] M. C. Gower, "Industrial applications of laser micromachining," *Optics Express,* vol. 7, pp. 56-67, 2000.

[117] N. H. Rizvi, P. T. Rumsby, and M. C. Gower, "New developments and applications in the production of 3D microstructures by laser micromachining," in *Proceeding of SPIE*, vol. 3898, pp. 240-249, 1999.

[118] A. S. Holmes, "Laser processes for MEMS manufacture," in *Proceeding of SPIE*, vol. 4426, pp. 203-209, 2002.

[119] C. G. K. Malek, "Laser processing for bio-microfluidics applications (part I)," *Analytical and Bioanalytical Chemistry,* vol. 385, pp. 1351-1361, 2006.

[120] C. G. K. Malek, "Laser processing for bio-microfluidics applications (part II)," *Analytical and Bioanalytical Chemistry,* vol. 385, pp. 1362-1369, 2006.

[121] W. A. Beck, M. Huang, J. Ketterl, and T. Hughes, "IR laser welding of thin polymer films as a fabrication method for polymer MEMS," in *Proceeding of SPIE*, vol. 5067, pp. 167-178, 2003.

[122] S. Rajaraman, O. C. Seong, R. H. Shafer, J. D. Ross, J. Vukasinovic, C. Yoonsu, S. P. DeWeerth, A. Glezer, and M. G. Allen, "Microfabrication technologies for a coupled three-dimensional microelectrode, microfluidic array," *Journal of Micromechanics and Microengineering,* vol. 17, pp. 163-171, 2007.

[123] C. Yoonsu, O. C. Seong, R. H. Shafer, and M. G. Allen, "Highly inclined electrodeposited metal lines using an excimer laser patterning technique," in *International Conference on Solid State Sensors and Actuators and Microsystems*, Seoul, Korea, 2005, pp. 1469-1472.

[124] Y.-L. Loo, R. L. Willett, K. W. Baldwin, and J. A. Rogers, "Additive, nanoscale patterning of metal films with a stamp and a surface chemistry mediated transfer process: applications in plastic electronics," *Applied Physics Letters,* vol. 81, pp. 562-564, 2002.

[125] S.-H. Hur, D.-Y. Khang, C. Kocabas, and J. A. Rogers, "Nanotransfer printing by use of noncovalent surface forces: Applications to thin-film transistors that use single-walled carbon nanotube networks and semiconducting polymers," *Applied Physics Letters,* vol. 85, pp. 5730-5732, 2004.

[126] Y. Choi, M. McClain, M. LaPlaca, A. Frazier, and M. Allen, "Three dimensional MEMS microfluidic perfusion system for thick brain slice cultures," *Biomedical Microdevices,* vol. 9, pp. 7-13, 2007.

[127] S. P. Davis, B. J. Landis, Z. H. Adams, M. G. Allen, and M. R. Prausnitz, "Insertion of microneedles into skin: measurement and prediction of insertion force and needle fracture force," *Journal of Biomechanics,* vol. 37, pp. 1155-1163, 2004.

[128] M. R. Prausnitz, B. S. Lau, C. D. Milano, S. Conner, R. Langer, and J. C. Weaver, "A Quantitative study of electroporation showing a plateau in net molecular-transport," *Biophysical Journal,* vol. 65, pp. 414-422, 1993.

[129] P. J. Canatella, J. F. Karr, J. A. Petros, and M. R. Prausnitz, "Quantitative study of electroporation-mediated molecular uptake and cell viability," *Biophysical Journal,* vol. 80, pp. 755-764, 2001.

[130] L. C. Heller, M. J. Jaroszeski, D. Coppola, A. N. McCray, J. Hickey, and R. Heller, "Optimization of cutaneous electrically mediated plasmid DNA delivery using novel electrode," *Gene Therapy,* vol. 14, pp. 275-280, 2007.

[131] G. S. Nanda and K. P. Mishra, "Studies on electroporation of thermally and chemically treated human erythrocytes," *Bioelectrochemistry and Bioenergetics,* vol. 34, pp. 129-134, 1994.

[132] R. Susil, D. Semrov, and D. Miklavcic, "Electric field-induced transmembrane potential depends on cell density and organization," *Electro- and Magnetobiology,* vol. 17, pp. 391-399, 1998.

[133] A. E. Sowers and M. R. Lieber, "Electropore diameters, lifetimes, numbers, and locations in individual erythrocyte-ghosts," *FEBS Letters,* vol. 205, pp. 179-184, 1986.